**UNIVERSITÀ DEGLI STUDI DI NAPOLI**
**"FEDERICO II"**

SCUOLA POLITECNICA E DELLE SCIENZE DI BASE
DIPARTIMENTO DI INGEGNERIA INDUSTRIALE

XXX CICLO

PHD DISSERTATION IN
INDUSTRIAL ENGINEERING

# Investigation of Chevron Synthetic Jets Flow Field and Heat Transfer

**Cuono Massimo Crispo**

| **Tutors** | **Coordinator** |
|---|---|
| Prof. Gennaro Cardone<br>Prof. Carlo Salvatore Greco | Prof. Michele Grassi |

December 2017

*"Instrue praeceptis animum, nec discere cesses;*
*Nam sine doctrina vita est quasi mortis imago."*
Dionysius Cato
(Disticha Catonis, Liber III)

# Contents

# List of Figures

# List of Tables

# Nomenclature

## Acronyms

| | |
|---|---|
| 2D | two-dimensional |
| 3D | three-dimensional |
| A/D | analog to digital |
| CJ | continuous jet |
| CCD | charge coupled device |
| CMOS | complementary metal-oxide-semiconductor |
| FOV | field of view |
| IFOV | instantaneous field of view |
| IR | infrared |
| K-H | Kelvin-Helmholtz |
| LWIR | long wavelength infrared |
| MRTD | minimum resolvable temperature difference |
| MTF | modulation transfer function |
| MDTD | minimum detectable temperature difference |
| MWIR | middle wavelength infrared |
| NASA | national aeronautics and space administration |
| NETD | noise equivalent temperature difference |
| OTF | optical transfer function |
| PIV | particle image velocimetry |
| SJ | synthetic jet |
| Stereo-PIV | stereoscopic particle image velocimetry |
| ZNMF | zero-net-mass-flux |

## Symbols

| | |
|---|---|
| $A_f$ | surface area of the foil, $\mathrm{m}^2$ |
| $B$ | calibration constant, K |
| $Bi$ | Biot number |
| $c$ | speed of propagation of an electromagnetic wave, $\mathrm{m\,s^{-1}}$ |
| $c_0$ | speed of propagation of light in vacuum, $\mathrm{m\,s^{-1}}$ |
| $C_1, C_2$ | first and second radiation constants, $\mathrm{W\,m^{-2}}$ and $\mathrm{K\,m}$ |
| $d_{diff}$ | diffraction image diameter of the particle, m |
| $d_{geom}$ | geometric image diameter of the particle, m |
| $d_p$ | diameter of the particle, m |
| $d_\tau$ | diameter of the particle image, m |
| $D$ | diameter of the nozzle exit section, m |
| $E$ | total hemispherical emissive power, $\mathrm{W\,m^{-2}}$ |
| $E_b$ | black body total hemispherical emissive power, $\mathrm{W\,m^{-2}}$ |
| $E_{b,amb}$ | black body total hemispherical emissive power of the ambient, $\mathrm{W\,m^{-2}}$ |
| $E_{b,atm}$ | black body total hemispherical emissive power of the atmosphere, $\mathrm{W\,m^{-2}}$ |
| $E_{b,obj}$ | black body total hemispherical emissive power of the body, $\mathrm{W\,m^{-2}}$ |
| $E_{b\lambda}$ | black body spectral hemispherical emissive power, $\mathrm{W\,m^{-3}}$ |
| $E_\lambda$ | spectral hemispherical emissive power, $\mathrm{W\,m^{-3}}$ |
| $E_t$ | total radiation collected by the IR camera detector, $\mathrm{W\,m^{-2}}$ |
| $f$ | oscillating frequency of the membrane, Hz |
| $f_{acq}$ | acquisition frequency, Hz |
| $f_\#$ | f-number or f-stop |
| $F$ | calibration constant |
| $\mathbf{F}$ | mapping function between object coordinates and image coordinates |
| $Fo$ | Fourier number |

| | |
|---|---|
| $h$ | convective heat transfer coefficient, $\mathrm{W\,m^{-2}\,K^{-1}}$ |
| $H$ | nozzle-to-plate distance, m |
| $I_1, I_2$ | normalised distribution of light intensity |
| $I_f$ | electric current imposed to the foil, A |
| $k$ | fluid thermal conductivity, $\mathrm{W\,m^{-1}\,K^{-1}}$ |
| $k_f$ | thermal conductivity of the foil, $\mathrm{W\,m^{-1}\,K^{-1}}$ |
| $L_0$ | stroke length, m |
| $L_0^{(f)}$ | synthetic jet formation stroke length, m |
| $m$ | natural number |
| $M$ | magnification factor |
| $n$ | index of refraction |
| $n_p$ | number of periods of membrane oscillation |
| $N$ | number of the instantaneous vector fields for a given phase angle |
| $N_{div}$ | number of sampled phases |
| $Nu$ | Nusselt number |
| $Nu_0$ | Nusselt number at the stagnation point |
| $Nu_{chev}$ | Nusselt number related to the chevron configuration |
| $Nu_{circ}$ | Nusselt number related to the circular configuration |
| $Nu_r$ | azimuthally averaged Nusselt number |
| $Q$ | second invariant of the velocity gradient, $\mathrm{s^{-2}}$ |
| $\dot{q}_c$ | convective heat flux, $\mathrm{W\,m^{-2}}$ |
| $\dot{q}_j$ | heat flux provided via Joule effect, $\mathrm{W\,m^{-2}}$ |
| $\dot{q}_{nc}$ | natural convection heat flux, $\mathrm{W\,m^{-2}}$ |
| $\dot{q}_r$ | radiative heat flux, $\mathrm{W\,m^{-2}}$ |
| $\dot{q}_{tc}$ | tangential conduction heat flux, $\mathrm{W\,m^{-2}}$ |
| $r$ | radial distance from the axis, m |
| $R$ | calibration constant, V or A |
| $R_c$ | normalised function of cross-correlation |
| $Re$ | Reynolds number |
| $s$ | foil thickness, m |
| $St$ | Strouhal number |
| $Stk$ | Stokes number |
| $t$ | time, s |
| $T$ | absolute body temperature, K |

| | |
|---|---|
| $T_{amb}$ | ambient temperature, K |
| $T_{atm}$ | atmosphere temperature, K |
| $T_{aw}$ | adiabatic wall temperature, K |
| $T_b$ | black body temperature, K |
| $T_{film}$ | film temperature, K |
| $T_{obj}$ | body temperature, K |
| $T_w$ | foil temperature, K |
| $TKE$ | time-averaged turbulent kinetic energy, $\mathrm{m^2\,s^{-2}}$ |
| $< TKE >$ | phase-averaged turbulent kinetic energy, $\mathrm{m^2\,s^{-2}}$ |
| $u, v, w$ | instantaneous $x$, $y$ and $z$ velocity components, $\mathrm{m\,s^{-1}}$ |
| $u_e$ | velocity along the jet centreline at the exit section, $\mathrm{m\,s^{-1}}$ |
| $< u >, < v >, < w >$ | phase-averaged $x$, $y$ and $z$ velocity components, $\mathrm{m\,s^{-1}}$ |
| $< u_r >, < u_\theta >$ | phase-averaged velocity components along the radial and azimuthal directions, $\mathrm{m\,s^{-1}}$ |
| $\overline{u_i' u_i'}$ | time-averaged Reynolds stresses, $\mathrm{m^2\,s^{-2}}$ |
| $< u_i' u_i' >$ | phase-averaged Reynolds stresses, $\mathrm{m^2\,s^{-2}}$ |
| $U, V, W$ | time-averaged $x$, $y$ and $z$ velocity components, $\mathrm{m\,s^{-1}}$ |
| $U_{amb}, U_{atm}, U_{obj}$ | output detected signals of the IR detector related to the ambient, atmosphere and body, V or A |
| $U_c$ | time-averaged axial velocity component along the jet centreline, $\mathrm{m\,s^{-1}}$ |
| $U_D$ | total output detected signal of the IR detector, V or A |
| $U_r, U_\theta$ | time-averaged velocity components along the radial and azimuthal directions, $\mathrm{m\,s^{-1}}$ |
| $U_0$ | characteristic velocity of the jet, $\mathrm{m\,s^{-1}}$ |
| $V_f$ | electric voltage imposed to the foil, V |
| $x-, y-, z-$ | spatial coordinates, m |
| $\underline{x}$ | image coordinates, px |
| $\underline{X}$ | object coordinates, m |
| $\nabla^2$ | two-dimensional Laplacian operator, $\mathrm{m^{-2}}$ |

## Greek symbols

| | |
|---|---|
| $\alpha$ | thermal diffusivity of the foil, $\mathrm{m^2\,s^{-1}}$ |
| $\alpha_r$ | absorptivity coefficient |
| $\alpha_{r\lambda}$ | spectral absorptivity coefficient |
| $\gamma$ | enhancement ratio |
| $\gamma_0$ | enhancement ratio at the stagnation point |
| $\delta z$ | depth of field, m |
| $\Delta_x, \Delta_y$ | local displacement components in the image plane, px |
| $\Delta x$ | distance between two subsequent planes, m |
| $\Delta t$ | time separation between the two laser pulses, s |
| $\varepsilon$ | emissivity coefficient of the paint |
| $\epsilon_\lambda$ | spectral hemispherical emissivity coefficient |
| $\epsilon_t$ | total hemispherical emissivity coefficient |
| $\lambda$ | wavelength of the electromagnetic wave, m |
| $\mu$ | fluid dynamic viscosity, Pl |
| $\nu$ | frequency of an electromagnetic wave, Hz |
| $\rho$ | fluid density, $\mathrm{kg\,m^{-3}}$ |
| $\rho_p$ | density of the particle, $\mathrm{kg\,m^{-3}}$ |
| $\rho_r$ | reflectivity coefficient |
| $\rho_{r\lambda}$ | spectral reflectivity coefficient |
| $\sigma$ | Stefan-Boltzmann constant, $\mathrm{W/(m^2K^4)}$ |
| $\uptau$ | actuation period, s |
| $\tau$ | relaxation time, s |
| $\tau_{flow}$ | characteristic time of the flow, s |
| $\tau_r$ | transmissivity coefficient |
| $\phi$ | phase angle, ° |
| $\omega_x, \omega_y, \omega_z$ | $x$, $y$ and $z$ vorticity components, $\mathrm{s^{-1}}$ |

# Summary

Over the last twenty years, synthetic jets have been a topic of extensive research. These jets have been studied in a wide range of engineering applications, especially for their flow control and heat transfer capabilities. Ongoing research and development efforts in promoting high heat and mass transfer rates have led to adopt impinging synthetic jets as a new solution. From this perspective, many studies have been aimed at evaluating the heat transfer though a complete characterisation of the flow topology of impinging synthetic jets is lacking. The flow associated with synthetic jets involves mechanisms of formation, evolution, interaction and breakdown of discrete vortical structures and small-scale turbulence. In particular, the coherent structures dynamics and the turbulence intensity affect the transport of scalar quantities of the jets. It is clear that it is needed to act on these flow features to affect the heat transfer. Several active and passive strategies have been employed to manipulate the natural behaviour of the flow such as exit geometry modification, insertion of grids and injection of secondary flows.

The present thesis analyses the effect of a saw-tooth exit pattern, called chevron exit, on the flow field and heat transfer of a synthetic jet. The chevron exits are generally applied at the trailing edge of jet engine nozzles for acoustic noise reduction and mixing enhancement. For the present study, the synthetic jet is obtained by a loudspeaker as oscillating element and a contoured nozzle as inlet/outlet aperture. Two experimental techniques are used: Stereoscopic Particle Image Velocimetry for the two-dimensional three-component flow field measurements and Infrared thermography in conjunction with the heated thin foil heat transfer sensor for the heat transfer measurements.

Owing to the peculiar features of synthetic jets and the effect of the chevron elements on the coherent structures organisation, the chevron exit could lead to a heat transfer enhancement. It is shown that this kind of nozzle can produce an increase of turbulence intensity levels in some regions of the field and entrainment and mixing enhancement by introducing streamwise coherent structures.

In Chapter 1, the literature about free and impinging synthetic jets is reviewed in attempt to explain how the flow field influences the heat transfer distribution on the wall and to describe the state of the art in the field of synthetic impinging jets. A glance at the effects of the chevrons on continuous and pulsed jets is given. This literature survey motivates the study of chevron synthetic jets in free and impinging conditions to understand the fluid mechanics characteristics and the heat transfer performance.

In Chapters 2 and 3, the working principles and the state of art of the employed measurement techniques are described.

The results obtained are organised in the following three chapters. Since a synthetic jet with a chevron exit is investigated for the first time, the flow topology in free condition (i.e. without impingement plate) is presented in Chapter 4. The time- and phase-averaged flow fields are investigated. In order to highlight the effect of the chevron nozzle onto the flow field, a comparison with a round jet without vortex generators is carried out. A three-dimensional reconstruction of the large scale coherent structures elucidates the organisation of the flow field.

The effects of the chevron geometry on the convective heat transfer rates, assessed with the Infrared thermography measurements, are explored in Chapter 5. A comparison with a circular synthetic jet is carried out.

Finally, a particular condition of heat transfer is chosen and the corresponding flow field is investigated in Chapter 6. The fluid-dynamic mechanisms behind the convective heat transfer rate that characterises both the chevron and circular impinging synthetic jets are investigated. The organisation of the coherent structures impinging on the plate is reconstructed.

# Chapter 1

# Introduction and background

In this chapter, a review of the main features of free and impinging synthetic jets will be carried out, with a particular focus on the round jet topology. Furthermore, the performances in terms of convective heat transfer of such jets when impinging onto a flat surface will be discussed. Then, innovative solutions of synthetic jet devices for heat transfer enhancement are illustrated with particular focus on the exit geometry modification. Moreover, in Section 1.3, a brief history of the chevron elements is presented with reference to the applications and the effect on the flow field. The main objectives and the outline of the thesis are illustrated in the last two sections.

## 1.1 Synthetic jets

### 1.1.1 Free synthetic jets

The transmission of acoustic waves produced by the oscillating boundary of a quiescent medium can generate a streaming motion without mass addition. The first to understand this was Lord Rayleigh at the end of 19th century. He wrote in his work (Rayleigh, 1896, vol.2 pp.236–237): "*The precise conditions under which jets are formed is a subject of great delicacy... But with air, as we actually have it, moving under the action of the pressures to be found in resonators, it must be admitted that jets may sometimes occur. While experimenting about two years ago with one of Konig's brass* *resonators of pitch c', I noticed that when the corresponding fork, strongly excited, was held to the mouth of the Helmholtz resonator a wind of considerable force issued from the nipple at the opposite side. This effect may rise to such intensity as to blow out a candle upon whose wick the stream is directed... Closer examination revealed the fact that at the sides of the nipple the outward flowing stream was replaced by one in the opposite direction, so that a tongue of flame from a suitable placed candle appeared to enter the nipple at the same time that another candle situated immediately in front was blown away*". This is the first scientific work that reports on the observation of acoustic streaming. Later in 1948, the general equations of the second-order acoustic phenomena were developed by Eckart (1948). A higher degree of approximation of the theory of sound of Lord Rayleigh was presented. Based on this theory of streaming caused by sound waves developed by Eckart (1948), Ingård and Labate (1950) carried out an investigation of circulations in air caused by sound waves at audio frequencies in the neighbourhood of an orifice. For the first time, the flow field of a synthetic jet was investigated. Mednikov and Novitskii (1975) induced an oscillatory velocity field with a mechanical piston at a frequency range between 10 Hz and 100 Hz. They reported the formation of a jet without net mass flux and average velocity up to $17\,\mathrm{m\,s^{-1}}$. Subsequently, Lebedeva (1980) performed an interferometer study of the velocity field near an orifice with a diameter of 0.75 cm for frequencies of normal sound waves of 500 Hz and 1600 Hz, generating a jet with velocities up to $10\,\mathrm{m\,s^{-1}}$. Lighthill (1978) stated that the streaming motions induced by acoustic waves result from the acoustic energy dissipation through two mechanisms: the transmission attenuation of pressure waves through a compressible medium (within the fluid) while the second is related to viscous effects at a vibrating boundary of a solid body adjacent to fluid at rest. These streaming motions without mass addiction which are generated by the transmission of acoustic waves or by the oscillating solid boundary in a quiescent fluid typically do not present discrete vortices that are involved in the formation of synthetic jets.

The first scientists to propose an innovative device called zero-net-mass-flux synthetic jet were Coe et al. (1994, 1995). As sketched in Figure 1.1, a synthetic jet (SJ) or zero-net-mass-flux (ZNMF) device, consists of a cavity bounded on a side by an oscillating boundary (in common applications it consists of a loudspeaker, piezoelectric diaphragm or piston) and on the opposite side by an opening (orifice, slot, pipe or nozzle) acting as both inlet and outlet. The oscillation of the moving boundary causes periodic cavity volume changes and, as a result, pressure variations which lead to the alternate ejection and suction of fluid across the opening. In this way, the device is able to transfer momentum to the external environment without net mass ejection. During the ejection stroke, the flow separates at the edges of the outlet and a vortex sheet rolls up, and under certain conditions (Holman et al., 2005), a vortex ring is formed and convects away under its own self-induced velocity. During the suction stroke, the fluid is entrained into the cavity from all directions. The jet formation is possible if the ejected fluid has enough momentum to win the call back forces, otherwise the vortex ring is ingested back into the orifice and no jet is formed. The time-periodic cycle induces a time-periodic formation, advection and interactions of discrete vortical structures which ultimately become turbulent, slow down, and lose

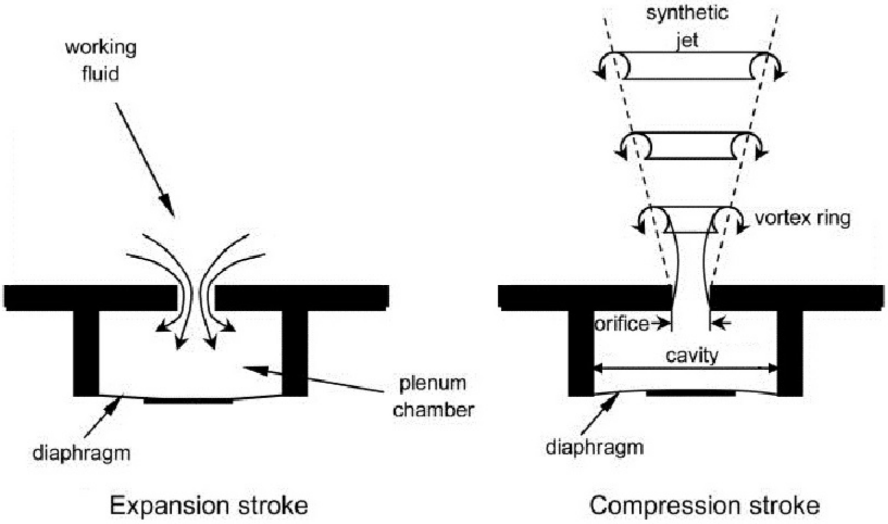

Figure 1.1: Sketch of a synthetic jet device. On the left: fluid ingestion phase; on the right: fluid expulsion phase and vortex ring formation, (adapted from Al-Atabi, 2011).

their coherence turning into a steady turbulent jet (Smith and Glezer, 1998) and the formation of a stagnation point, located on the centreline, also named saddle point, which separates the suction flow directed towards the cavity from the established jet convecting away.

The flow behaviour of a synthetic jet can be characterised by two dimensionless parameters, the Reynolds and Strouhal numbers, defined as

$$Re = \frac{\rho U_0 D}{\mu} \tag{1.1}$$

$$St = \frac{D}{L_0} = \frac{fD}{U_0} \tag{1.2}$$

where $\rho$ is the fluid density, $U_0$ is the characteristic velocity of the jet, $D$ is the characteristic length usually the orifice or nozzle diameter, $\mu$ is the fluid dynamic viscosity, $L_0$ is the stroke length (defined as $U_0/f$) and $f$ is the oscillating frequency of the membrane. In literature, it is possible to find several definitions of the reference velocity $U_0$ (Smith and Glezer, 1998; Cater and Soria, 2002; Mallinson et al., 1999). In the present work, accordingly to Smith and Glezer (1998), $U_0$ is defined as the mean centreline velocity over the ejection half of the cycle

$$U_0 = \frac{1}{\tau} \int_0^{\frac{\tau}{2}} u_e(t) dt \tag{1.3}$$

where $\tau$ is the actuation period and $u_e$ is the velocity along the jet centreline at the exit section.

SJ actuators have been arousing a great deal of interest because of their advantages. A major characteristic of these devices is, as the name suggests, that they produce a zero-net-mass flux, whilst a non-zero momentum rate is produced. Furthermore, the jet generation does not require any continuous fluid supply, because it is synthesised directly from the surrounding fluid in which they are deployed. This allows small size and low cost solutions. They are more efficient devices requiring lower power consumption than fans. In addition, control and design of SJ actuators are rather simple and their actuation frequency can range from few to several kHz. The main disadvantages are related to a maximum velocity achievable, mechanical failure due to fatigue mechanism and noise problems (Lasance and Aarts, 2008).

During last years, the flow field of unconfined SJs has been investigated both experimentally and numerically (e.g. Rumsey et al., 2006; Mohseni and Mittal, 2014) and comparisons with continuous jets (CJs) have been carried out. Smith and Glezer (1998) first presented a comprehensive experimental study of SJs. A planar SJ, obtained with a rectangular two-dimensional (2D) slot exit was compared with a conventional 2D CJ. The results showed that a jet is formed by the movement of a piezoelectric-driven diaphragm in a cavity and the jet becomes turbulent in the far field. In the far field, the SJ is similar to conventional 2D jets in that cross-stream distributions of the time-averaged velocity and the corresponding rms fluctuations. However, compared to CJs, the mean centreline velocity of the SJ decreases faster and the streamwise increase of its width and volume flow rate is lower. Differently, Cater and Soria (2002) experimentally investigated a round SJ generated by an oscillating piston in a cavity behind a circular orifice. They observed that in the far field the round turbulent SJ has a self-similar cross-stream velocity distribution analogous to that of a conventional CJ but with a larger spreading rate and entrainment.

The intense research associated with these actuators has produced a large amount of works and the scientific knowledge has remained scattered across several journal articles and conference papers. The first effort to arrange the literature about this topic was done by Glezer and Amitay (2002). Glezer and Amitay described, in the first part of their work, the SJ formation and evolution in the near and far field. The interaction of SJs with a cross flow was treated in the second part. They stated that "*It is clear that at least in the near field of the jet, its evolution depends critically on the details of the formation and advection of the discrete vortices in the presence of the time-periodic reversed flow*" (Glezer and Amitay, 2002). In the far field, although streamwise and crosswise velocity profiles and the corresponding rms velocity fluctuations present self-similar profiles, other variables such as the mean centreline velocity, the jet width and the volume flow rate do not match corresponding scaling for CJs. The discrepancies were associated with a streamwise decrease in the momentum flux of the jet as a result of the adverse streamwise pressure gradient near the jet orifice imposed by the suction phase. Subsequently, measurements of rectangular 2D slot SJs with *Re* equal to 2000 and comparisons with CJs at the same Reynolds number were conducted by Smith and Swift (2003). Their experiments showed that in the far field, SJs present the same self-similar velocity profiles of CJs as found by Cater and Soria (2002) and Glezer and Amitay (2002). In the near field, SJs are dominated by vortex pairs that entrain more fluid than CJ columns. Therefore, synthetic jets grow more rapidly, both in terms of jet width and volume flux, than CJs do. Likely, these latter findings are different from those obtained by Smith and Glezer (1998) because of the different operating conditions.

The effect of the dimensionless stroke length and Reynold number were investigated by Shuster and Smith (2007). In agreement with the previous works, in the near field, they found that the flow is dominated by the vortex ring formed during the expulsion phase of the actuator cycle, and the flow field scales exclusively with the actuator stroke length. For distances from the orifice greater than the stroke length $L_0$, the flow field first undergoes a transition from discrete vortex rings to a nominally steady turbulent jet and then resembles a conventional round turbulent jet. However some differences were observed in the far field. The SJ had a faster spreading rate with a correspondingly more rapid decrease in the mean centreline velocity. They stated that the dimensionless stroke length, $L_0/D$, uniquely identifies a synthetic jet flow. More recently, McGuinn et al. (2013) have carried out high-speed particle image velocimetry (PIV) and hot-wire anemometry measurements to investigate the effect of varying stroke length on the flow morphology of SJs. Four free synthetic jet flow morphology regimes were identified, based on threshold values for the stroke length $L_0/D$, which are in good agreement with previously published findings for an impulsively started jet flow. No jet is formed for dimensionless stroke length below the formation threshold $L_0/D \leq 2$. In agreement with Gharib et al. (1998), the strength of a vortex ring increases as the stroke length increases up to $L_0/D = 4$. For additional ejected fluid, $4 \leq L_0/D \leq 8$, the vortex ring shows a wider vortex core and a following trailing jet is formed. For $8 \leq L_0/D \leq 16$, in the trailing jet a maximum ejected velocity was observed, which destabilises the vortex and results in an increased flow mixing. Higher $L_0/D$ exhibited a flow regime dominated by the trailing jet, which overtakes the vortex, resulting in a highly turbulent intermittent jet flow. Figure 1.2 shows a schematic illustration of the morphology of formation and evolution of the synthetic jet flow at different stroke lengths.

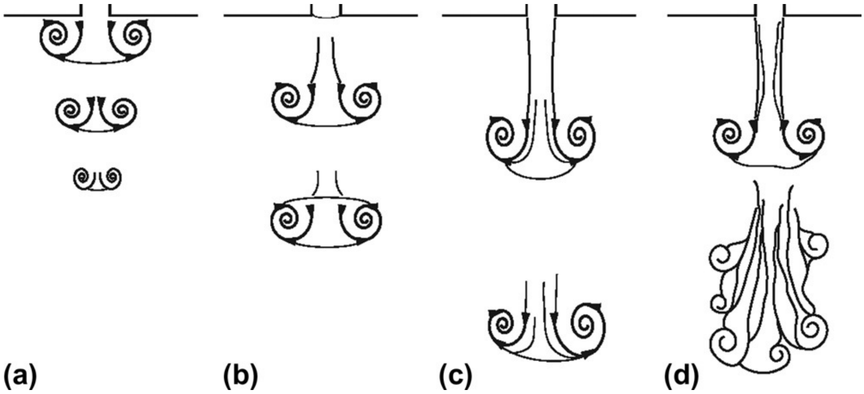

Figure 1.2: Flow morphology of vortex evolution at various stroke lengths (a) $L_0/D < 4$, (b) $4 \leq L_0/D < 8$, (c) $8 \leq L_0/D < 16$, and (d) $L_0/D \geq 16$, (McGuinn et al., 2013).

These works represent only a part of the main contributions in literature, which have given more insight about SJs, increasing the knowledge about their flow field and highlighting the differences with conventional CJs.

### 1.1.2 Impinging synthetic jets: flow field and heat transfer features

Studies on a single isolated SJ have pointed out the great potential of these devices from the standpoint of both fluid dynamic and technical/practical assessments. SJs have risen increasing interest in many fields of application such as flow control (Amitay et al., 2001), micropropulsion (Mueller et al., 2000), active control for micro air vehicles (Otani et al., 2009), jet vectoring (Smith and Glezer, 2002), mixing enhancement (Wang and Menon, 2001) and heat transfer (Pavlova and Amitay, 2006). In particular, due to the unsteady nature of the phenomenon and the larger jet width and entrainment than CJs, synthetic jets have attracted considerable interest in heat transfer applications.

There is a large number of studies describing and evaluating the heat transfer capabilities of SJs. In 1982, Gutmark et al. (1982) first presented heat transfer data on SJs used to enhance both natural and forced convection. The results showed that the acoustically excited flow increases the overall heat transfer coefficient. Several years later, the design and thermal performance of a heat sink for high power dissipation was studied in combination with SJ impingement by Mahalingam and Glezer (2005). The results revealed a case temperature decrease from 71.5 °C to 36 °C with SJs operation and a power dissipation of 20–40 % higher than the same heat sink with a fan in the flow rate range of 3–5 cubic feet per minute. The effects of jet formation frequency and Reynolds number at different nozzle-to-surface distances were investigated by Pavlova and Amitay (2006). Using particle image velocimetry, Pavlova and Amitay showed that at higher frequencies, the jet was associated with merging and breakdown of vortices before impinging on the surface. At lower frequencies, the wavelength between coherent structures is larger such that vortex rings impinge on the surface individually. For this reason, the axial turbulent velocity shows only a peak near the impingement plate at low frequency and the heat removal is associated with large-scale mixing, whilst, at high frequency, it attains high values along the shear layers of the vortex ring as results of a small-scale mixing. Later, Valiorgue et al. (2009) also performed PIV measurements to clarify the influence of the impinging vortex on the time-averaged heat transfer distribution. The impinging flow field was studied for fixed dimensionless orifice-to-plate distance equal to 2 and dimensionless stroke length and Reynolds number ranging between $1 < L_0/D < 22$ and $1000 < Re < 4300$, respectively. For high stroke lengths ($L_0/D > 5$), an increasingly stronger time-averaged recirculation vortex was observed close to the heat transfer surface, around a radial distance from the axis of $r/D \cong 2$. This vortex was not observed for lower stroke lengths. In agreement with Shuster and Smith (2007), they also observed that the flow structure for a fixed stroke length was unaffected by the Reynolds number . More recently, in a work of Chaudhari et al. (2010a), the heat transfer performance of an impinging synthetic jet at Reynolds number ranging between 1500–4200 and for nozzle-to-plate distances varying between 0–25 exit diameters was investigated. They carried out a comparison with a continuous jet observing comparable performance between the two jets at Reynolds number equal to 4000 and envisaging a better performance of the SJs at higher Reynolds numbers.

As for CJs, heat transfer correlations have been developed also for SJs (Persoons et al., 2011; Arik and Icoz, 2012). Persoons et al. (2011) compared the stagnation point heat transfer performance of an axisymmetric SJ versus established CJ correlations. Persoons et al. proposed a general correlation for the stagnation point Nusselt number including the effect of all appropriate scaling parameters: Reynolds number ($500 \leq Re \leq 1500$), normalised exit-to-plate distance ($2 \leq H/D \leq 16$) and dimensionless stroke length ($2 \leq L_0/D \leq 40$). Based on such a correlation, Persoons et al. defined four heat transfer regimes, each one identified by a different range of values acquired by the ratio $(L_0 - L_0^{(f)})/H$ (where $L_0^{(f)}$ is the SJ formation stroke length, i.e., practically the escape length of the vortex ring in order to not be swallowed again in the orifice during the suction phase). Arik and Icoz (2012) established a closed form empirical correlation to predict the heat transfer coefficient as a function of Reynolds number, axial distance, orifice size and jet driving frequency. They observed that the heat transfer coefficient on a vertical surface increases with the driving voltage; it has a peak at the resonance frequency and the effect of the axial distance on the heat transfer becomes stronger as the jet driving frequency increases. The empirical correlation proposed by Arik and Icoz is valid for $Re < 2900$, $5 < H/D < 20$ and actuation frequency between 0.16 times the resonance frequency and the resonance frequency itself. This correlation law does not take into account the Strouhal number influence on the SJ flow field topology that affects the convective heat transfer mechanisms. McGuinn et al. (2013) studied the impinging flow field of SJs with high-speed PIV and hot wire anemometry. They also accounted for the presence of the plate with the non-dimensional parameter $(L_0 - L_0^{(f)})/H$, as previously done by Persoons et al. (2011). In the study by McGuinn et al., $L_0^{(f)}$ was constant and equal to 2 diameters, the dimensionless nozzle-to-plate distance varied between 2 and 16, the dimensionless stroke length between 3 and 32 and the Reynolds number was equal to 1500. A first regime was found for $(L_0 - L_0^{(f)})/H \leq 0.5$, which corresponds to a stroke length slightly higher than the formation one; as a consequence the momentum of the jet reaching the surface is very weak. Accordingly, the heat transfer increases with increasing $(L_0 - L_0^{(f)})/H$ up to

1. Further increase of this ratio is seen to promote radial spreading of the jet causing reduction in time-average velocity approaching the impingement region for $1 < (L_0 - L_0^{(f)})/H \leq 2$, while for $(L_0 - L_0^{(f)})/H > 2$ the flow field was dominated by the trailing jet. Ultimately, the flow regimes identified by McGuinn et al. are in good agreement with the stagnation point heat transfer regimes presented by Persoons et al. with no flow field information.

Numerical studies have been undertaken in order to correlate the heat transfer and the impinging flow field of SJs. Silva and Ortega (2013) numerically studied the relationship between the flow field and the heat transfer of a purely oscillatory jet (that is not influenced by the exit geometry). They solved the problem by using a fully unsteady, two dimensional finite volume approach to determine the complex time dependent flow field varying several parameters: driving frequency (400–1200 Hz), Reynolds number (203–508) and orifice-to-plate distance (5–20$D$). They found that the merging of vortices led to a lower heat transfer and that, by using the point-to-point correlations, the instantaneous local Nusselt number was strongly correlated to the axial impinging velocity. Bazdidi-Tehrani et al. (2011) numerically analysed the nozzle-to-plate distance (ranging between 2–8$D$) and frequency (equal to 16, 80 and 400 Hz) influence on the heat transfer and flow field of a confined impinging synthetic jet at Reynolds number equal to 3386 with a turbulence intensity set to 10 %. They found that a recirculation zone, between the confined synthetic jet device and the impingement plate, is generated at dimensionless nozzle-to-plate distances equal to 2 and 4 which causes a decrease in the heat transfer performance. Such a region disappears for higher nozzle-to-plate distances leading to an increase of the heat transfer. This recirculation region reduces the effective heat transfer because it stops the counter current flow which helps to remove the heated air supplying fresh incoming air. They also noticed that the heat transfer rate is enhanced as the frequency increases, because such unfavourable recirculation region decreases and that SJ provides a heat transfer rate greater than a steady jet whose velocity is the same of the maximum expulsion velocity of the synthetic jet (during its ejection phase). Moreover, they stated that the vortex motion influences the heat transfer: an increase in the local heat transfer is obtained while the vortex ring is sweeping the impinging wall. Such an enhancement decreases as the vortex ring moves farther from the stagnation point.

A large amount of works deals with the heat transfer features of SJs. Nevertheless, little is known about the flow field of an impinging SJ compared to their free flow field counterpart. In fact, the literature on the characterisation of the impinging flow field of such jets is rather limited and incomplete. This is mostly due to the increase of the parametric space with not only includes a dependence on $H/D$ but also on $L_0/D$. The main reason for this is that the investigations on impinging synthetic jets are mainly interested in heat transfer behaviour and partially analyse the flow field. Some authors, as Bazdidi-Tehrani et al. (2011); Persoons et al. (2011), have highlighted the necessity of further experimental and numerical investigations on the impinging SJ flow field.

Recently, Greco et al. (2017) have conducted an experimental study on the impinging field of SJs. They analysed the influence of the Strouhal number (0.011, 0.022 and 0.044) and the orifice-to-plate distance (2, 4 and 6 orifice diameters) at a Reynolds number equal to 35000. This study shows that the Strouhal number mainly affects the SJ structure because it governs the influence of the vortex ring and the trailing jet on the flow field. A higher Strouhal number produces a flow field characterised by the stronger effect of vortex ring, which leads to higher entrainment and as a consequence a larger jet width and lower centreline velocity. Higher Strouhal numbers also produce smaller stroke length, which involves reduced trailing jet, lower extension of the potential core and higher centreline turbulent kinetic energy. A reduced stroke length also involves a small saddle point excursion along the centreline. Conversely, for lower Strouhal numbers, the leading role is assumed by the trailing jet. The flow topology of impinging SJ is strongly affected by the adverse pressure gradient induced by the presence of the impingement plate. The exit-to-plate distance modulates the adverse pressure gradient strength which affects the streamwise evolution of the shear layer and the vortex ring behaviour. Small orifice-to-plate distances cause a high adverse pressure gradient and the SJ impinges the plate with the potential core region leading a double peak axial velocity distribution on the plate and a peak in the radial velocity component. At larger distances, the adverse pressure gradient is weaker and the impinging axial velocity profile is Gaussian-shaped preventing the occurrence of the radial velocity peak.

Some studies, under certain conditions, have found similar aspects between synthetic and continuous jets. For this reason, it is worthwhile to report a brief review on the behaviour of impinging continuous jets. Numerous reviews were dedicated to the topic over the last years, trying to point out both the flow field topology and the heat and mass transfer properties of impinging jets (Martin, 1977; Polat et al., 1989; Jambunathan et al., 1992; Viskanta, 1993; Carlomagno and Ianiro, 2014). The impinging CJ flow field can be subdivided into different regions, as schematically represented in Figure 1.3.

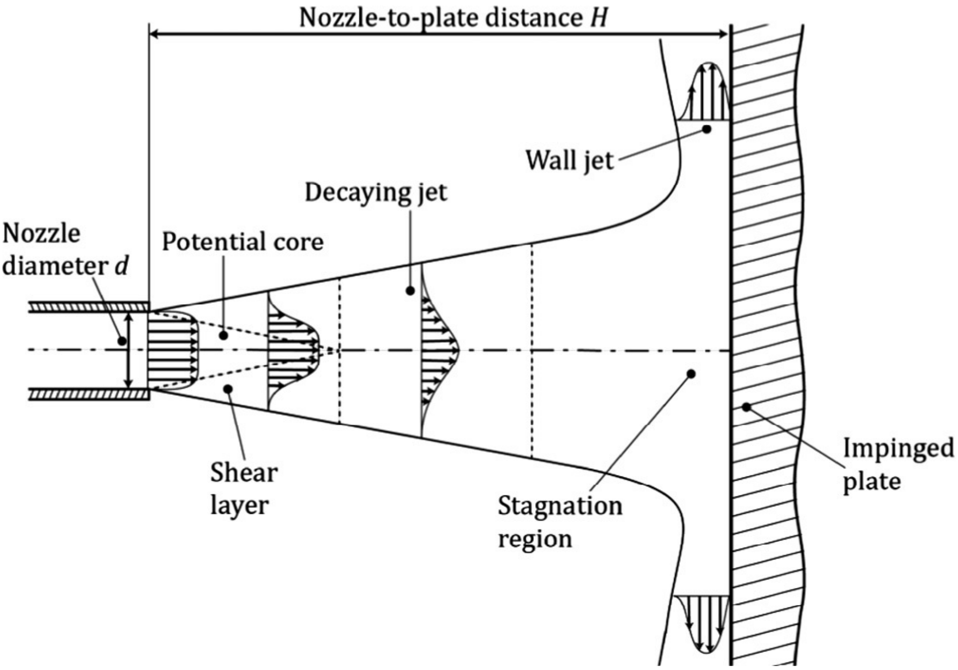

Figure 1.3: Schematic representation of the flow regions of a round impinging continuous jet, (Carlomagno and Ianiro, 2014).

When the jet is sufficiently far from the impingement surface it behaves as a free submerged jet. It is possible to distinguish a region referred to as free jet region. The interaction of the emerging jet with the quiescent ambient fluid triggers a shear-driven entrainment of mass, momentum and energy towards the jet core. As sketched, a region of the jet is not affected by the shear layer and it is referred to as potential core, where the original flow velocity and total pressure are retained. The potential core diminishes in width as the shear layer grows and as a rule of thumb the end of the core region is defined as the axial position from the nozzle exit where the average centreline flow dynamic pressure reaches 95 % of its initial value. Generally, the potential core zone extends from the orifice exit 6–7 nozzle diameters for axisymmetric jets and 4.7–7.7 orifice widths for slot jets. Beyond the potential core, the jet is followed by a flow developing region, and afterwards by a fully developed region. Both these two regions (extending for few diameters) are referred as decaying jet region because the axial velocity profile "decays" from a top-hat-shaped to a Gaussian-shaped profile. When the exit-to-plate distance is such that the potential core and the decaying jet regions exist, they constitute the free jet region, where the impingement wall is practically not yet affecting the flow field. While the jet is approaching the plate, the axial velocity is decreasing and is undergoing a rapid change of direction (in the plate-parallel direction) in the so-called quasi stagnation region. The consequence is an increment in the static pressure that is propagated upstream. From the stagnation point, the flow evolves along the impingement plate spreading radially into the so-called wall jet region. The flow velocity approaches a zero value at the stagnation point and then is accelerated up to a maximum value that occurs at a radial distance of about one nozzle diameter from the stagnation point. The wall boundary layer grows, entrains more fluid and the location of maximum of the velocity profile shifts progressively farther from the wall, while the average peak speed decreases. After, in the fully developed wall jet region, the flow becomes self-similar, with the maximum in the radial velocity that tends to zero as the distance from the stagnation region increases. Whereas the stabilizing effect of the acceleration keeps the boundary layer laminar in the stagnation zone, transition to turbulence generally occurs in the decelerating flow region immediately after the coordinate at which the flow reaches the maximum velocity.

It is obvious that the described impinging field changes at short nozzle-to-plate distances and some regions may be no longer present. As the plate gets closer to the jet exit, first the fully developed region disappears, then the whole decaying jet region may disappear. If the target plate distance is further reduced, within a distance of about two nozzle diameters, the high static pressure in the stagnation region has a significant influence on the flow development up to the nozzle. Thus, impingement occurs within the jet potential core.

The heat transfer characteristics are sensitive to the impinging flow conditions and vortical structures. An impinging jet is often considered to be laminar up to a jet Reynolds number, based on the nozzle diameter and exit conditions, of approximately 2500. However, there are many factors that could generate a turbulent jet, such as the dimensionless nozzle-to-plate distance, if the jet is confined or not, the original velocity profile and upstream conditions. In the initial jet region, the primary source of turbulence is the shear flow at the jet edges. This shear layer naturally grows along the jet axis. The shear layer generates flow instability, similar to the Kelvin–Helmholtz one. So, also in the case of impinging continuous jets, large scale structures (in form of K-H instabilities) are present before impinging onto the plate. The largest eddies have a length scale of the same order of magnitude as the nozzle diameter. They may either independently break up into smaller eddies at impingement or meet and interact with other downstream flow features, if the impingement plate is sufficiently far away. On the other side, in the decaying jet the flow may form small eddies within the centre of the jet, eventually developing into an unstructured turbulent flow field with little or no coherent structures in the entire jet core. Approaching the impingement plate, additional mechanisms take part to influence the flow. The pressure gradients within the flow field cause the flow to deflect, altering the shear layer and turning as well as stretching large-scale structures.

Large scale coherent structures develop in the jet shear layer. They undergo an acceleration due to the conversion of the momentum transferred from the axial to the radial component. The vortices may penetrate into the boundary layer and exchange fluid of differing kinetic energy and temperature (or concentration). In the vicinity of the impingement plate, the vortex rings interact with the boundary layer all the way around. As these vortices, also named primary vortices, travel against and along the wall, they produce secondary counter-rotating vortices responsible of the separation of the boundary layer at about 1.5-2 diameters from the nozzle axis. These structures are reported in Figure 1.4.

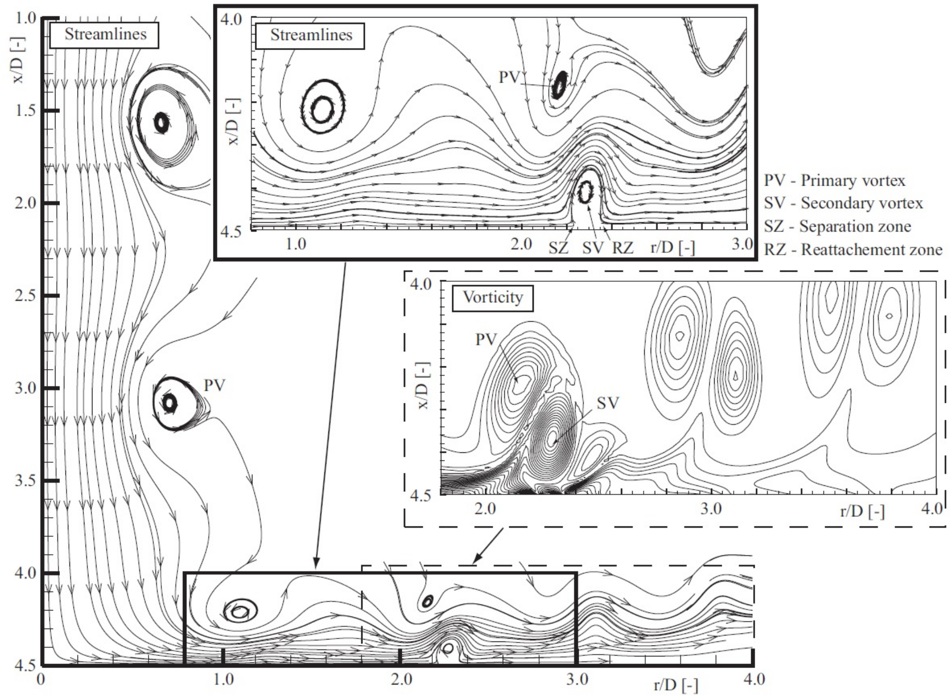

Figure 1.4: Instantaneous flow field of a laminar round impinging jet, (Rohlfs et al., 2012).

The convective heat transfer properties of round impinging jets have been detailed in numerous investigations (Martin, 1977; Polat et al., 1989; Jambunathan et al., 1992; Viskanta, 1993; Carlomagno and Ianiro, 2014). As already mentioned, they result extremely well performing when a high convective heat transfer rate is required. The convective heat transfer is generally presented in terms of the Nusselt number $Nu = hD/k$, being $h$ the convective heat transfer coefficient, $D$ a reference length and $k$ the fluid thermal conductivity. In general, the dimensional convective heat transfer $h$ is also reported in literature as shown in Figure 1.5.

At the stagnation point, at relatively short nozzle-to-plate distances, the heat transfer values increase as $H/D$ increases. In particular, this is associ-

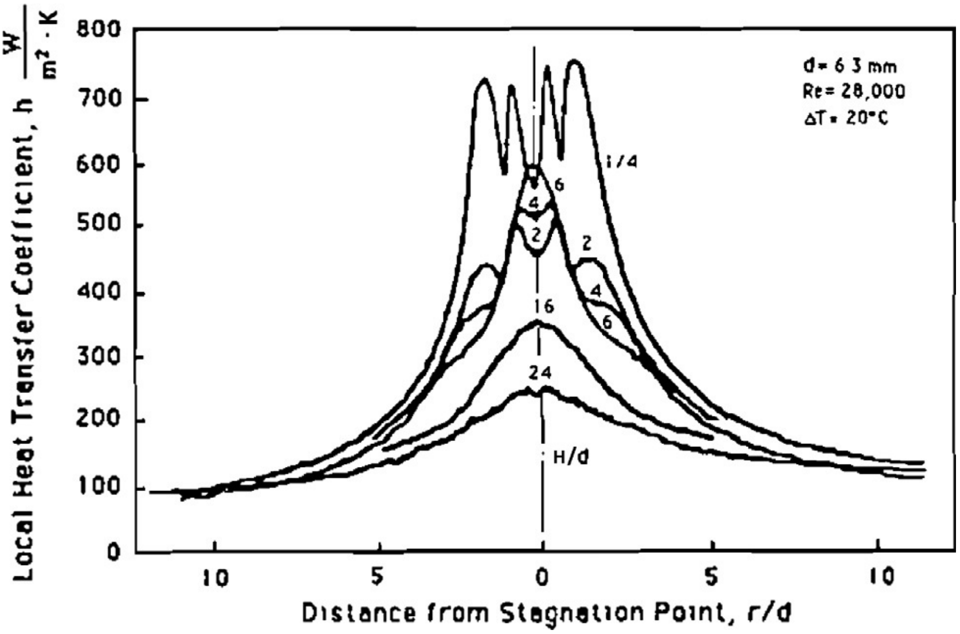

Figure 1.5: Heat transfer coefficient radial profiles for various dimensionless nozzle-to-plate distances, (Gardon, 1962).

ated to two aspects: the fact that the axial velocity is nearly constant within the potential core, whose extension ranges from 4.5 to 6 diameters; and on the other side, the progressive penetration of the shear layer towards the jet axis produces an increment of the convective heat transfer rate. The region immediately beyond the potential core presents high turbulence intensity levels, thus the stagnation Nusselt number at the nozzle-to-plate distance of about $6D$ attains a maximum. Beyond this limiting distance, representative of the extension of the potential core itself, the stagnation Nusselt number monotonically decreases because the turbulence intensity level does not compensate for the velocity deficit.

As the distance from the nozzle exit increases, for short nozzle-to-plate separations the radial heat transfer profile presents a double peak radial distribution (see Figure 1.5). An inner peak, located at about $0.5D$ from the axis, is addressed to the concurrent effect of the impinging jet shear layer and to the high values of the impinging jet axial velocity, which then convects a large amount of fluid in this region, causing an increment of the heat transfer rate. As also shown by the flow field results, the fluid converts its axial velocity into a radial component, accelerates but then experiences a local separation due to the effect of the secondary vortex, as reported in Figure 1.4. This has two consequences: first, the local separation produces a minimum in the heat transfer rate; second, downstream of the separation, the reattaching fluid produces a further enhancement of the heat transfer values.

Depending on the nozzle geometry and on the upstream turbulence level, the second maximum is generally located at radial separations from the nozzle axis ranging from 1.5 to 2 diameters. For nozzle-to-plate distances larger than $6D$, the heat transfer radial profile is monotonically decreasing because: from one side the axial impinging velocity decreases; while from the other side, the primary vortex ring at the impinging plate is not strong enough to cause the wall boundary layer separation. In the wall jet region, the Nusselt number monotonically decreases.

## 1.2 Synthetic jet devices: innovative solutions

As seen before, several investigations have focused on exploring the effects of varying some design and/or operation parameters (e.g. cavity geometry, exit configuration, Reynolds number, Strouhal number, nozzle-to-plate distance) on different fields of applications such as: heat transfer, jet vectoring, noise suppression and mixing enhancement.

Some innovative configurations were based on the generation of multi-cavity SJs by using a unique device. A new generation of SJ devices was provided by Luo et al. (2006). It consists of a cavity split in two sub-cavities bounded by the same oscillating piezoelectric diaphragm and with two exit slots. Thus, two adjacent jets can be established downstream, and a slide block regulates the two jets. The numerical computations showed that this new device may double the function of the existing devices and also resolve the problems of pressure loading and energy inefficiency of the existing devices. The slide block of the new SJ device has an important regulating function and different types of SJs can be generated with slight modifications of the slide block. Subsequently, this device was realised and PIV measurements were reported in a work of Luo et al. (2011). It was shown that in the near field, the two jets entrain fluid around them and interact with each other generating a complex phenomenon of "self-support". While, in the far field, the two jets merge in a single more stable synthetic jet. Persoons et al. (2009) proposed two adjacent SJs with slot orifices and investigated the phase shift effect between the jets (0°, 60°, 120° and 180°) at nozzle-to-plate distances $H/D = 6$, 12 and 24, for dimensionless stroke length equal to 10, 29 and Reynolds number equal to 600, 750. At the optimal configuration, corresponding at $L_0/D = 29$, $Re = 600$, phase shift of 120° and a jet-to-surface spacing $H/D$ equal to 12, it was founded an enhancement of about 90 % in the average heat transfer rate compared to the corresponding single jet.

A comparison between a single circular SJ and twin circular SJs in phase opposition was performed by Greco et al. (2014). They performed heat transfer measurements at Reynolds number equal to 5100 and Strouhal number equal to 0.024 varying the jet axes distance and nozzle-to-plate distance. The results showed a general heat transfer gain achieved with the twin SJs, especially at lower jet-to-jet spacing. In a following work, Greco et al. (2016) investigated the flow field and they observed that, although the 180° phase-shifted SJs generate a destructive interaction causing a reduction of the phase-correlated velocity values, their interaction promotes the increase of turbulent fluctuations and axial velocity. It was also observed that during the suction phase, the twin synthetic jet has a saddle point that does not approach the impinging plate differently from the single configuration. This is relevant for a device which is supposed to be used as a cooling system, because the device prevents ingestion of hot air coming from the plate which has to be cooled. Recently, Paolillo et al. (2017) have proposed a quadruple SJ device. The effect of the phase delay on the flow field and on the acoustic noise was investigated at fixed Reynolds and Strouhal numbers of the single SJs, equal to 4000 and 0.2, respectively. The measurements showed a more complex evolution of the coherent vortices than the vortices of a single synthetic jet, since they result from the interaction of the vortex rings inherent to four different jets constituting the device. In the far field, the acoustic noise was reduced of about 14 dB in the 90° circularly-shifted-jets configuration with respect to the monopole configuration.

Other solutions include exit geometry modifications. From a practical point of view, these solutions are easier to make and at a relatively low cost because they rely merely on changes in the exit configuration.

The effect of the orifice shape on SJ-based impingement cooling was experimentally investigated, for the first time, by Chaudhari et al. (2010b). They considered different configurations consisting in square, circular, and rectangular orifice shapes. Experiments were undertaken at a Reynolds number ranging between 950 and 4000 while the dimensionless nozzle-to-plate distance varied between 1 and 25. A square orifice was found to perform better at axial distances larger than 5 diameters, while a rectangular orifice (with small aspect ratio 1–5.25) was found to be more effective at lower axial distances. Subsequently, Chaudhari et al. (2011) proposed a new solution, consisting in a centre orifice surrounded by azimuthally evenly spaced satellite orifices. Measurements, conducted for Reynolds number in the range of 1000–2600 and axial distance in the range of 1–30$D$, revealed that the number of satellite orifices affects the heat transfer coefficient at lower axial distances. The maximum heat transfer coefficient with multiple orifice synthetic jet was up to approximately 30 % greater than that obtained with a conventional single orifice synthetic jet. Later, the effect of the orifice shape was studied also by Bhapkar et al. (2014). They experimentally investigated and compared elliptic synthetic jets with circular, rectangular and square orifices having same equivalent diameter and constant input power supplied to the actuator. The effect of orifice shape, aspect ratio and operating parameters of the synthetic jet on acoustic and heat transfer performance was studied. It is found that irrespective of the shape of the orifice, the synthetic jet generates the minimum sound pressure level when operated at its resonance frequency. The maximum heat transfer enhancement is obtained at the resonance frequency for elliptical orifice of aspect ratio 1.4 at the dimensionless exit-to-plate distance of 3. For exit-to-plate distance $H/D < 6$, the elliptical exit performs better than the other shapes. The elliptical shape presents higher heat transfer rates than the rectangular exit used by Chaudhari et al. (2010b). This was mainly attributed to the enhanced mixing and the large entrainment generated by the elliptic geometry. For $H/D > 6$, circular and square exits outperform elliptic and rectangular jets heat transfer rates. This was mainly due to the high spreading rates because of which air loses its momentum before reaching the target plate. Later investigations were performed by Mangate and Chaudhari (2015) using diamond and oval shaped orifices, that confirmed the heat transfer enhancement with respect to a circular exit. At low axial distances, the maximum value of the average heat transfer coefficient was found to be 17 % higher in case of diamond shape orifice and 7 % higher in case of oval shape than a circular exit configuration with same hydraulic diameter. They did not carry out flow field measurements, but argued that probably the observed heat transfer features had to be ascribed to better entrainment and mixing properties within the jet in case of diamond and oval shape orifices.

## 1.3 Chevron technology

It is of paramount importance to be able to properly manipulate a flow field in order to achieve or improve some desired effects and to prevent or reduce side effects. The ability to control a flow, by manipulating its structure, is one of the most important topics in fluid dynamics. The control strategies are involved in several areas of application, such as: transition delay, separation prevention, drag reduction, lift augmentation, turbulence suppression, noise abatement, combustion efficiency, heat and mass transfer enhancement. A large amount of flow control solutions is available both for external and internal flows (Gad-el Hak, 2006). One of these solutions is the application of chevron elements which belong to the family of the axial vortex generators. This section provides an overview of the historical development and main underlying mechanisms of the chevron technology.

The technological development of the chevrons has its roots in a joint NASA/industry effort for acoustic issues. An explanation for the origin of sound generated from fluid streams was proposed by Lighthill (1952). According to Lighthill's analogy, the regular fluctuations or turbulence in the flow field are the sources of sound generation. Later, in 1964, the source of the acoustic noise was particularised in terms of vorticity dynamics by Powell (1964). In continuous jets, vortical structures can arise from shear layer instabilities or be induced by specific excitations. The implication of large-scale coherent flow structures in noise generation suggested that lower acoustic emissions might be achieved by modifying such structures. One of the earliest studies regarding jet noise reduction was carried out by Westley and Lilley (1952). They proposed a modification of the nozzle exit geometry applying small obstacles. These small protrusions into the flow, located at the nozzle edge were called “tabs”. Some of the tabs used by Westley and Lilley are reported in Figure 1.6. The acoustic noise abatement observed by these authors, led to several investigations on the acoustic effect of tabs (Nagel et al., 1983; Samimy et al., 1993; Bridges and Brown, 2004). Different shaped elements (like square, rectangle and triangular tabs) mounted at the nozzle exit with strong inclination towards the jet flow were studied. It was widely recognised that these tabs were effective in noise suppression. The term “chevron” appeared later (in the 1990s under the NASA’s High Speed Research Program and the Advanced Subsonic Technology Program (as reported by Zaman et al., 2011)) to indicate a sawtooth pattern at the nozzle exit edge, i.e. extensions of the nozzle wall into a continuous serrated edge with mild penetration into the flow with respect to the tabs.

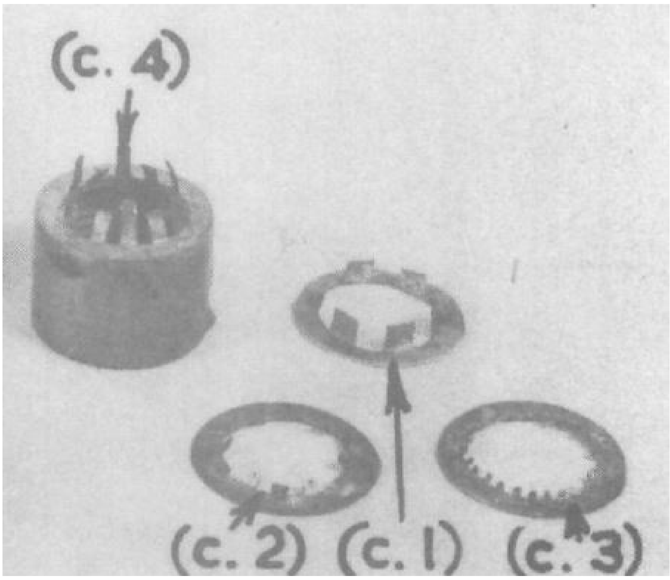

Figure 1.6: Noise reduction devices used by Westley and Lilley (1952), (adapted from Westley and Lilley, 1952).

Studies aimed at understanding the flow mechanisms were carried out. The work of Bradbury and Khadem (1975) is one of the first investigations on the effect of tabs on the flow field. Bradbury and Khadem noted that the main effect was the reduction of the jet potential core. The structure of jets issued from notched nozzles was studied by Pannu and Johannesen (1976). They observed a jet spread and low speed regions in the notch plane. The Schlieren images were used to provide a sketch of the jet structure and it was inferred the generation of streamwise vortices. The sketch of the jet structure proposed by Pannu and Johannesen is reported in Figure 1.7. During 1980s and 1990s, these findings encouraged several researchers to explore the effect of the tabs on the spreading and turbulent mixing enhancement in jets. The obtained results were so impressive that some research groups dubbed them as “super mixers” (Zaman et al., 2011). Flow mechanisms were investigated and reported in several works (Samimy et al., 1993; Zaman et al., 1994; Zaman, 1996; Reeder and Samimy, 1996).

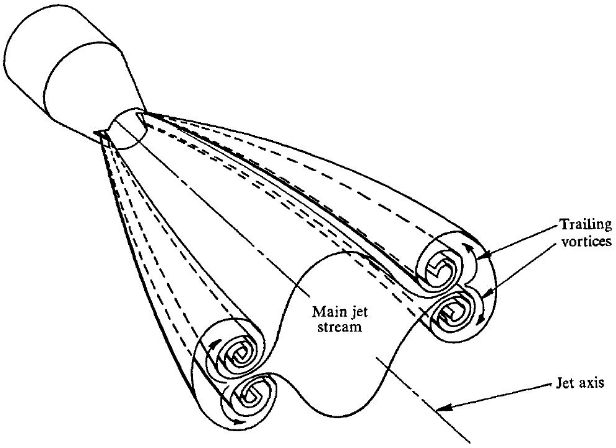

Figure 1.7: Sketch of jet structure, (Pannu and Johannesen, 1976).

During 1990s, first tests on engine models showed that their effect on the noise was mixed. The tabs suppressed the noise at low frequencies although a noise increase at higher frequencies was experienced. Parametric studies on tabs were carried out in various configurations. The design of the tabs was supported by computational fluid dynamics simulations. However, the complex noise generation mechanisms and the difficulty to relate simulations and noise prediction produced only a general idea: the rapid jet decay reduces low-frequency noise, while high turbulence level near the nozzle exit increases high-frequency noise. The results on some tests, conducted under NASA programmes, were encouraging, but the thrust loss had to be evaluated. So, in 1998, static and flight tests evaluated small thrust penalty values under 0.1 % for some cases. The studies showed that a slight variation in the chevron geometry produces large effects on the noise and thrust penalty. A complete knowledge of their aerodynamics and acoustics is far from being achieved. This notwithstanding, further static measurements and flight tests on best-performing configurations culminated in the first commercial engine with chevron nozzle. In 2003, the Bombardier CRJ 9000 was the first aircraft with an engine equipped with chevrons. Nowadays, the chevrons elements are applied on several aero engines as shown in Figure 1.8. A more detailed review on the history of the development from tab elements to chevrons is given by Zaman et al. (2011).

(a) (b)

Figure 1.8: Boeing (a) 737 and (b) 777 engines equipped with chevrons, (adapted from Boeing; NASA).

From a fluid dynamics standpoint, there is a huge amount of works dealing with the effect of vortex generators; for this reason only few relevant works are reported in the following. These devices are essentially responsible for the generation of streamwise vortices. Zaman et al. (1994) and Reeder and Samimy (1996) proposed two sources of formation of the streamwise vortices. The first source is due to a pressure hill occurring within the nozzle upstream of the tab and in this case, the pressure gradient and the no-slip condition at the wall produce a pair of vortices. The other source consists in the reorientation, at the edge of the chevrons, of the vortex filaments on the internal wall of the nozzle. These streamwise vortices can be controlled by acting on the geometric parameters of the vortex generator elements. Zaman (1996) studied the effects of the vortex generators placed at the edge of a rectangular nozzle in a periodically pulsed jet. It was observed a deformation and reorientation of the rolled-up azimuthal vortical structure which undergoes the axis-switching phenomenon. Zaman showed that the axis-switching, caused by the dynamic of the azimuthal vortical structures, can be controlled acting on the number and location of the vortex generators. On the same line of research, Grinstein et al. (1996) conducted a study on a round jet excited by an acoustic driver and equipped with vortex generators installed upstream of the nozzle exit. Numerical simulations and experiments of reactive (burner configuration) and non-reactive free jets were carried out. In these experiments, the flow field is characterised by the self-deformation of a non-circular vortex ring. The dynamics of the large coherent structures affects the mixing pattern resulting in regions of localised inactive combustion and regions with enhanced mixing and entrainment corresponding to intense combustion areas. The mixing enhancement mechanisms associated with streamwise vortices were computationally and experimentally studied by Waitz et al. (1997). They stated that the mixing enhancement is caused by two main phenomena: the increase of the interfacial surface area between two regions containing fluid with different properties (e.g. chemical composition, momentum or energy) and the increase of the magnitude of local gradients in the direction normal to the interface.

Focusing on the chevron nozzle, Violato and Scarano (2011) investigated the three-dimensional flow field topology of a continuous jet with six-chevrons exit, at Reynolds number equal to 5000, comparing it to a conventional circular jet at the same Reynolds number. The most prominent unsteady feature exhibited by the circular jet flow is the shedding of vortex rings that result from the growth of Kelvin-Helmholtz instabilities. Streamwise structures of axial and radial vorticity are also observed in the outer region and they move inward and outward under the effect of the Kelvin-Helmholtz instabilities. The flow topology of the chevron jet differs from the circular jet. The axisymmetric ring-like coherence of the vortices which develop in a circular jet is replaced by streamwise oriented vortices with a quasi-steady behaviour. Figure 1.9 illustrates the time sequence of the large coherent structures evolution for both circular and chevron synthetic jets (Violato and Scarano, 2011).

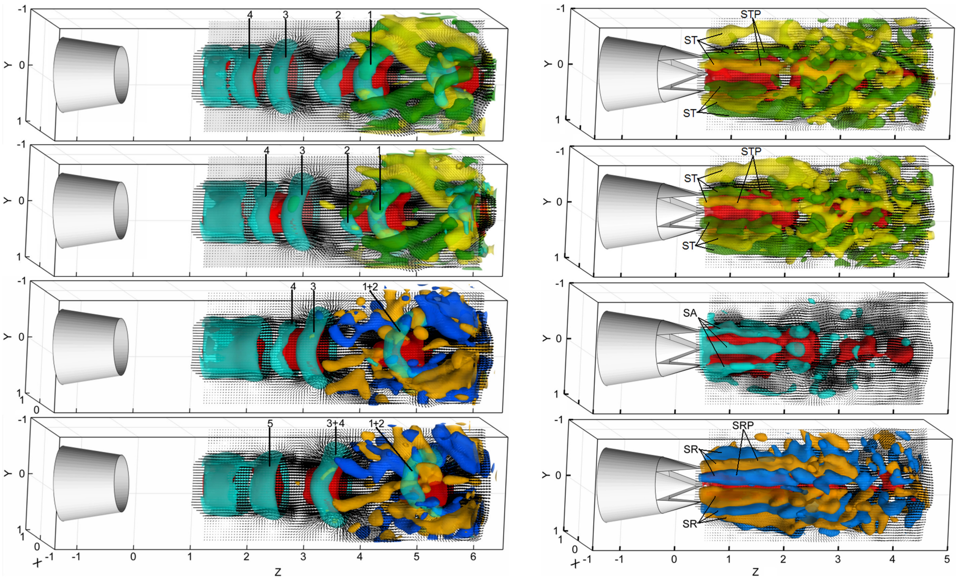

(a) (b)

Figure 1.9: Time sequence visualisation of the (a) circular and (b) chevron jet. Velocity vector slice in the axial plane. Iso-surfaces of axial velocity (red). In the first two snapshots, iso-surface of azimuthal (cyan), axial negative (green) and positive (yellow) vorticity components; in the last two snapshots, iso-surfaces of azimuthal (cyan), radial negative (blue) and positive (orange) vorticity components. (Adapted from Violato and Scarano, 2011).

Later, Violato et al. (2012) experimentally studied the impinging flow field and the associated heat transfer features of chevron jets compared to circular jets. On the impingement plate, the chevron jet presents a more homogeneous organisation than the circular one with streamwise vortices scattered all over the region of impingement. In contrast with the circular case, the radial convective velocity of the vortices is highly fluctuating and the heat transfer rate is enhanced in presence of the chevron nozzle. At the centre of the impingement area, the chevron jet exhibited larger heat transfer rate than the circular jet, with a maximum enhancement of 44 %. According to Violato et al. (2012), the enhancement is caused by the development of streamwise vortices which, compared with the toroidal vortices, are associated with a deeper penetration of turbulent induced mixing and higher arrival speed.

The beneficial impact of these devices on the spreading, mixing and entrainment of CJs leads to study the effect of the chevrons on SJs.

## 1.4 Objectives of the thesis

In view of the effects of a chevron exit on the flow field and heat transfer properties of continuous jets, a question arises as to whether the chevrons could produce a significant change in synthetic jets.

Two main objectives are pursued in this thesis. The first one is to investigate the 3D evolution of large-scale structures in chevron synthetic jets at moderate Reynolds number using Stereoscopic PIV (Stereo-PIV). Circular and six-chevron synthetic jets are compared. The focus is placed on the evolution of the coherent structures.

The second objective is to study the heat transfer characteristics of the chevron synthetic jet and the relation between the impinging flow field features and the heat transfer performance.

## 1.5 Outline of the thesis

The remaining of this thesis is structured as follows. The following two chapters explain the experimental measurement techniques employed. Chapter

2 describes the working principle of planar and Stereo-PIV. Chapter 3 describes the use of Infrared (IR) thermography for thermo-fluid-dynamic applications and the heated thin foil heat flux sensor. The results are shown in the subsequent three chapters. The 3D large-scale organisation of the chevron synthetic jet and a comparison between the circular and the chevron configurations are presented in Chapter 4. Then, the heat transfer characteristics of a chevron synthetic jet are presented in Chapter 5, along with a comparison between the heat transfer performance of circular and chevron synthetic jets. Chapter 6 describes the relation between the impinging flow field and the heat transfer features. Finally, in Chapter 7, the conclusions are drawn and future perspective are proposed.

# Chapter 2

# Particle image velocimetry

In this chapter the basic principles of Particle Image Velocimetry (PIV) will be presented and discussed. Some of the main aspects that are taken into account when designing either a planar or stereoscopic PIV experiment are introduced. More details can be found in Raffel et al. (2007).

## 2.1 Basic principles

Particle image velocimetry (PIV) is an optical, laser-based anemometry technique, able to provide velocity vector field by analysing couples of images of illuminated tracer particles inserted into the flow and carried by the fluid. It is possible to obtain the instantaneous velocity vector field by evaluating the particle image shift between the two recorded images. From the previous sentence, it is clear that to perform PIV measurements, some ingredients are required: a seeding system to insert tracer particles within the flow, an illumination system for illuminating the tracer particles, an imaging and recording system that allows to record the light scattered by the tracers and calculation methods for PIV image evaluation. Schematic of experimental arrangement of a PIV experiment in a wind tunnel is sketched in Figure 2.1. The pulsed light source is collimated in a light sheet that illuminates the tracer particles. These particles have to accurately follow the flow and to present good light scattering properties. The light scattered by the particles is recorded on a camera. The local fluid velocity is measured indirectly

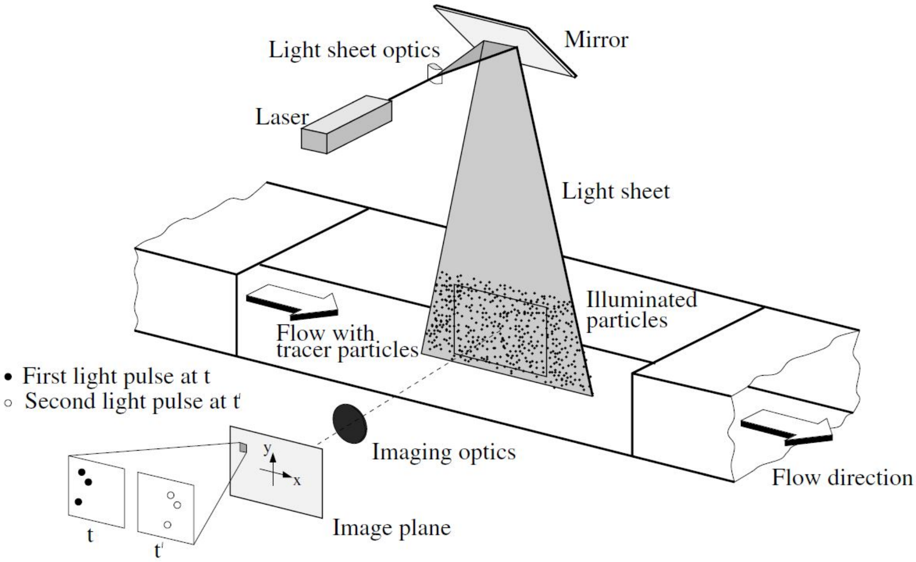

Figure 2.1: Schematic sketch of PIV setup, (Raffel et al., 2007).

as a function of the tracer displacement occurring in the time interval between two laser pulses. The local displacement vector for the images of the tracer particles of the first and second illumination is evaluated by computer algorithms. The recorded images are divided in so-called interrogation windows and for each interrogation window a statistical auto-correlation (in case of double-exposure single-frame) or cross-correlation (in case of single-exposure double-frame) allows to determine the displacement vector (Raffel et al., 2007). At this stage, the velocity vector can be evaluated as

$$\begin{pmatrix} u \\ v \end{pmatrix} = \frac{M}{\Delta t} \begin{Bmatrix} \Delta_x \\ \Delta_y \end{Bmatrix} \tag{2.1}$$

where $u$ and $v$ are the local velocity components in the real or object plane, $\Delta t$ is the time separation between the two laser pulses, $\Delta_x$ and $\Delta_y$ are the local displacement components in the image plane and $M$ is the magnification factor from the object plane to the image plane, taken to be constant in the absence of aberrations and misalignment. The magnification factor is the ratio of the distance between the image plane and the lens to the distance between the object plane and the lens.

### 2.1.1 Particles: properties and imaging

To be precise, PIV technique determines the tracer particles velocity instead of the fluid velocity. Therefore, the tracer particles must be able to follow the flow as accurately as possible without perturbing it. A convenient parameter to measure the tendency of tracers particles to attain equilibrium with the fluid is the relaxation time:

$$\tau = d_p^2 \frac{\rho_p}{18\mu} \tag{2.2}$$

where $d_p$ is the diameter of the particle, $\rho_p$ the density of the particle. Equation 2.2 shows the dependence of the relaxation time on particle and fluid characteristics. The tracer particles present a better tendency to follow the flow for small relaxation time values. In particular, the Stokes number, $Stk = \tau/\tau_{flow}$ where $\tau_{flow}$ is a characteristic time of the flow, expresses the fidelity of particle tracers in the specific flow experiment. Some properties of relevant PIV tracer particles are summarised in Table 2.1.

Table 2.1: Seeding materials for gas flows, (adapted from Melling, 1997).

| Material | Density ($\mathrm{kg\,m^{-2}}$) | Viscosity ($\mathrm{m^2\,s^{-1}}$) | Mean diameter (µm) |
|---|---|---|---|
| $TiO_2$ | 3500 | $1.50 \times 10^{-5}$ | 0.45–1.44 |
| $Al_2O_3$ | 3970 | $3.00 \times 10^{-4}$ | 0.78–2.46 |
| Glass | 2600 | $1.50 \times 10^{-5}$ | 0.53–1.67 |
| Microballon | 100 | $1.50 \times 10^{-5}$ | 2.69–8.50 |
| Olive oil | 970 | $1.45 \times 10^{-5}$ | 0.98–3.09 |

The PIV experiments in the present thesis, as most of the PIV measurements of air flow, use olive oil particles as tracer particles. These particles, in addition to the advantage of very small relaxation time and $Stk < 0.1$, are not toxic and they hold their dimensions for long time and for a wide range of external conditions.

The velocity measurement accuracy strongly depends also on the particle image diameter. The image of the tracer particles on the camera sensor is associated to the actual geometry of the particle and the light scattering properties of the particles. An estimate of the particle image diameter is given by Adrian and Yao (1985):

$$d_\tau = \sqrt{d_{geom}^2 + d_{diff}^2} = \sqrt{(Md_p)^2 + (2.44 f_\#(M+1)\lambda)^2} \tag{2.3}$$

being $d_{geom}$ the geometric image diameter of the particle obtained with a magnification $M$, $d_{diff}$ the diffraction image diameter obtained approximating the intensity distribution with a Gaussian curve, $f_\#$ the f-number or f-stop, defined as the ratio between the focal length and the aperture diameter and $\lambda$ the wavelength of the illuminating source. Whilst the particle dimension $d_\tau$ should be as small as possible to reduce the uncertainties in the displacement determination, it should be not smaller than 2 pixels to avoid problems that arise when the particle dimension is too small, as the peak-locking.

Considering the imaging of objects, the best focusing is obtained at the position where the rays, coming from the object, intersect after having passed through the lens. If the distance between the lens and the imaging plane (i.e. camera sensor) is not perfectly adjusted, the geometric image is blurred. It is important to introduce the depth of field, defined as the distance along the lens optical axis on which the blur spot size does not exceed a threshold. The depth of field can be estimated as follow:

$$\delta z = 2 f_\# d_{diff} \frac{1+M}{M^2} = 4.88 f_\#^2 \lambda \frac{(1+M)^2}{M^2} \tag{2.4}$$

### 2.1.2 Illumination and recording system

The illumination of the particles occurs by means of a thin light sheet. Due to the requirement of high energy density pulses, pulsed lasers represent the illuminating source for PIV application. The illumination pulse duration must be short enough to “freeze” the motion of the particles during the pulse exposure in order to avoid blurring of the images. Moreover, the time delay between the illumination pulses must be long enough to determine the particles’ displacement between the images with a sufficient resolution. On the other hand, it must be short enough to avoid particles with an out-of-plane velocity component to leave the light sheet between the two subsequent illuminations.

Generally, neodymium-doped yttrium aluminium garnet lasers (Nd:YAG lasers with $\lambda = 1064\,\mathrm{nm}$ or $\lambda = 532\,\mathrm{nm}$) are used in applications at working frequency ranging between 1 Hz and 15 Hz. The released energy per pulse ranges between $100\,mJ/pulse$ and $800\,mJ/pulse$. Neodymium-doped yttrium lithium fluoride lasers (Nd:YLF lasers with $\lambda = 1053\,\mathrm{nm}$ or $\lambda = 526\,\mathrm{nm}$) are employed for high frequency applications, being the working frequency up to 10 kHz. The released energy per pulse is lower, at most $30\,mJ/pulse$, compared to the low frequency laser.

Typical laser beam diameters are of about 10 mm at the laser output, therefore the illumination of the tracer particles by a thin laser sheet is achieved by a combination of lenses. Then, the images of the tracer particles are collected by using cameras. In the past, photographic films were used to record the images. Technological development in electronics drew the attention from analog film cameras to digital ones. Nowadays, the most common cameras are charge coupled device (CCD) and complementary metal-oxide-semiconductor (CMOS). Typically, the sensor size is around 1-16 Mpx and the acquisition frequency, obviously, tuned with the illumination system.

### 2.1.3 Statistical PIV evaluation

Once two images of the particles illuminated by the laser sheet are recorded with a small time separation, a double distribution of light intensity on a grid of points is obtained. Individual particles can be detected, but it is difficult to identify particle images pairs throughout the double recorded frames. So, the tracking of the motion of ensembles of particle images contained in a small portion of the grid, called interrogation window, is evaluated. The determination of the displacement relies on the statistical operator of correlation.

Consider two intensity distribution $I_1(x_i, y_j)$ and $I_2(x_i, y_j)$ subdivided in interrogation windows, the normalised function of cross-correlation is computed as

$$R_c(\Delta_x, \Delta_y) = \frac{\sum_i \sum_j [I_1(i,j) - \bar{I}_1][I_2(i+\Delta_x, j+\Delta_y) - \bar{I}_2]}{\sqrt{\sum_i \sum_j [I_1(i,j) - \bar{I}_1]^2 \cdot \sum_i \sum_j [I_2(i+\Delta_x, j+\Delta_y) - \bar{I}_2]^2}} \tag{2.5}$$

where $\bar{I}_1$ and $\bar{I}_2$ are the average intensities in the interrogation windows, $\Delta_x$ and $\Delta_y$ the image pixel shifts. This operator gives the position of the correlation peak. The position of the correlation peak is assumed as linear shift approximation. For laser separation pulses small enough, the linear approximation is valid also for the particles motion. Knowing the pulses separation time, the velocity can be estimated. The evaluation of the PIV recordings is illustrated in more detail in Figure 2.2.

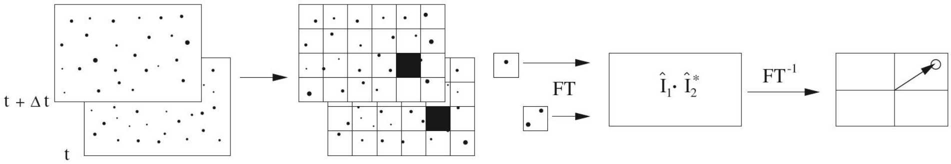

Figure 2.2: Analysis of double frame single exposure recordings, (Raffel et al., 2007).

## 2.2 Stereoscopic PIV

So far, the PIV method described allows recording the projection of the velocity vector into the plane of the light sheet. The particles movement through the laser sheet, named out-of-plane displacement, introduces some limitations. The out-of-plane loss of pairs in two recorded frames reduces the signal-to-noise ratio and, as a consequence, the accuracy in detecting the correlation peak location (Raffel et al., 2007). Another limitation is the perspective error, shown in Figure 2.3. A particle displacement in the laser thickness direction influences the particle image displacement, especially at the edges of the field of view (FOV). This effect introduces an uncertainty in measuring the in-plane velocity components. Furthermore, it is often required to extract 3D information due to the complexity of the phenomenon. These aspects have led to the development of the stereoscopic particle image velocimetry.

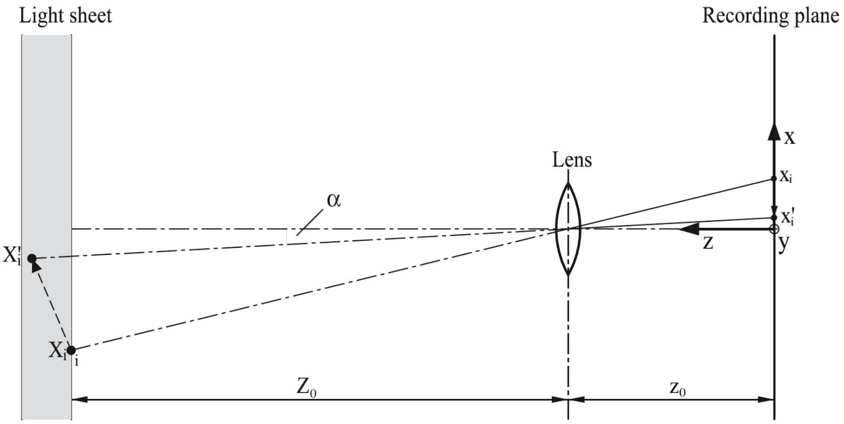

Figure 2.3: Imaging of a particle within the light sheet on the recording plane, (Raffel et al., 2007).

Stereoscopic PIV (Stereo-PIV) is useful to partially overcome limitations of classical PIV and it is able to measure the three-dimensional velocity components in the measurement plane (two-dimension three-component). When measuring three-dimensional particle displacement, one may characterise this situation as having three unknowns ($\Delta_x$, $\Delta_y$ and $\Delta_z$) with the single view providing only two equations as reported in Equation 2.1. Stereo-PIV eliminates this problem by acquiring two simultaneous views along different directions as shown in Figure 2.4. The reconstruction of the three-dimensional displacement field is performed from the two projected, planar displacement fields.

A Stereo-PIV configuration, consisting in a simple translation system, has the advantages of uniform magnification, but the common imaged area is limited. This configuration is sketched in Figure 2.5a. Moreover, as the angle subtended between the two optical axes of the cameras reduces, large errors in the measurement of the out-of-plane velocity component occur. An alternative configuration is represented by the angular lens displacement

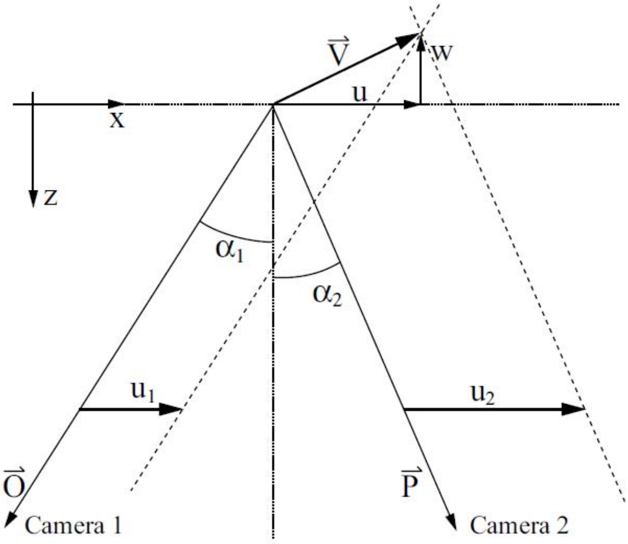

Figure 2.4: Stereo viewing geometry in the x-z plane, (Raffel et al., 2007).

configuration, in Figure 2.5b. The Scheimpflug condition is satisfied when, rotating the lenses with respect to the sensor, the focal plane, the lens plane and the target plane will converge into one straight line. This configuration has a no constant magnification across the FOV, but in return the measurement precision of the out-of-plane velocity component can be increased setting the opening angle between the two cameras as near as possible to 90°.

The images of each camera are individually cross-correlated. Subsequently, each image plane is combined to evaluate the three-dimensional data reconstruction. Prasad (2000) classified the stereoscopic reconstruction methods in geometric and calibration-based. Only a calibration-based method will be discussed, because many studies have demonstrated its superiority in terms of accuracy.

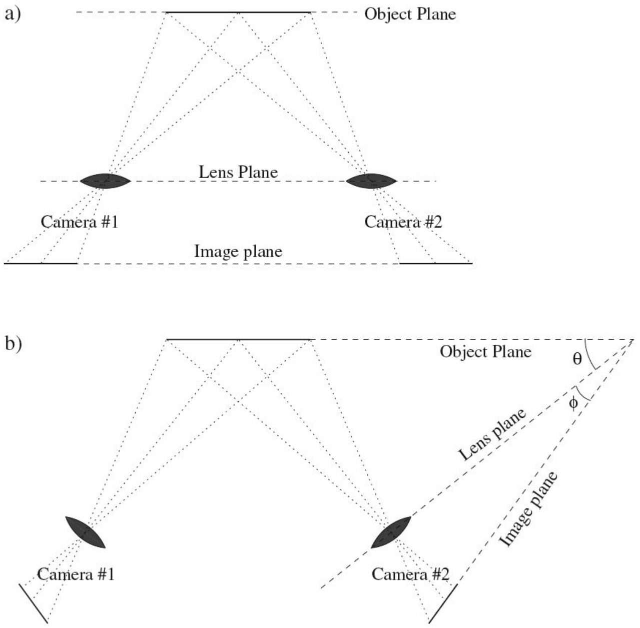

Figure 2.5: Basic Stereo-PIV arrangements: (a) translation displacement, (b) angular displacement with Scheimpflug condition, (Raffel et al., 2007).

### 2.2.1 Optical calibration and reconstruction

The calibration procedure consists in the determination of the correspondence function **F** between object coordinates $\underline{X}$ and image coordinates $\underline{x}$:

$$\underline{X} = \mathbf{F}(\underline{x}) \tag{2.6}$$

The calibration consists in placing a calibration target in object plane, with known position and high-contrasted known markers. The target has to coincide with the laser sheet. Once the markers are identified on the images, a discrete correspondence between real and image planes is obtained. A regression procedure is then used to fit a chosen function for the mapping function **F**. One of the most adopted model for **F** is the pinhole camera model.

Then, the 3C velocity field reconstruction is performed. A reconstruction technique requires that the images are de-warped onto a common grid in the physical space, and then interrogated with a standard PIV algorithm. The three component displacement is obtained by using geometrical relations (Willert, 1997).

### 2.2.2 Disparity correction and self-calibration

The misalignment between the calibration plate and the laser sheet, shown in Figure 2.6, represents one of the main sources of error in Stereo-PIV.

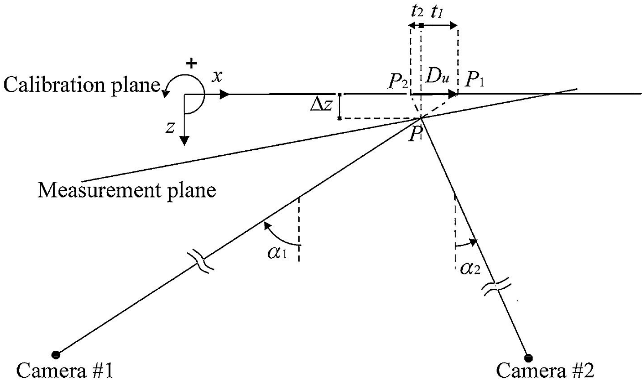

Figure 2.6: Sketch of a generic misalignment error between calibration and measurement plane, (Giordano and Astarita, 2009).

The misalignment error affects the true position of the light sheet in space and the dewarping of images. Typically, in order to correct for the residual misalignment, a disparity correction is applied.

Willert (1997) proposed a procedure based on cross-correlation of the simultaneous dewarped images of the two cameras in the object plane $z = 0$; the local misalignments (also referred as disparity map) are used to correct the position errors. Wieneke (2005) proposed a procedure accounting also for the reconstruction error. The disparity map is used to estimate the position of the measurement plane; subsequently, the mapping function is modified so that the measurement plane will be coincident with the target plane $z = 0$. This procedure is called self-calibration procedure.

## 2.3 Stereo-PIV algorithm

The Stereo-PIV procedure used in the present thesis consists of three main steps: the correction of the misalignment error between calibration and measurement planes (Figure 2.7), PIV cross-correlation and 3C displacement reconstruction. In particular, the Stereo-PIV steps are:

- Calibration: a mapping function, which transforms the object coordinates into the image coordinates of camera 1 and of camera 2, is computed.

- Dewarping: the two dewarped images recorded at the same instant by the two cameras are compared with a PIV process based on the iterative image deformation method (Astarita, 2006).

- Disparity: the disparity map can be computed and used to evaluate the local misalignment by means of triangulation.

- Measurement plane: the equation of the measurement plane in the object space is computed by means of a regression method. The above steps are iterated to obtain a better accuracy in the determination of the measurement plane equation.

- PIV cross-correlation: the images of each camera are dewarped on the correct measurement plane onto a common grid in the physical space. A PIV cross-correlation algorithm, detailed in Astarita (2008), is applied individually for each camera.

- Three component displacement reconstruction: finally, the three component displacement is obtained by using geometrical relations (Willert, 1997; Giordano and Astarita, 2009).

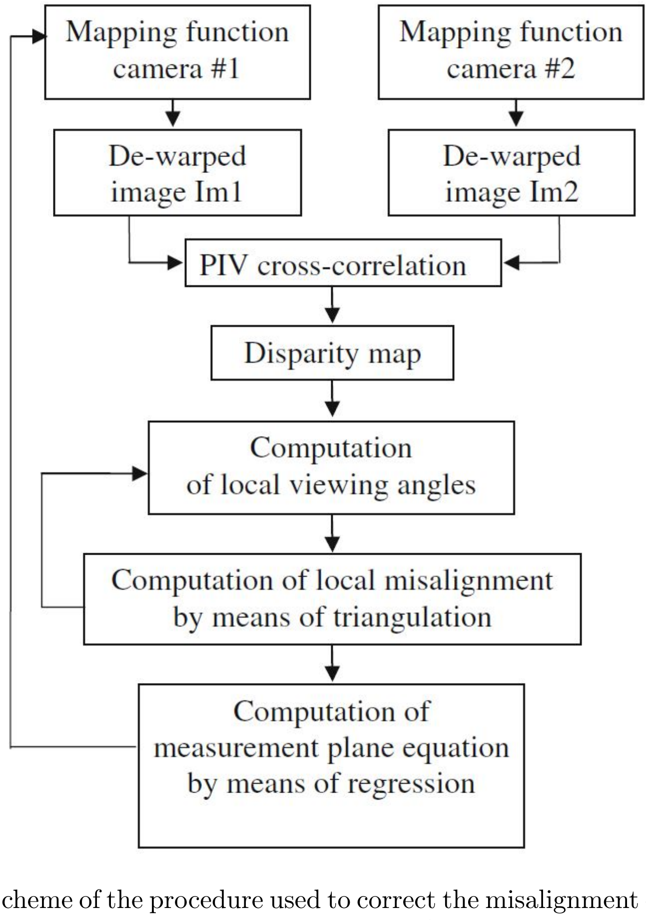

Figure 2.7: Scheme of the procedure used to correct the misalignment error between calibration and measurement planes, (Giordano and Astarita, 2009).

# Chapter 3

# IR thermography for convective heat transfer measurements

IR Thermography for fluid dynamics applications is presented. At the beginning, theoretical aspects of the energy transport that occur by means of radiation are briefly drawn. Afterwards, the main features characterising an IR scanner are presented. Finally, the application of IR cameras for the measurement of the convective heat flux in fluid dynamics will be discussed. In particular, the heated thin foil heat flux sensor is described. For more details, the reader is referred to the book by Astarita and Carlomagno (2012).

## 3.1 Background of radiation heat transfer

Energy exchange is related to work and heat transfer. Focusing the attention on the thermal energy, the main exchange mechanisms involved are convection, conduction and radiation. Heat transfer by radiation is an energy transport mechanism that occurs by means of electromagnetic waves. Differently than heat conduction and convection, energy can be transmitted by thermal radiation in the absence of a medium. If a medium is present, the transferred energy may be or not be downgraded. In the first case, the medium is called partially transparent, i.e. it allows only a fraction of the transmitted energy to pass through. In the latter case, it is said fully transparent medium and the whole amount of energy is transmitted through it.

Thermal radiation is electromagnetic radiation generated by the thermal motion of charged particles in matter. All matter with a temperature greater than absolute zero 0 K emits thermal radiation. The amount of energy transported by electromagnetic radiation depends on several parameters such as the surface finish, thermodynamic state, the material and the wavelength of the electromagnetic wave. The wavelength $\lambda$, the frequency $\nu$ and the speed of propagation $c$ of an electromagnetic wave through a medium (with index of refraction $n$) are related as follows:

$$\lambda = \frac{c}{\nu} = \frac{c_0}{\nu n} \tag{3.1}$$

being $c_0$ the speed of propagation of light in vacuum ($2.998 \times 10^8\ \mathrm{m\,s^{-1}}$). Both $c$ and $\lambda$ depend on the nature of the medium through which the wave travels, $\nu$ is dependent only on the source of the electromagnetic wave.

The electromagnetic spectrum extends from small wavelength to large ones and it is reported in Figure 3.1. It is divided in a number di wavelength intervals, called spectral bands. The thermal radiation band is conventionally defined as a relatively small fraction of the complete spectrum, positioned between 0.1 µm and 1000 µm, which includes part of the ultraviolet and all of the visible and infrared (IR) bands. In particular, most of the thermal energy is transported by electromagnetic waves at wavelength in the infrared spectral band. This band is subdivided into four sub-bands: near infrared (0.76 µm–3 µm), middle infrared (3 µm–6 µm), far infrared (6 µm–15 µm) and extreme infrared (15 µm–1000 µm).

In general, the energy transported by radiations may be absorbed, reflected or pass through a body. By indicating with $\alpha_r$ the amount of incident radiation absorbed by a body, $\rho_r$ the radiation reflected by a body and $\tau_r$ the fraction of radiation transmitted through a body, the energy conservation requires:

$$\alpha_r + \rho_r + \tau_r = 1 \tag{3.2}$$

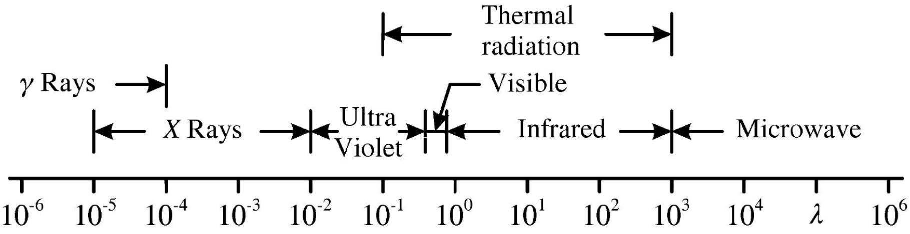

Figure 3.1: Electromagnetic spectrum (wavelength $\lambda$ in µm), (Astarita and Carlomagno, 2012).

where $\alpha_r$, $\rho_r$ and $\tau_r$ are respectively called absorptivity, reflectivity and transmissivity coefficients of the body. Clearly, these coefficients are non-negative and smaller than, or at most equal to 1. Completely non-transparent bodies are called opaque bodies and in such case $\tau_r = 0$. An opaque body at a certain temperature emits from its surface radiations in all directions and at different wavelengths. The amount of energy emitted by radiation depends on the material, surface characteristics, surface finish as already mentioned.

It is useful to introduce the concept of black body. General laws for thermal radiation of black body can be set out and then extended to real bodies. Black body is defined as a perfect emitter and absorber of radiations. For a black body $\alpha_r = 1$ and, consequently, $\tau_r = \rho_r = 0$. A black body is able to absorb all the incident radiation, regardless of its wavelength and direction, and is the body that, for a fixed temperature and wavelength, emits the maximum of radiation.

Planck's law of radiation permits to evaluate the energy flux at fixed wavelength which is emitted by a black body in vacuum:

$$E_{b\lambda}(\lambda, T) = \frac{C_1}{\lambda^5 (e^{\frac{C_2}{\lambda T}} - 1)} \tag{3.3}$$

where $T$ is the absolute body temperature, $C_1 = 3.742 \times 10^{-6}\mathrm{W\,m^2}$ and $C_2 = 1.439 \times 10^{-2}\mathrm{K\,m}$ are the first and second radiation constants. Figure 3.2 displays the spectral black body emissive power's dependence on wavelength for several absolute temperature values. There is an appreciable shift of the maximum in the spectral power towards smaller wavelengths as the absolute temperature increases.

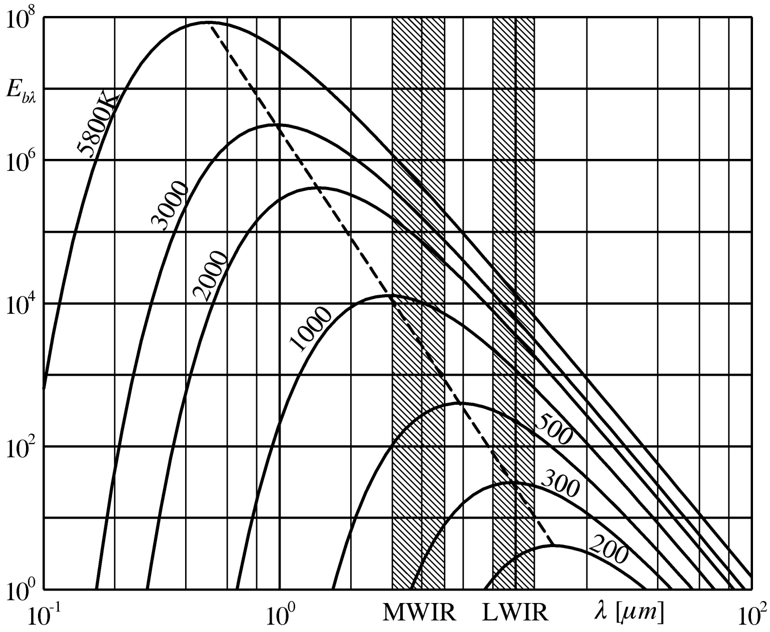

Figure 3.2: Spectral hemispherical black body emissive power ($\mathrm{W\,m^{-2}\,\mu m^{-1}}$) in vacuum for several absolute temperature (K) values as a function of the wavelength, (Astarita and Carlomagno, 2012).

For standard thermo-fluid-dynamic applications, most of energy is emitted in the middle or long infrared spectral band. Therefore, for these applications, IR cameras are sensitive in the middle (MWIR) or the long wavelength (LWIR). There are no IR cameras working around 5 µm–7.5 µm, because of the high atmospheric absorption in this range.

The locus of the points that individuate the maxima of Planck's law as a function of the absolute temperature (dashed line in Figure 3.2) is represented by Wien's law:

$$\lambda_{max} T = 2898\,\mathrm{\mu m\,K} \tag{3.4}$$

Equation 3.4 allows to find the wavelength at which a black body emits its maximum spectral emissive power at a given temperature.

The Stefan-Boltzmann law can be obtained integrating Planck's law of radiation. Stefan-Boltzmann law permits to calculate the total (energy flux over all wavelengths) black body hemispherical emissive power:

$$E_b = \int_0^\infty E_{b\lambda}(\lambda, T) d\lambda = \sigma T^4 \tag{3.5}$$

where $\sigma = 5.670 \times 10^{-8}\,\mathrm{W/(m^2K^4)}$ is the Stefan–Boltzmann constant.

The emission from real opaque bodies, both on a total and spectral basis, is different from that of a black body and does not definitely follow the aforementioned laws. The radiation emitted by a real body is only a fraction of the radiation emitted by a black body at the same conditions. To take into account this fraction, the spectral hemispherical emissivity coefficient $\epsilon_\lambda$ is introduced:

$$\epsilon_\lambda = \frac{E_\lambda(\lambda, T)}{E_{b\lambda}(\lambda, T)} \tag{3.6}$$

Similarly, the total hemispherical emissivity coefficient $\epsilon_t$ is defined as:

$$\epsilon_t = \frac{E_(T)}{E_b(T)} \tag{3.7}$$

The emissivity coefficient is a function of the angle between the direction normal to the emitting surface and the direction of the emitted radiation. When this dependency does not occur, the body is a diffuse emitter. The spectral emissivity of a body is also dependent on the wavelength of the emitted radiation, the emitting body material and the conditions of its surface. A body whose spectral emissivity is independent on the wavelength is called grey body. Although a proper grey body does not exist, it often occurs that a real surface may have a quite constant emissivity over the used IR detector band, thus allowing to consider the grey hypothesis as satisfied.

Kirchhoff's law states that for diffuse emission the spectral emissivity coefficient $\epsilon_\lambda$ is equal to the spectral absorptivity coefficient $\alpha_{r\lambda}$, which is the absorbed fraction of the radiation at a certain wavelength

$$\epsilon_\lambda + \rho_{r\lambda} = 1 \tag{3.8}$$

This leads to the consideration that bodies with low emissivity emit less energy and reflect a large amount of the radiation impinging on them.

## 3.2 IR scanner

IR scanner (camera) is a temperature transducer. Compared to standard techniques, the use of an IR camera produces a 2D temperature map, non-intrusive, high sensitivity and low time response measurements. IR camera allows accurate measurements of surface temperature maps even in the presence of relatively high spatial gradients.

A schematic representation of the main components of an IR camera is shown in Figure 3.3. Thermal radiation is conveyed by an optical system into a temperature detector that is sensible to the proper IR band. The electric signal generated by the detector is acquired by a video frame grabber and is processed by a dedicated electronic board in order to obtain a temperature map of the scanned area.

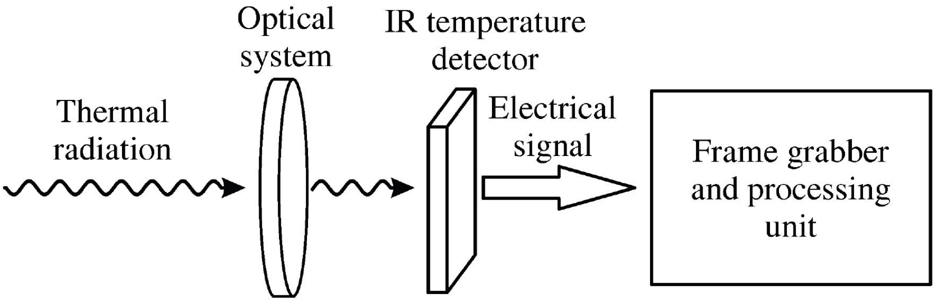

Figure 3.3: Sketch of the main systems that characterise an IR camera, (Astarita and Carlomagno, 2012).

### 3.2.1 Thermal sensitivity

Thermal sensitivity is generally expressed in terms of mean noise equivalent temperature difference (NETD), which is correctly defined as the time standard deviation of the random background noise averaged over all pixels of a black body scene (Levesque et al., 2005). The NETD is a function of the used black body temperature and, normally, the camera manufacturer provides it at ambient temperature in terms of mK.

At an ambient temperature of 20 °C, modern uncooled IR scanners have a typical NETD value of about 30 mK while cooled detectors may be as low as 10 mK. The thermal sensitivity decreases upon increasing the spatial frequency of the input thermal signal and for this reason it may be expressed also in terms of minimum resolvable temperature difference (MRTD), which is the minimal temperature difference of a 4-bar target detectable by the operator. A similar index is the minimum detectable temperature difference (MDTD) for which a series of circular targets are used instead of the 4-bar one. Both indices are equivalent to the NETD for low spatial frequencies.

### 3.2.2 Spatial resolution

The spatial resolution represents the capability of an IR scanner to measure surface temperature differences between points placed at relatively small distances. A coarse definition of the spatial resolution is based on the instantaneous field of view (IFOV) defined as the ratio of the detector size width over the lens focal length and is normally expressed in mrad. However, this is only an ideal design parameter and does not fully describe the performance of the IR scanner.

Since the lens focal length can be changed, a proper definition of the spatial resolution of an IR camera has to be given in terms of the scanner Modulation Transfer Function (MTF), which is the magnitude of the normalized complete Optical Transfer Function (OTF). A physical meaning to the definition of spatial resolution in terms of MTF can be given considering a sinusoidal temperature signal of amplitude $I$ as represented in Figure 3.4 that is only a function of the $x$ coordinate. The measured temperature signal exhibits a smaller amplitude $M$, which is generally referred to as modulation. The modulation, is generally a decreasing function of the signal spatial frequency. For each spatial frequency, the modulation transfer function is defined as the ratio between the recorded and the input sine wave amplitudes $M/I$. A source of modulation comes from the distortion and diffraction of the optical system but usually also the detector pixel dimension can play a fundamental role.

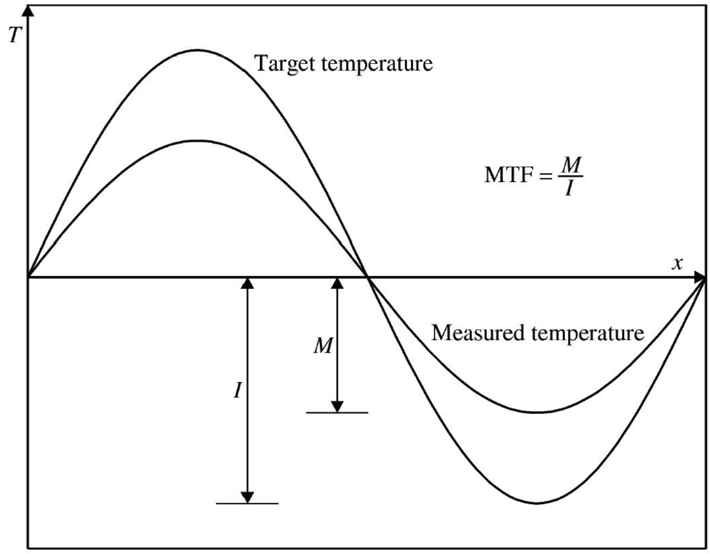

Figure 3.4: Illustration of the modulation effect, (Astarita and Carlomagno, 2012).

In Figure 3.5 the measured modulation of an IR scanner, based on a 1024 × 1024 square pixels quantum well infrared photodetector detector operating in the MWIR band, is shown as a function of the spatial frequency normalised with respect to the Nyquist frequency (1/2 pixel pitch, 25.6 cycles/mm). As the spatial frequency increases, the modulation becomes more and more severe, i.e. the damping increases.

### 3.2.3 Acquisition frequency

The acquisition frequency is an important parameter for the study of transient phenomena in thermo-fluid dynamics and is mainly connected with the detector response time. Normally, this parameter is reported as the rate of acquisition of a complete thermal image in terms of the number of full frames acquired per second (Hz). This value varies from few Hz up to tens of thousands of Hz. It should be noted that the maximum acquisition frequency is limited by the minimum integration time needed by a detector

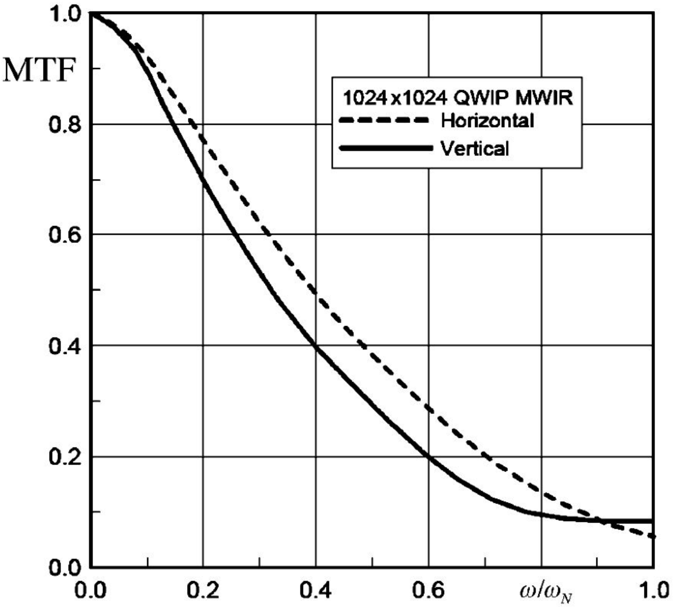

Figure 3.5: Scanner measured modulation transfer function of an IR scanner, (Astarita and Carlomagno, 2012).

pixel to measure correctly the temperature of the target object. This time is inversely proportional to the measured temperature so that, for low object temperatures, the maximum acquisition frequency is smaller than at higher ones.

### 3.2.4 Temperature and dynamic ranges

The temperature range which can usually be measured with an IR scanner spans approximately from −20 °C up to 1500 °C, but it can be further extended to higher values by adequately filtering the incoming radiation. Filtering is generally performed with filters which are grey in the used infrared band.

The dynamic range, or intensity resolution, is expressed in terms of the number of digital intensity levels the individual pixel signal is composed of. The latest generation of cameras typically provides 14 bits A/D conversion, which allows measurement of small temperature differences even in the presence of a relatively large temperature range in the viewed scene.

In any case, the temperature range is clearly limited at relatively small temperatures because of the extremely small radiative flux that impinges on the detector (see Figure 3.2). Besides, since the radiative flux is a nonlinear function of the temperature, when measuring large temperatures, the detector integration time must be significantly reduced or the incident radiation filtered, thus leading to a loss in the accuracy when simultaneously measuring lower temperatures.

## 3.3 IR scanner calibration

The output signal of an IR camera depends on the radiation energy that impinges on it and a calibration function is needed to convert the produced electric signal into the real viewed object (target) temperature. Most modern cameras are already calibrated; the user does not receive the raw output, but rather a 2D distribution map of temperatures.

Nevertheless, often a more accurate calibration, or a recalibration (e.g. in a different temperature range, smaller or larger) of the IR scanner is required. Here, the basic information necessary to calibrate an IR camera is reported.

To better understand the calibration procedure, a sketch is reported in Figure 3.6. A fraction of the radiation flux collected by the IR camera is emitted by the target. Indeed, two other contributions must be taken into account: one associated to the radiation emitted by the ambient that is reflected from the target and another to the atmosphere emission. Furthermore, it must be considered that the atmosphere itself represents a medium, thus constituting an attenuation for the radiation that reaches the scanner. Keeping in mind these considerations, if the emitting body is at a temperature $T_{obj}$, it will emit only a fraction $\epsilon_t$ of the radiation a black body would emit at the same temperature. If the transmissivity coefficient of the atmosphere is $\tau_r$ the radiation emitted by the object that reaches the IR camera detector will be $\tau_r \epsilon_t E_{b,obj}$.

Considering that, during the calibration the ambient temperature $T_{amb}$

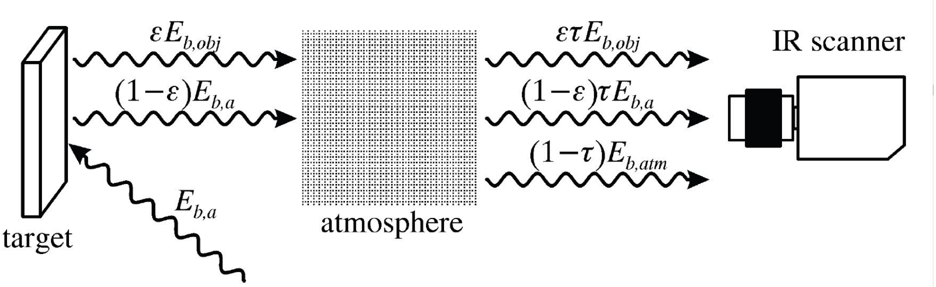

Figure 3.6: Sketch of the radiation detected by an IR camera, (Astarita and Carlomagno, 2012).

is kept at a constant value and that the extension of the ambient is much larger than that of the emitting body, it is reasonable to assume the ambient as a black body, thus the emitted radiation is $E_{b,amb}$. The target is assumed as opaque, the reflectivity coefficient can be evaluated as $1 - \epsilon_t$ and, taking also into account the absorption of the atmosphere, the radiation emitted by the surrounding ambient environment reflected by the target and collected by the IR camera detector is equal to $(1 - \epsilon_t)\tau_r E_{b,amb}$

Similarly, supposing that the atmosphere is at a constant temperature $T_{atm}$ and its emissivity is $(1 - \tau_r)$, the radiation collected by the IR scanner detector will be $(1 - \tau_r)E_{b,atm}$.

The total radiation collected by the IR camera detector results

$$E_t = \tau_r \epsilon_t E_{b,obj} + (1 - \epsilon_t)\tau_r E_{b,amb} + (1 - \tau_r)E_{b,atm} \tag{3.9}$$

The output detected signal of the IR detector $U_D$, which could be either a current $I$ or a voltage $V$ can be considered as linearly dependent on $E_t$:

$$U_D = \tau_r \epsilon_t U_{obj} + (1 - \epsilon_t)\tau_r U_{amb} + (1 - \tau_r)U_{atm} \tag{3.10}$$

The output signals $U_D, U_{obj}, U_{amb}, U_{atm}$ can be approximated by a function similar to Planck's law, being the IR bands quite narrow, so it results

$$U_D = \tau_r \epsilon_t \frac{R}{(e^{\frac{B}{T_{obj}}} - F)} + (1 - \epsilon_t)\tau_r \frac{R}{(e^{\frac{B}{T_{amb}}} - F)} + (1 - \tau_r)\frac{R}{(e^{\frac{B}{T_{atm}}} - F)} \tag{3.11}$$

The constants $R$ (voltage or electric current), $B$ (K) and $F$ (dimensionless) depend on the integration time and on the IR scanner properties. Equation 3.11 solved for $T_{obj}$, gives:

$$T_{obj} = \frac{B}{\ln\left(\dfrac{\epsilon_t \tau_r R}{U_D - (1-\epsilon_t)\tau_r U_{amb} - (1-\tau_r)U_{atm}} + F\right)} \tag{3.12}$$

Therefore, in order to calculate the object temperature, one needs to measure the ambient environment and atmospheric temperatures (which often coincide) with external thermometers and to evaluate the emissivity coefficient of the target, the transmissivity coefficient of the atmosphere and the three calibration constants. When performing measurements at relatively short distances, normally the atmospheric transmissivity coefficient can be practically put equal to 1, therefore, the terms associated with atmospheric absorption and emission may be neglected. This hypothesis is assumed in the following. If a semi-transparent window (or a mirror) is placed in the optical path, other terms, similar to that relative to the atmospheric absorption, should be included in the previous equations and both the optical characteristics of the window (mirror) and its temperature should be known.

For the determination of the calibration constants a black body is used as a reference object for the calibration so that the emissivity is equal to 1 and also the spurious reflections from the surrounding ambient environment can be neglected. Putting the black body relatively close to the IR camera, Equation 3.12 reduces to

$$T_{obj} = \frac{B}{\ln\left(\dfrac{R}{U_D} + F\right)} \tag{3.13}$$

By changing the black body temperature in the range of interest, it is possible to record the output signal from the IR scanner and then the calibration constants can be found by making a non-linear best fit of the independent measurement points.

In particular, by indicating with $T_b$ the black body temperature, measured with a high-accuracy thermometer, the calibration constants are evaluated by varying $R$, $B$ and $F$ in order to minimize, with a standard optimization algorithm, the functional:

$$\sum_{i=1}^{n}(T_b^i - T_{obj}^i)^2 \tag{3.14}$$

The temperature calibration range should be chosen larger than the expected real experimental one.

## 3.4 Heated thin foil heat flux sensor

Infrared thermography is predominantly applied in thermo-fluid dynamics for determining the convective heat flux $\dot{q}_c$ (energy per unit surface and per unit time, $\mathrm{W\,m^{-2}}$), and/or the convective heat transfer coefficient $h$ (heat flux per unit temperature difference, $\mathrm{W\,m^{-2}\,K^{-1}}$), between a solid surface and a fluid flowing on it. By applying a suitable thermo-physical model and the energy conservation equation to the sensor, it is usually possible to find a relationship between the measured temperature and the convective heat transfer coefficient, between the sensor and the moving fluid. It has to be point out that the convective heat flux is a vector quantity. However, only its component normal to the exchanging surface will be considered. In the case of the experiments reported in this thesis, the heated thin foil heat flux sensor is used.

IR camera represents the temperature transducer, while the sensor is made of a thermally thin foil with a well-known thermal behaviour, whose surface temperature has to be measured by means of the IR camera. Frequently, the thermo-physical properties of the slab vary only slightly with the temperature, so that it is often possible to assume the heat flux sensor as ideal (i.e. independent of its thermodynamic state, that is, its temperature). The thermally thin foil can be either metallic (i.e. stainless steel or constantan typically tens of micrometres thick) or a printed board circuit, heated by a known heat flux, generally provided via Joule effect. The foil is exposed to the incoming fluid on one side, whilst the opposite side is generally thermally insulated or imaged by IR camera, as in the case of the experiments reported in the present thesis. The temperature measurement of the foil side opposite to the impinged surface is possible being the thermally thin

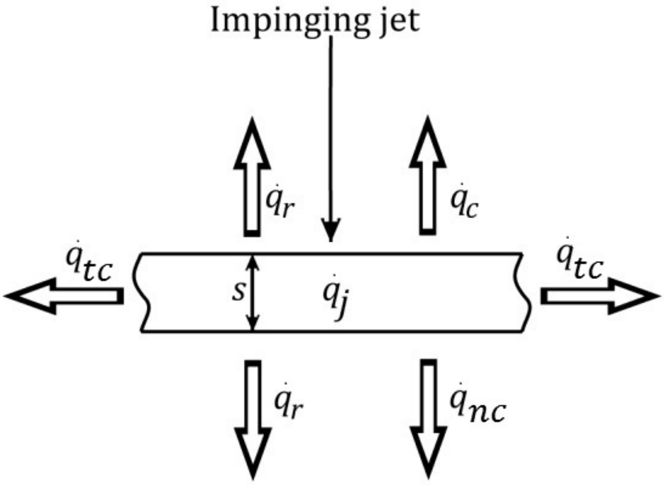

Figure 3.7: Energy balance within the slab, (adapted from Astarita and Carlomagno, 2012).

condition satisfied. This implies that the Biot number, $Bi = hs/k_f$ where $h$ is the convective heat transfer coefficient, $s$ is the foil thickness and $k_f$ is the thermal conductivity of the foil, is smaller than 1. Furthermore, the foil allows to follow unsteady thermal processes whenever the Fourier number $Fo = \alpha t/s^2$, where $\alpha$ is the thermal diffusivity of the foil, $t$ is a characteristic time of the flow, is greater than 1. The emissivity of the imaged side is artificially increased by coating it with a thin layer of thermally black paint, with emissivity coefficient $\varepsilon$, in order to increase the signal acquired by the thermal detector.

By applying the steady state energy balance to the foil represented in Figure 3.7, it results:

$$\dot{q}_j = \dot{q}_r + \dot{q}_{nc} + \dot{q}_{tc} + \dot{q}_c \tag{3.15}$$

the terms in Equation 3.15 represent:

- $\dot{q}_j$: heat flux input provided by Joule effect with a stabilized power supply. The voltage $V_f$ and the electric current $I_f$ imposed to the foil (which represents an electric resistance) of surface area $A_f$ are measured giving: $\dot{q}_j = V_f I_f / A_f$;

- $\dot{q}_r$: radiative heat flux. This contribution is estimated by using the Stefan-Boltzmann's law: $\dot{q}_r = \sigma\varepsilon(T_w^4 - T_{amb}^4)$, where $\sigma$ is the Stefan-Boltzmann's constant, $T_w$ is the foil temperature and $T_{amb}$ is the ambient temperature. This term is made of two contributions: one towards the impinging flow, which is negligible according to the small value of the emissivity of the plate in that direction and the other is the radiation towards the ambient;

- $\dot{q}_{nc}$: natural convection heat flux. This loss contribution can be estimated using well-known empirical correlations available in literature (see McAdams, 1954; Welty et al., 2009) or performing ad hoc experiments;

- $\dot{q}_{tc}$: tangential conduction heat flux. In case of isotropic material, it can be estimated by means of Fourier's law: $\dot{q}_{tc} = -k_f s \nabla^2 T_w$, with $\nabla^2$ the two-dimensional Laplacian operator evaluated in the heat flux sensor plane (Carlomagno and Cardone, 2010; Astarita and Carlomagno, 2012);

- $\dot{q}_c$: convective heat flux. It can be expressed in terms of Newton's law: $\dot{q}_c = h(T_w - T_{aw})$, being $T_{aw}$ the adiabatic wall temperature.

Solving Equation 3.15 for $h$, the following expression is obtained:

$$h = \frac{\dot{q}_j - \dot{q}_r - \dot{q}_{nc} - \dot{q}_{tc}}{T_w - T_{aw}} \tag{3.16}$$

The heat losses $\dot{q}_r, \dot{q}_{nc}, \dot{q}_{tc}$ are to be considered as correction terms and, in order to obtain accurate data, they should be a small fraction of the total Joule heating; otherwise, an error in their evaluation could produce a significant error in the measured $h$. Furthermore, $T_{aw}$ is measured without heating the foil in normal on-going testing flow conditions. The $T_w$ is representative of the wall temperature when the heat flux by Joule effect is provided to the plate and the jet is impinging onto it.

# Chapter 4

# Flow field of a chevron synthetic jet [1]

In this chapter, the flow field generated by a synthetic jet device with a six-chevron nozzle exit is studied and compared to the baseline case represented by a circular synthetic jet. For both configurations, the devices are operated at the same input electric power, thus leading to Reynolds and Strouhal numbers equal to 5600 and 0.115 for the circular exit and 6000 and 0.106 for the chevron exit. Phase-locked Stereo-PIV measurements are used to reconstruct the three-dimensional coherent vortex structures. Time-averaged and phase-averaged measurements are analysed and discussed.

## 4.1 Experimental procedure

### 4.1.1 Experimental setup

Experiments are carried out on two synthetic jet devices with a circular and a chevron nozzle exit. A schematic of the system is displayed in Figure 4.1. In order to generate the synthetic jet, the contoured nozzle is coupled with a loudspeaker (Audiola SBL 20N BL) of diameter equal to 100 mm (Figure 4.1a). The contoured nozzle and the chevron cap used in this thesis are

---

[1] This chapter has been adapted from the article published in Experimental Thermal and Fluid Science, (Crispo et al., 2017).

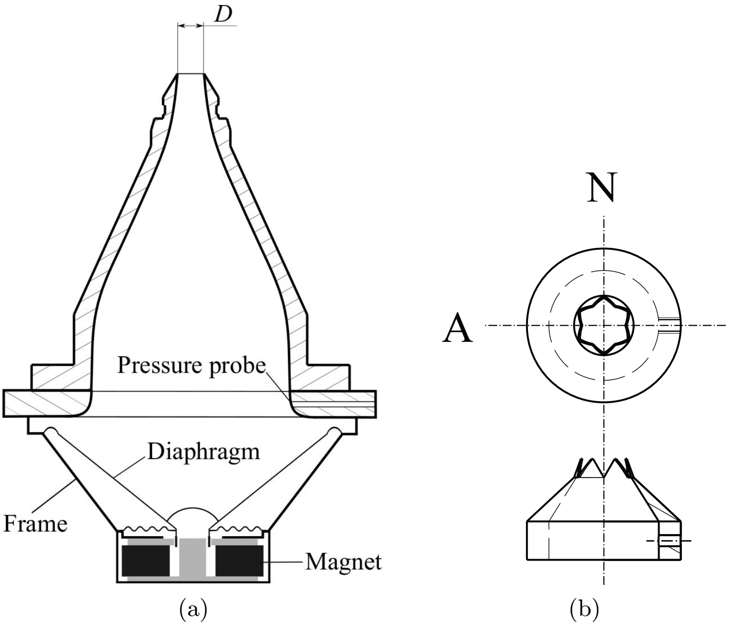

Figure 4.1: Synthetic jet device: sketch of the (a) jet device and (b) chevron cap.

described in detail in Violato and Scarano (2011) and Violato et al. (2012). The round nozzle has an exit diameter $D$ of 10 mm, it is 125 mm long and it has a contraction ratio of 56:1. Following the work of Schram (2003), the nozzle contraction shape is a symmetric $7^{\text{th}}$ order polynomial profile. The chosen profile yields an uniform laminar flow at the exit. The chevron synthetic jet is realised by applying a chevron exit cap (Figure 4.1b) on top of the round nozzle. The chevron exit has six chevron elements 4.5 mm long and inclined towards the jet axis with an angle of 18.2°, thus resulting in a penetration depth of 1.48 mm.

The resonance frequency of the system in both configurations is experimentally determined by measuring the loudspeaker impedance, as done by Greco et al. (2013). The system is characterised by two resonance frequencies equal to about 80 Hz and 300 Hz. The loudspeaker is driven by a sinusoidal input signal with a frequency of 96 Hz by a Diligent Inc. Analog Discovery analog signal generator coupled with an amplifier. At this working frequency the impedance of the two synthetic jet configurations differs of less than 1.5 %. The system is operated with electric power equal to 5.2 W. Under these operating conditions, the Reynolds number (Equation 1.1) is equal to 5600 and 6000 and the Strouhal number (Equation 1.2) is equal to 0.115 and 0.106 for the circular and the chevron configurations, respectively. They are estimated by measuring the axial velocity component along the jet centreline at 0.6 $D$ from the nozzle exit, which is the closest point to the exit plane of the round nozzle in the FOV. The origin of the reference frame is fixed at the centre of the round nozzle exit section. The $x-$axis is aligned with the jet centreline and the $y-$ and $z-$axes lie in the plane perpendicular to the $x-$direction, forming a clockwise reference frame. A sketch of the adopted reference frame is reported in Figure 4.2.

### 4.1.2 PIV measurement details

Stereo-PIV technique is used to measure the instantaneous two-dimensional three-component velocity field. Particle images are acquired in the $x - y$ plane passing through the jet axis. In presence of the chevron exit, $x - y$ planes including both the apex (A in Figure 4.1b) and notch (N in Figure 4.1b) are investigated.

Furthermore, phase-locked scanning Stereo-PIV measurements are carried out in order to reconstruct the three-dimensional coherent vortex structures. The 3D reconstruction is carried out recording particle images in the crosswise $y - z$ plane as follows: for a given phase the position of the vortex core cross-section is detected by looking at the streamwise measurements. Then, the synthetic jet device is placed with the $x-$axis perpendicular to the laser sheet, on a slide with micrometre accuracy and the flow field is scanned along the $x-$ direction with 33 equidistant planes across the vortex core (Figure 4.2b). The distance between two subsequent planes is set to $\Delta x = 0.5\,\text{mm}$. For each plane 500 double frame particle images are acquired. Three phases are investigated corresponding to a vortex ring position at about $x/D = 1.75$, 3 and 4.5. These phases represent a near, middle and far location of the vortex ring in the investigated field of view of the streamwise measurements.

Oil droplets with a diameter of approximately 1 µm are used to seed the

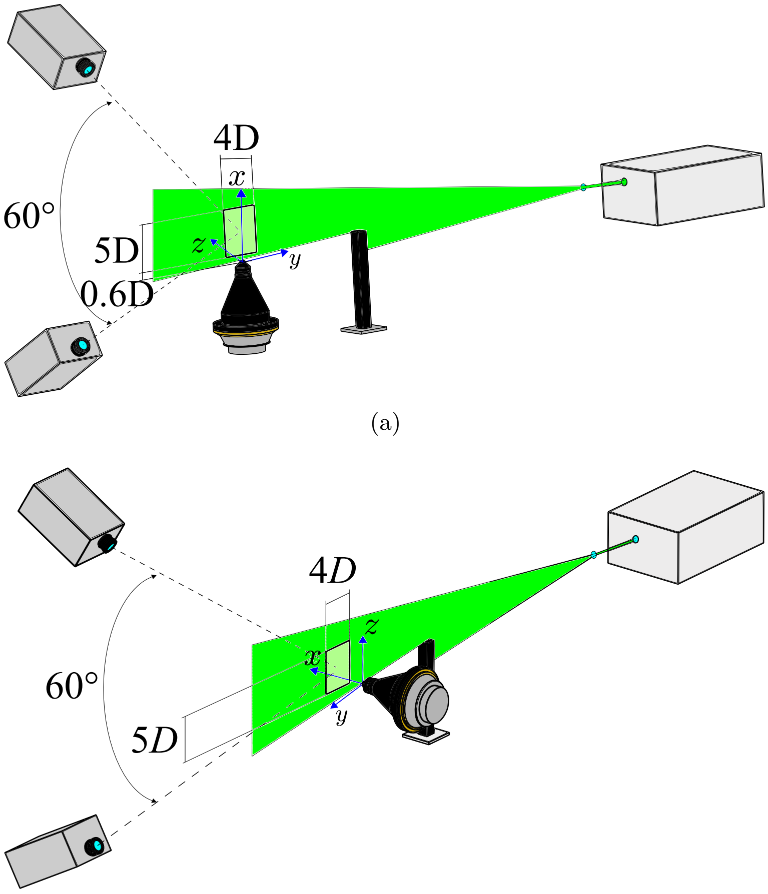

(a)

(b)

Figure 4.2: Sketch of the experimental setup: Stereo-PIV system and measurement domain for (a) streamwise and (b) crosswise measurement planes.

flow. Illumination is provided by the Quantel Evergreen laser that is a double pulsed Nd:YAG laser (532 nm, 200 mJ per pulse, <10 ns pulse duration). The time separation between the two laser pulses is set to $\Delta t = 8\,\mu\text{s}$ and to $\Delta t = 6\,\mu\text{s}$ for the streamwise and the crosswise plane, respectively. The laser sheet thickness is approximately 1 mm. Particle images are recorded by two

Andor Zyla sCMOS cameras (2160 px × 2560 px, 16 bit, 6 µm px$^{-1}$ equipped with Scheimpflug adapters and Tokina 100 mm focal length objectives set at numerical aperture $f_{\#} = 16$. The resulting digital resolution is 50 px mm$^{-1}$. The measurement domain in the $x - y$ plane (Figure 4.2a) ranges between $0.6 < x/D < 5.6$ and $-2 < y/D < 2$, while in the crosswise $y - z$ plane (Figure 4.2b) ranges between $-2 < y/D < 2$ and $-2.8 < z/D < 2.2$. The acquisition system is synchronized with the synthetic jet in order to perform phase-locked measurements. The synchronization is realised by using a Digilent Inc. Analog Discovery. The input signal to the loudspeaker is used also as trigger for the acquisition system. The acquisition is performed at the frequency $f_{acq}$ estimated following Greco et al. (2013):

$$f_{acq} = \frac{f}{\frac{1}{N_{div}} + n_p} \tag{4.1}$$

The phenomenon with frequency $f$ is sampled every $n_p$ periods of membrane oscillation with a phase shift of $360°/N_{div}$. The phenomenon is sampled with a 12° phase separation. In order to obtain reliable turbulent statistics, 15,000 double frame particles images (500 snapshots for each phase) are recorded.

A multi-pass algorithm with windows deformation and Blackman weighting windows (Astarita and Cardone, 2005; Astarita, 2006, 2007, 2008) is used to compute the velocity fields. The final interrogation window size is 32 px × 32 px with an overlap of 75 %, thus resulting in a vector pitch of 0.16 mm (approximately 62 vectors per $D$) for the streamwise measurements. Differently, for the crosswise measurements the final interrogation window size is 24 px × 24 px with an overlap of 75 % and vector pitch of 0.12 mm (approximately 83 vectors per $D$). A normalised median validation criterion (Westerweel and Scarano, 2005) is applied to remove spuriously detected vectors. The uncertainty in displacement, related to the peak localisation, is the main contribution to velocity uncertainty. For the given particle size (approximately 3 px), image noise and particle displacement, the random error is found to be approximately 2 % of the maximum velocity in the jet core. The details of the experimental set up are summarized in Table 4.1.

Table 4.1: Details of the experimental setup for free flow field.

| | |
|---|---|
| Flow conditions | $Re = 5600$, $St = 0.115$ (circular)<br>$Re = 6000$, $St = 0.106$ (chevron) |
| Seeding material | olive oil particles - 1 µm diameter |
| Illumination | Quantel Evergreen Nd:YAG laser (532 nm, 200 mJ per pulse, <10 ns pulse duration) |
| Recording device | 2 Andor Zyla sCMOS cameras (2160 px × 2560 px, 16 bit, 6 µm px$^{-1}$) |
| Recording method | double frame - single exposure |
| Optical arrangement | Tokina 100 mm focal length objectives, $f_{\#} = 16$ with Scheimpflug adapters |
| Field of view | $5D \times 4D$ (streamwise)<br>$4D \times 5D$, $1.6D$ scanned, $0.05D$ spatial step (crosswise) |
| Pulse separation | 8 µs (streamwise), 6 µs(crosswise) |
| Recorded images | 500 snapshots/phase (streamwise)<br>500 snapshots/plane (crosswise) |
| Digital resolution | 50 px mm$^{-1}$ |
| Interrogation window size | 32 px × 32 px, overlap 75 % (streamwise)<br>24 px × 24 px, overlap 75 % (crosswise) |

### 4.1.3 Data reduction: triple decomposition

The velocity triple decomposition scheme, proposed by Hussain and Reynolds (1970), is used for the data analysis:

$$u_i(\underline{x}, t) = U_i(\underline{x}) + \tilde{u}_i(\underline{x}, t) + u_i'(\underline{x}, t) \tag{4.2}$$

being $u_i$ the i-th instantaneous velocity component ($u_1 = u, u_2 = v, u_3 = w$), $U_i$ the time-averaged velocity component, $\tilde{u}_i$ the phase-correlated velocity component and $u_i'$ the turbulent fluctuations. They are defined as follows:

$$U_i(\underline{x}) = \lim_{t \to \infty} \frac{1}{t} \int_0^t u_i(\underline{x}, g) dg \tag{4.3}$$

$$< u_i(\underline{x}, t) >= \lim_{N \to \infty} \frac{1}{N} \sum_{m=0}^{N} u_i(\underline{x}, t + m\tau) \tag{4.4}$$

$$\tilde{u}_i(\underline{x}, t) =< u_i(\underline{x}, t) > -U_i(\underline{x}) \tag{4.5}$$

$$u_i'(\underline{x}, t) = u_i(\underline{x}, t) - < u_i(\underline{x}, t) > \tag{4.6}$$

where $< u_i(\underline{x}, t) >$ is the phase-averaged velocity component, $N$ is the number of the instantaneous fields at the same phase, $m$ is an integer and $\tau$ is the time period of the wave produced by the loudspeaker.

The time-averaged turbulent kinetic energy $TKE$ and the phase-averaged turbulent kinetic energy $< TKE >$ can be computed as

$$TKE = \sum_i \overline{u_i' u_i'}/2 \tag{4.7}$$

$$< TKE >= \sum_i < u_i' u_i' > /2 \tag{4.8}$$

where $\overline{u_i' u_i'}$ and $< u_i' u_i' >$ are the time-averaged and phase-averaged Reynolds stresses, respectively.

## 4.2 Results

In this section, the mean and statistical flow fields generated by both the circular and chevron synthetic jets are discussed and compared. Since it has been experimentally proved that the flow fields in the $x - y$ plane are symmetric with respect to the jet centreline, data are further averaged using the two middle-planes and then mirrored for easy interpretation. As a consequence, measurements noise is further reduced.

In this section, the starting phase $\phi = 0°$ is considered as the phase corresponding to the first positive axial-velocity value measured along the jet axis at the most upstream location.

### 4.2.1 Time-averaged velocity field

In Figure 4.3, the streamwise evolution of the dimensionless time-averaged axial velocity component along the jet centreline ($U_c$) is shown. The figure shows different behaviours of the two devices. More in detail, for the chevron synthetic jet $U_c$ increases faster than the circular jet and it attains its maximum $0.4D$ more downstream ($x/D = 2.3$). In the decay region, the jet with the chevron exit exhibits higher $U_c$. Furthermore, for the circular synthetic jet $U_c$ decreases proportional to $x^{-1}$ in agreement with the findings of Cater and Soria (2002) while the chevron one decreases with $x^{-0.55}$.

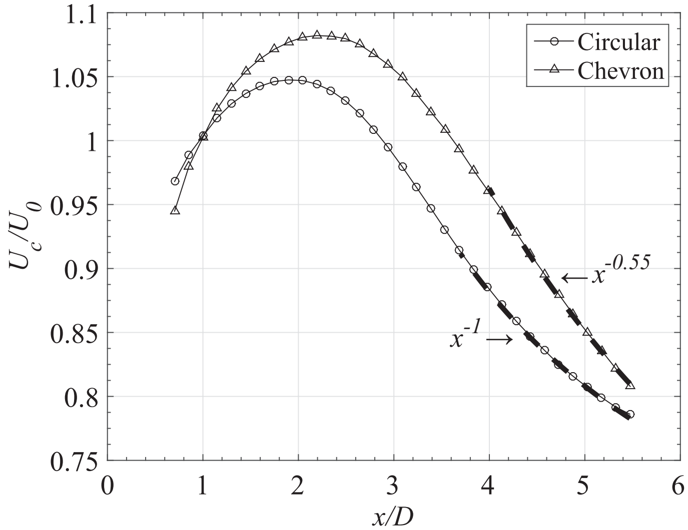

Figure 4.3: Time-averaged axial velocity component along the jet centreline ($U_c$) for the circular and the chevron synthetic jets.

The mean flow field topology is further discussed by looking at the evolution of the time-averaged axial velocity ($U$ profiles in the $y-$ direction, Figure 4.4). At $x/D = 0.6$ the circular device shows, in Figure 4.4a a region of constant $U$ across the jet centreline ($0.3 < y/D < 0.3$). Furthermore, it shows a change of slope at $y/D = \pm 0.65$ because of the long permanence of the vortex ring near the nozzle exit during the ejection phase, as it will be shown in the following Section 4.2.2. Moving away from the centreline, a region of negative $U$ is measured. It is due to the suction phase which affects the flow field up to $x/D = 2$. Moving downstream, the $U$ profile shows a bell-shaped distribution. For $x/D \geq 2$, the maximum of $U$ along the jet axis decreases (see $U_c$ in Figure 4.3) and the jet spreads because of the radial momentum diffusion (similar to continuous turbulent jets as reported by Abramovich et al., 1984).

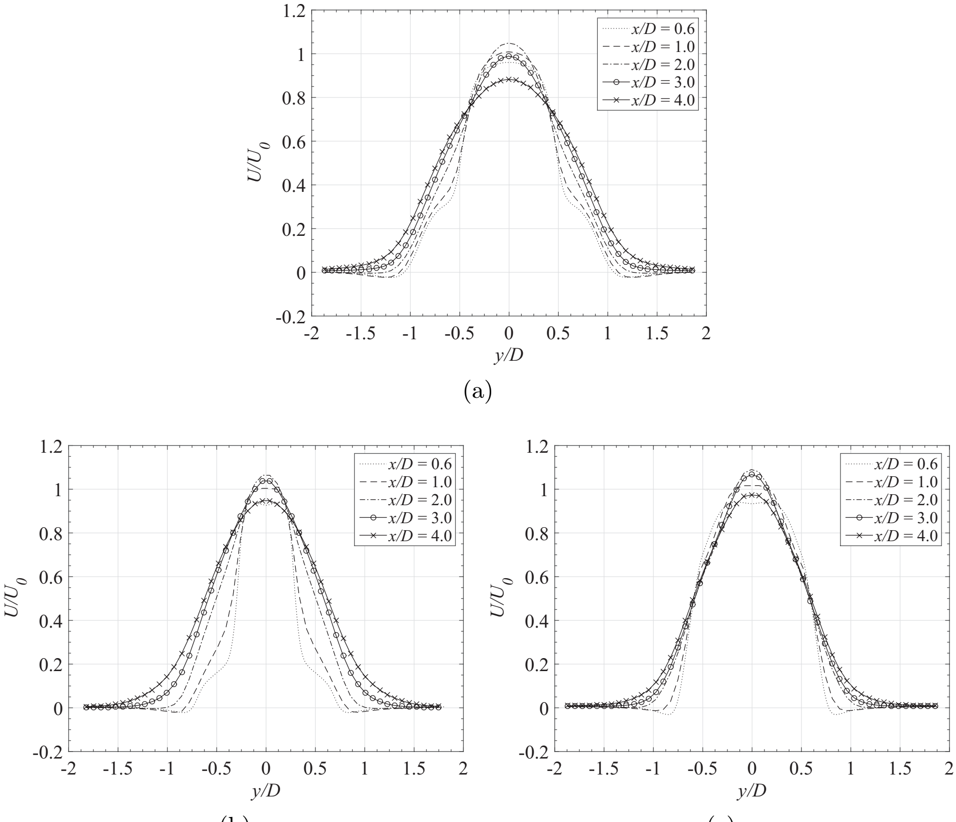

(a)

(b) (c)

Figure 4.4: Spatial distribution of $U$ in the $y-$direction at $x/D = 0.6$, 1.00, 2.00, 3.00, 4.00. (a) Circular synthetic jet, (b) apex and (c) notch of the chevron synthetic jet.

The chevron exit geometry acts as an additional converging nozzle in the apex plane. As a consequence, at $x/D = 0.6$ (see Figure 4.4b), the width of the $U$ profile is smaller than in presence of the circular exit. Moreover, two small peaks at $y/D = \pm 0.2$ are measured. At this streamwise position, regions with negative $U$ are present at $-1.29 < y/D < 0.74$ and $0.74 < y/D < 1.29$, and similarly to the circular configuration, the velocity decays to zero changing its slope. Moving downstream ($x/D \geq 2$), the two small peaks and the negative $U$ are not detected anymore. From $x/D \geq 2$, $U$ shows the same bell-shaped distribution as for the circular exit.

In the notch plane, the jet is issued from a larger exit area with same radius of the circular exit. The $U$ profile at $x/D = 0.6$ is wider than that of the circular configuration. Similar to the apex plane, a region characterised by negative $U$ is present and two small peaks can be observed at $y/D = \pm 0.2$. In this case, the lateral slope does not change, Figure 4.4c and this can be addressed to the average lateral transport of high momentum fluid at the notch (as shown for notched nozzles by Pannu and Johannesen, 1976).

Figure 4.5 shows the turbulent kinetic energy behaviour along the jet centreline, $TKE_c$. The chevron jet lowers the turbulence intensity along the jet centreline, in agreement with Violato and Scarano (2011). The trend of the $TKE_c$ is similar for both configurations, showing a reduction followed by an increase. The increase of the $TKE_c$ values for the circular synthetic jet is much stronger than that for the chevron one reaching approximately twice the intensity at $x/D = 5.5$.

Contours of $TKE$ in the $x - y$ plane are reported in Figure 4.6. In Figure 4.6a, at $x/D = 0.6$, the circular exit shows two local maxima at $y/D = \pm 0.5$ (inner high turbulent region) and $y/D = \pm 0.85$ (outer high turbulent region). The peak of $TKE$ in the outer turbulent region is caused by the turbulence production in the vortex ring core, while in the inner turbulent region is due to the shear layer between the trailing jet and the external quiescent ambient. At more downstream locations, the inner and outer turbulent regions merge because of the spreading of both the high turbulent region and of the shear layer. For both configurations, a low intensity $TKE$ region is measured across the centreline (i.e., inner region) in the near field corresponding to the jet width reduction. Downstream of this low turbulence intensity region, the $TKE$ increases and the high turbulent intensity area spreads because of the growth of the turbulent vortex ring (Maxworthy, 1977).

Focusing on the chevron synthetic jet, the $TKE$ maps, in Figure 4.6b for the apex plane and in Figure 4.6c for the notch plane, show that, near

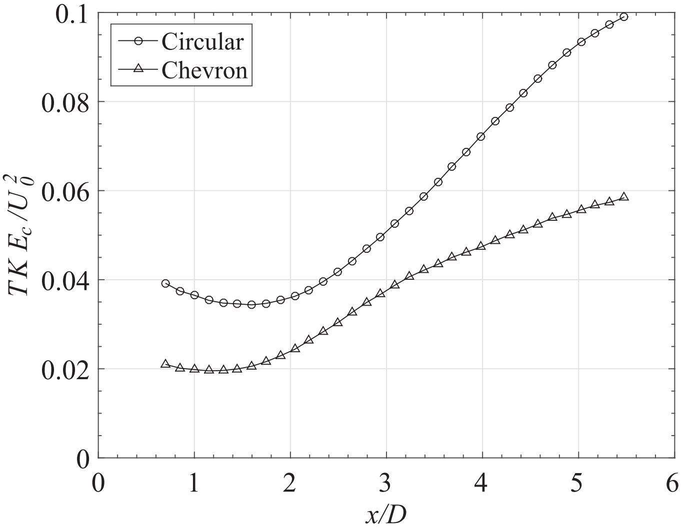

Figure 4.5: $TKE$ along the jet centreline for circular and chevron synthetic jets.

the nozzle exit, the high turbulent region is respectively tighter and thicker than the one of the circular jet. In the apex plane, the outer turbulent region is barely visible and, the high turbulence intensity is measured in the shear layer. Differently in the notch plane, the high $TKE$ area is thicker because of the presence of both the shear layer and the vortex ring. At more downstream locations, for both planes the high turbulent region spreads and the $TKE$ intensity decreases. On the other hand, a small increase of $TKE$ is measured at the end of the FOV. For $1.5 < x/D < 4.5$, the turbulence intensity decreases and the turbulence generated by the shear layer prevails over the one related to the vortex ring. At more downstream location this trend is reversed by the prevailing vortex ring effect. Comparing the $TKE$ intensity levels for the two devices, the chevron nozzle shows larger intensity in the near field ($x/D < 1.5$), while lower intensity at more downstream locations. These findings are in agreement with previous literature on continuous chevron jets (Doty et al., 2007; Bridges and Wernet, 2002). This calming effect, as named by Zaman et al. (2011) for continuous jets, may be a consequence of the streamwise vortices, which reduce the turbulence in the shear layer. These aspects will be clearly analysed in the following Section 4.2.2.

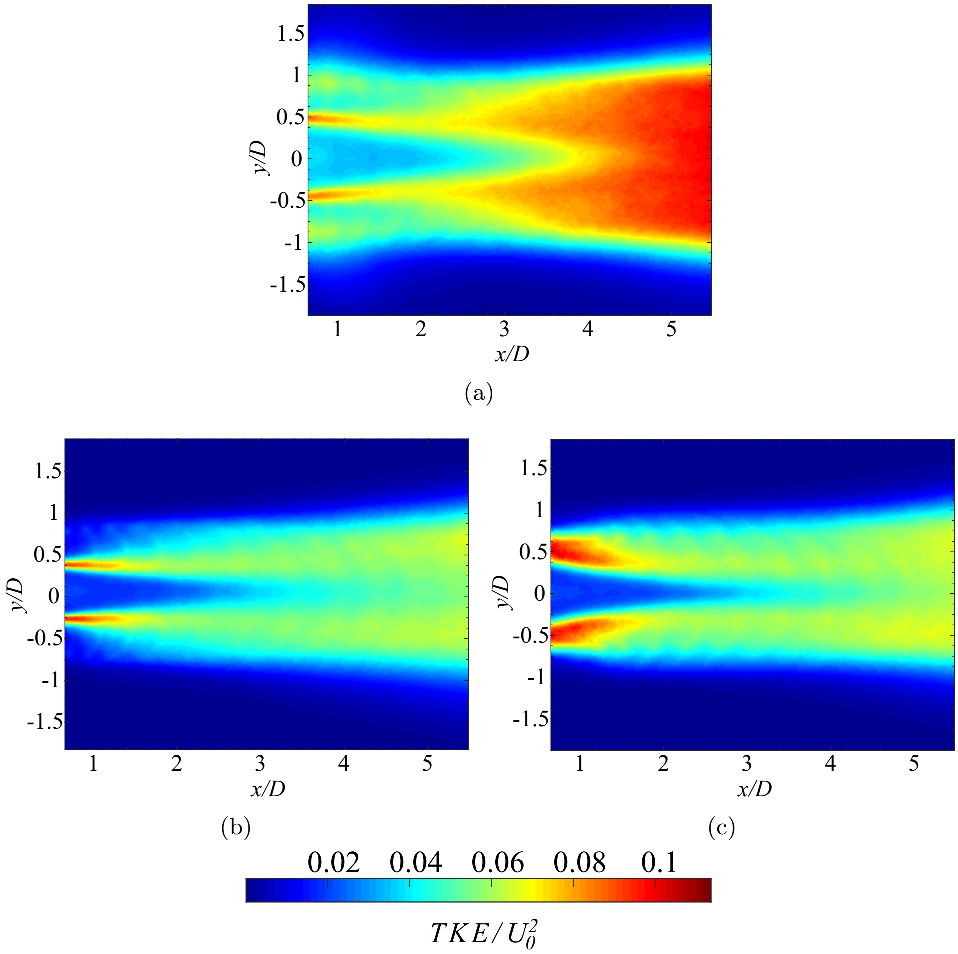

(a)

(b)

(c)

Figure 4.6: Time-averaged TKE maps for (a) circular, (b) apex and (c) notch planes.

### 4.2.2 Phase-averaged velocity field

The phase evolution of the two synthetic jets is discussed by looking at both the phase-averaged mean velocity and $< TKE >$ fields. The phase evolution of the circular synthetic jet is reported in the first column of Figure 4.7 where the phase-locked axial $< u >$ and the radial $< v >$ velocity components are reported in the top and bottom part of each subplot.

The vortex ring, visualised through the projection of the velocity vectors in the $x - y$ plane, is fully visible in the measurement area at $\phi = 60°$. In the jet core, i.e. the area embedded between the vortex ring, the $< u >$ is approximately constant in the $y$-direction up to $0.5\,D$ from the jet axis. At $\phi = 120°$, the region of high $< u >$ is still embedded within the vortex ring but its intensity decreases. Moreover, in the wake of the vortex ring, the trailing jet is formed. The vortex ring reduces its intensity convecting downstream as suggested by the maps of the axial and radial velocity components. During the last phase of ejection, the trailing jet is weakly visible and the spanwise velocity profile within the trailing jet is bell shaped.

The phase-locked evolution of the chevron synthetic jet is reported in the second and third column of Figure 4.7 for the apex and notch plane, respectively. Starting from $\phi = 60°$, the phase at which the vortex ring is fully visible, it is evident that in the apex plane at $x/D = 0.6$ the spanwise extension of the region where $< u > /U_0 \geq 0.75$, is approximately 30 % narrower than for the circular configuration. On the other hand, along the notch plane the spanwise extension of this region is approximately 20 % larger than for the circular configuration. At this phase, at approximately $0.2 < y/D < 0.4$, close to the jet core, the radial velocity component shows a motion towards the jet axis in the apex plane and an opposite motion, away from the jet axis, in the notch plane. These flow components are induced by streamwise vortices generated at the root of the chevron teeth (as discussed in the next section). Increasing $\phi$, the strength of both the inward and outward motions reduces because of the weaker streamwise vortices. At $\phi = 120°$, small differences in the $< v >$ component are measured at the trailing jet location (see circle in Figure 4.7). Both axial and radial velocity maps suggest a wider shear layer characterised by outflow along the notch plane and a tighter shear layer characterised by inflow along apex plane. At

$\phi = 168°$, no appreciable difference between the two planes of the chevron jet is detected.

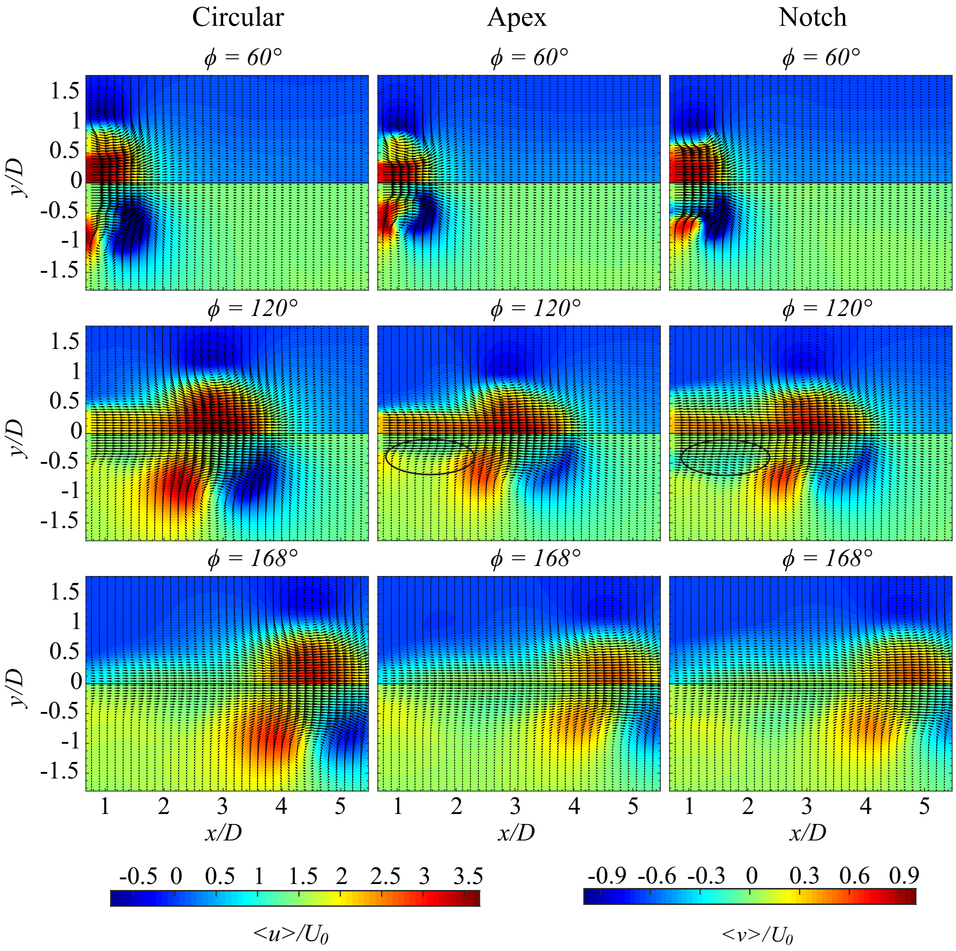

Figure 4.7: Phase-averaged axial (top) and radial (bottom) velocity components maps for circular (first column) and chevron (apex plane in the second column and notch plane in the third column) synthetic jets.

The statistical flow properties are discussed by looking at $< TKE >$, illustrated in Figure 4.8. For the circular configuration, at $\phi = 60°$ local high turbulence intensity regions are detected in the vortex ring core and across the shear layer between the jet core and the vortex ring. As the vortex ring moves downstream ($\phi = 120°$), the $< TKE >$ in the vortex core increases and the area of high turbulence intensity becomes wider. The trailing jet is characterised by a high $< TKE >$ intensity region across the shear layer near the nozzle exit. Further downstream, at $\phi = 168°$, the $< TKE >$ across the trailing jet decreases its intensity while the region of high $< TKE >$ inside the vortex ring core spreads towards the jet axis.

The chevron synthetic jet shows a completely different phase evolution of the $< TKE >$. At $\phi = 60°$, along the apex plane local maxima of $< TKE >$ are observed in the vortex ring core and in the region between the jet core and the vortex ring. Oppositely, in the notch plane the two regions cannot be distinguished. At $\phi = 120°$, the $< TKE >$ intensity is approximately the same in both the core of the vortex ring and along the trailing jet. Differently, the circular configuration shows high turbulence fluctuations intensity in the vortex core region. This uniformity in the intensity of the $< TKE >$ is due to the redistribution of the turbulent kinetic energy between the two large structures present in the chevron configuration: streamwise vortices and non-circular vortex ring (as it will be shown in the next section). When the vortex convects downstream, at $\phi = 168°$, the differences between the apex and the notch planes disappear. Furthermore, at this phase, the chevron synthetic jet shows only one region with relatively high $< TKE >$ near the vortex ring core whose values are definitely lower than those present in the circular configuration.

The difference in the spatial and time evolution of the $< TKE >$ may be explained by looking at the formation and evolution of the coherent structures, which are reported in the next section. The circular synthetic jet is characterised by a larger turbulence intensity in the vortex ring core than along the shear layer of the trailing jet. These regions may be caused the by the roll-up of the vortex ring and by the shear layer generated at the interface between the jet column and the surrounding environment. At more downstream locations (subsequent $\phi$), the vortex ring dissipates generating a wider and higher turbulence intensity area (Maxworthy, 1977). Differently, the chevron synthetic jet is characterised by both streamwise and azimuthal vortices, as reported in the next section. The formation of the streamwise

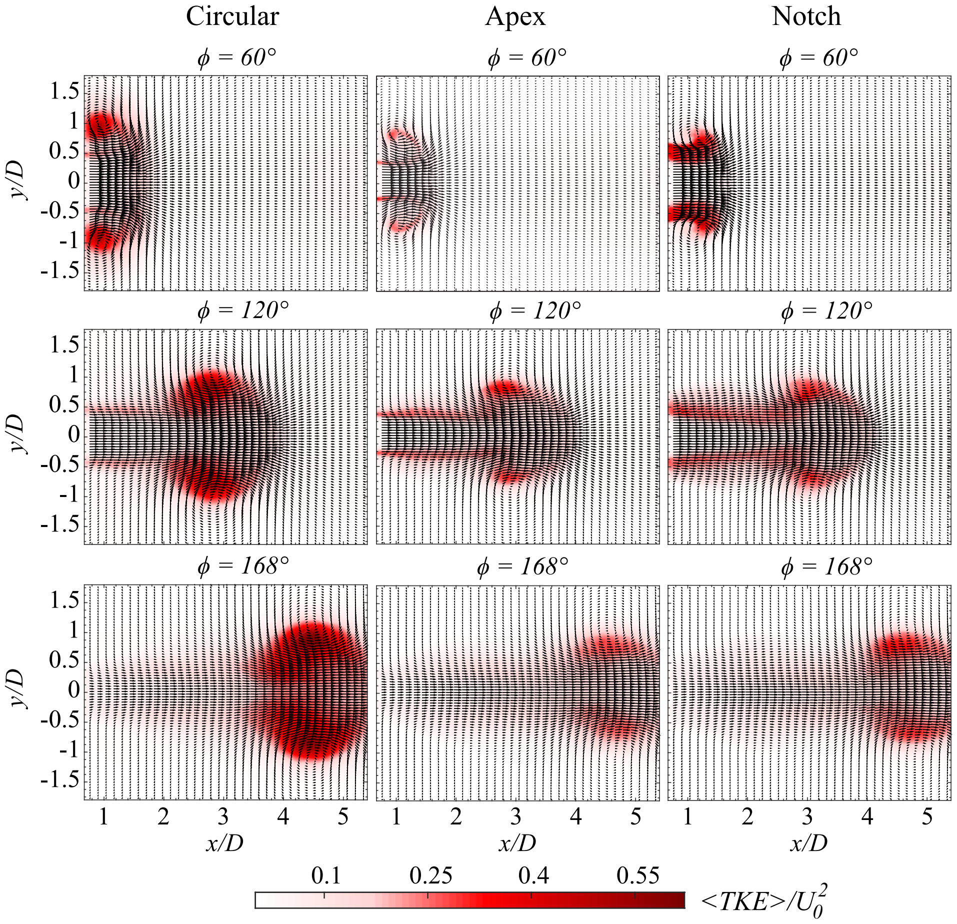

Figure 4.8: Phase-averaged turbulent kinetic energy maps for circular (first column) and chevron (apex plane in the second column and notch plane in the last column) synthetic jets.

structures at the notches may explain the larger intensity of the $< TKE >$ at this location. Differently from the circular case, at more downstream locations, the $< TKE >$ is less intense in the vortex ring core but slightly more intense along the trailing jet. This may be ascribed to the vorticity redistribution. As a matter of fact, the vorticity dissipates both along the trailing jet and the vortex ring core, resulting in the measured $< TKE >$ pattern. The streamwise vorticity appears to reduce the turbulence intensity of the vortex ring compared to the circular case. A similar effect was found by Zaman et al. (2011) for continuous chevron jet.

Figure 4.9 reports the $x - y$ location per phase of the vortex ring core generated in presence of the chevron nozzle exit along the apex and notch planes. The vortex-ring core location is detected as the location of maximum intensity of out-of-plane vorticity ($\omega_z$). In the figure, data for $\phi = 24°$ are not reported because the vortex ring is not fully present in the FOV. During the phase-evolution ($48° \leq \phi \leq 168°$) the position of vortex ring core in the apex plane is always farther from the jet axis and closer to the nozzle exit with respect to the notch plane. The distance reduces at the following phases and at $\phi = 168°$ both the $x$ and $y$ positions merge. This is due to the fact that the vortex ring of the chevron synthetic jet initially assumes a non-circular shape while, at a more downstream location, it tends to a classic circular vortex ring shape, as it will be shown in the next section.

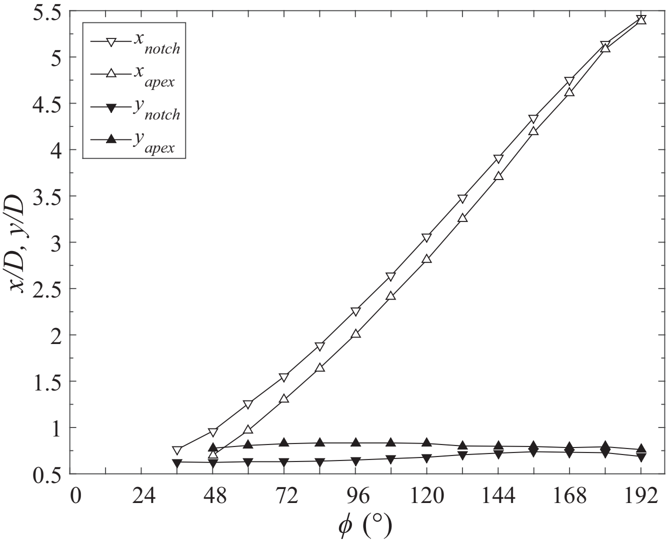

Figure 4.9: Streamwise ($x$) and radial ($y$) location of the vortex ring core along the apex and notch planes.

### 4.2.3 Flow field reconstruction

In order to study the three-dimensional flow organisation for the two investigated configurations, the flow field is reconstructed by means of scanning Stereo-PIV measurements for three phases corresponding to $\phi = 84°, 120°$ and $168°$.

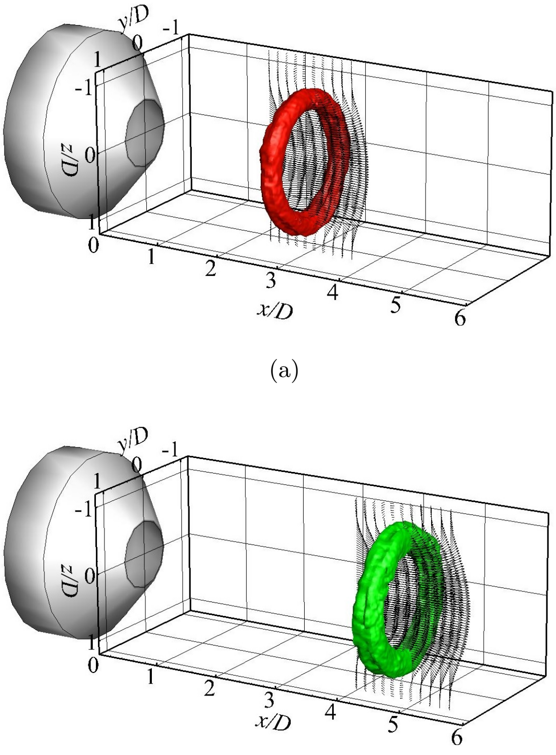

(a)

(b)

Figure 4.10: Three-dimensional reconstruction of the flow field at phase (a) 120° and (b) 168° for circular synthetic jet. Red iso-surface with $QD^2/U_0^2 = 25$ and green iso-surface with $QD^2/U_0^2 = 15$.

The circular synthetic jet is characterised by a vortex ring, reported in Figure 4.10, that becomes weaker moving downstream as already discussed in the previous section and reported in the literature (Smith and Glezer, 1998; Cater and Soria, 2002). As a matter of fact, by using the $Q$ criterion (Jeong and Hussain, 1995) to visualise the vortices, two different iso-surface levels equal to 25 and 15 are used to visualise the same vortex structure at $\phi = 120°$ and $168°$, respectively.

More interesting is the flow pattern of the chevron synthetic jet shown in Figures 4.11 and 4.12.

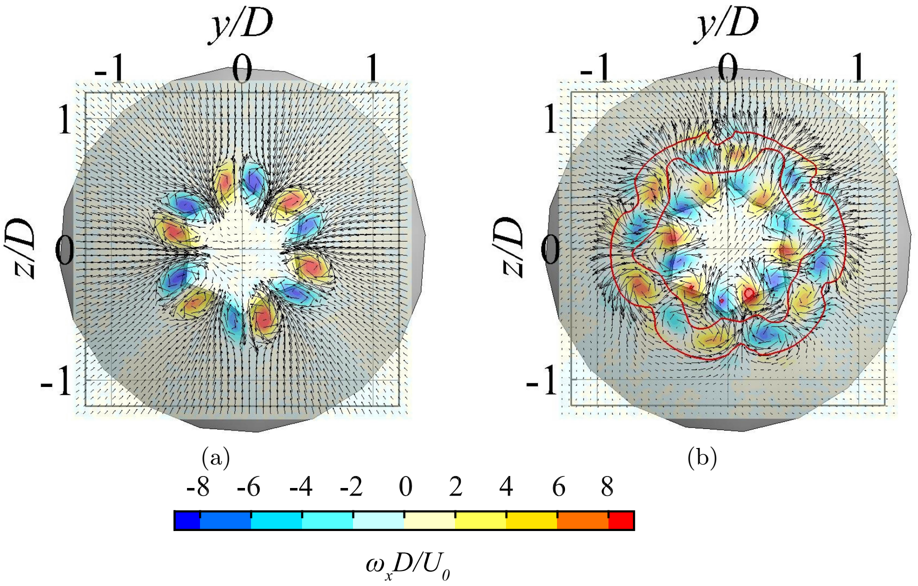

(a)

(b)

Figure 4.11: Crosswise slice at (a) $x/D = 1$ and (b) $x/D = 1.75$ at $\phi = 84°$ with $\omega_x D/U_0$ maps and red solid iso-lines of $QD^2/U_0^2 = 35$.

The effect of the chevron teeth is to re-orient the azimuthal vorticity into streamwise vorticity ($\omega_x$) (Violato and Scarano, 2011) with consequent formation of streamwise oriented counter-rotating vortices, six couples for the investigated nozzle configuration, generated at the notches of the chevron exit (Figure 4.11a). These counter-rotating vortices induce extra flow motions towards the jet axis and apart from the jet axis in correspondence of the notches and the apices respectively, as previously discussed. As a consequence, both the trailing jet and the vortex ring show a modified shape with respect to the conventional circular pattern. As a matter of fact, by looking at the cross-plane at $x/D = 1.75$ for $\phi = 84°$ in Figure 4.11b, the vortex ring is azimuthally modulated, as visualised through the iso-line of $Q$. The streamwise vortices induce opposite vorticity within the vortex ring as shown in Figure 4.11b. The presence of appreciable values of $\omega_x$ within a vortex ring may induce the phenomenon of the axis-switching (Grinstein et al., 1996). However, the mutual interaction between streamwise and azimuthal vorticity component prevents the self-deformation of the vortex ring in agreement with Zaman (1996). For this reason, the vortex ring convects downstream keeping unchanged its topology up to $\phi = 120°$ (where the vortex ring core is at approximately $x/D = 3$ from the nozzle exit). At a later stage of the ejection phase, both the streamwise vortices and the vortex ring become weaker; when the streamwise oriented counter-rotating vortices disappear ($\phi = 168°$) the vortex ring shows a circular shape. This is shown in Figure 4.12b. The evolution reflects the behaviour of non-circular jet to develop into an axisymmetric structure, as also seen by Gutmark and Grinstein (1999).

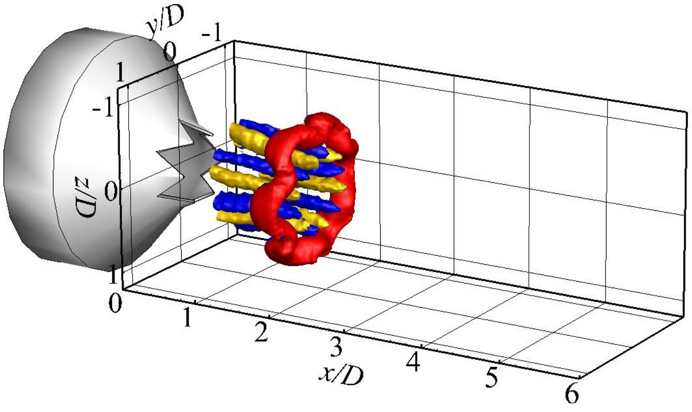

(a)

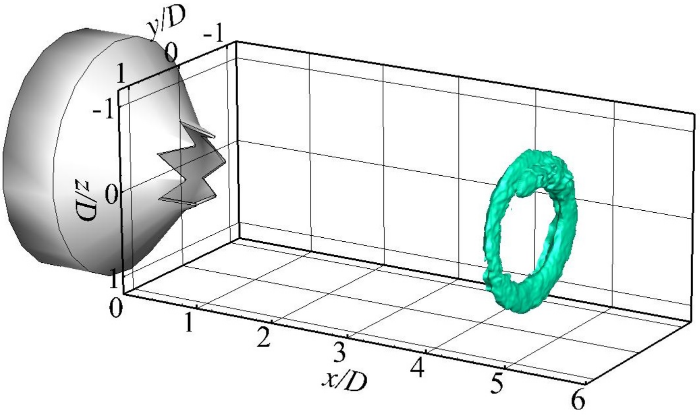

(b)

Figure 4.12: Three-dimensional reconstruction of the coherent vortex structures at $\phi$ equal to (a) 84° and (b) 168° for chevron synthetic jet with $QD^2/U_0^2$ iso-surface equal to 35 (red one) and 10 (light blue one) and $\omega_x D/U_0$ iso-surface equal to -4 (blue ones) and 4 (yellow ones) are represented.

## Chapter 5

# Heat transfer of a chevron synthetic jet

In this chapter, a comparison of the heat transfer properties of a chevron impinging synthetic jet with a circular one is carried out. The circular synthetic jet, taken as a reference case, is operated at Reynolds number equal to 4500 and the effect of the dimensionless stroke length (i.e. the inverse of Strouhal number) is taken into account by considering three different values: 9, 56, 112. The chevron synthetic jet is synthesised by keeping the same pressure oscillation in the device cavity. Since the chevrons elements present a little penetration depth, the head loss is small and the governing parameters at the nozzle exit are comparable.

## 5.1 Experimental procedure

### 5.1.1 Experimental setup

The experimental setup is sketched in Figure 5.1a. A thin constantan foil (200 mm long, 450 mm wide, 50 µm thick), whose flatness is ensured by a stiffening frame, constitutes the target plate. This plate is positioned horizontally and it is steadily and uniformly heated, via Joule effect, by using an external stabilized power supply. The target plate is cooled by a synthetic jet impinging normally on it. The synthetic jet device is obtained by coupling a contoured nozzle with a loudspeaker (HERTZ DS 25.3) through a wooden box as illustrated in Figure 5.1b. This device allows to obtain a wide range of $Re$ and $L_0/D$ conditions for the synthetic jet. The device operating parameters are continuously monitored using a Honeywell pressure transducer (HSCDRRN002NDAA5) which measures the pressure inside the cavity and two thermoresistances, one inside and another one outside the cavity, which monitor the cavity and ambient temperatures. To minimize the heating of the loudspeaker, the back-facing magnet is cooled by a water-based cooling system. The contoured nozzle has an exit diameter $D$ of 10 mm, it is 125 mm long and it presents a contraction ratio of 56:1. The nozzle is the same used in Chapter 4. The chevron configuration is obtained by applying the chevron exit cap (previously represented in Figure 4.1b) on the top of the contoured nozzle. The spacing between the nozzle exit and the target plate is adjusted by using a precision translation stage.

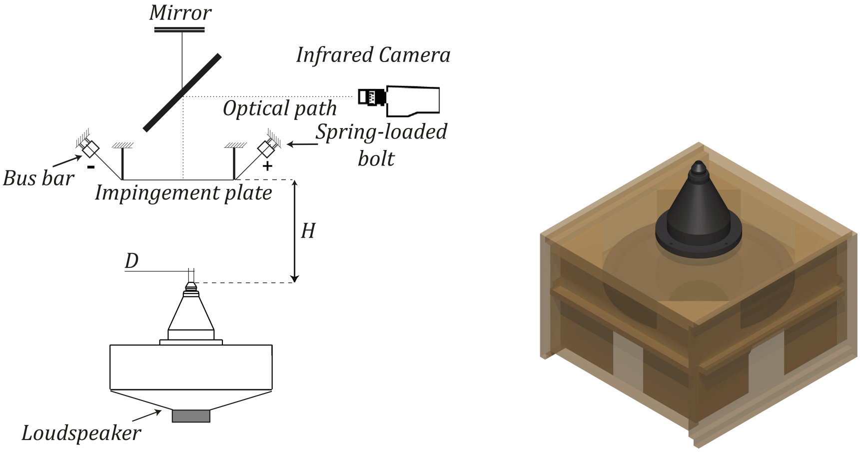

(a)

(b)

Figure 5.1: Sketch of the (a) experimental setup and (b) synthetic jet device.

The temperature of the foil is measured by an IR camera CEDIP JADE III (320 px × 240 px InSb focal plane array). This camera measures the temperature of the foil side opposite to the surface impinged by the synthetic jet. This is acceptable being the Biot number ($Bi = hs/k_f$, where $h$ is the convective heat transfer coefficient, $s$ is the foil thickness and $k_f$ is the thermal conductivity of the foil) and Fourier number ($Fo = \alpha/fs^2$, where $\alpha$ is the thermal diffusivity of the foil and $f$ is the oscillating frequency of the membrane) much smaller and greater than 1, respectively. The back side of the foil (i.e. the one opposite to the impingement area and imaged by the IR camera) is coated with high emissivity paint ($\varepsilon = 0.95$) in order to increase the signal-to-noise ratio with respect to the radiation coming from the surrounding ambient. The temperature map has a resolution of $2.3\,\mathrm{px\,mm^{-1}}$, thus corresponding to 23 px per diameter. The IR camera is calibrated with a black body for the whole measurement range taking also into account the mirror presence in the optical path. The NETD of the camera is about 25 mK and the root-mean-square error from the black body calibration is less than 0.1 K.

The IR thermography is used in conjunction with the heated thin foil heat flux sensor, described in Section 3.4. By applying the steady state energy balance to the foil, the convective heat transfer coefficient $h$ can be evaluated as reported in Equation 3.16. The heat flux input $\dot{q}_j$ is about $610\,\mathrm{W\,m^{-2}}$. In the central area of the impingement, the radiative heat flux $\dot{q}_r$ is less than 10 % of $\dot{q}_j$. For the natural convection heat flux $\dot{q}_{nc}$, the correlation employed in the present work (from Welty et al., 2009) results in a $\dot{q}_{nc}$ less than 14 % of $\dot{q}_j$ and the empirical correlation error is equal to 10 % of the total value $\dot{q}_{nc}$. For the term $\dot{q}_{tc}$, as suggested by Carlomagno and Cardone (2010), it is highly recommended to filter the temperature maps to reduce the effects of the measurement noise and of the residual error after the non-uniformity correction of the focal plane array. In this application a least square second order polynomial fitting 10 px × 10 px kernel is applied and this contribution is less than 5 % of $\dot{q}_j$.

In each experiment, the adiabatic wall temperature $T_{aw}$ distribution is measured by recording the temperature map of the target plate with the synthetic jet impinging on it and the electric current input off. This map is commonly referred to as “cold image”. Then, the corresponding “hot image” is recorded by imposing an electric power input large enough to provide a temperature difference of at most 15 K between $T_w$ and $T_{aw}$ on the surface of the impinged plate in order to carry out measurements with high accuracy but without affecting flow quality and system operability. For each temperature map 2000 images are recorded at a frame rate of 120 Hz and integration time of 450 µs.

The origin of reference frame is fixed at the centre of the target plane. The $x-$ axis is aligned with the jet centreline and $y-$ and $z-$ axes lie in the target plane (perpendicular to the $x-$ direction), forming a clockwise reference frame. Five dimensionless nozzle-to-plate distances are considered, namely $H/D = 2, 4, 6, 8$ and 10.

### 5.1.2 Test conditions and uncertainty analysis

The impedance of the synthetic jet device in both circular and chevron configurations is experimentally evaluated by measuring the loudspeaker voltage drop and electric current. Both synthetic jet configurations are characterised by two resonance frequencies equal to about 14 Hz and 107 Hz. The loudspeaker is driven by a sinusoidal input signal whose frequency and amplitude are changed depending on the $Re$ and $L_0/D$ (i.e. the inverse of $St$) required. The resulting operating conditions, $Re = 4500$ and $L_0/D = 9, 56$ and 112, are estimated by measuring the axial velocity component along the jet centreline at the nozzle exit with planar particle image velocimetry (PIV) technique. The chevron synthetic jet device is operated keeping the same cavity pressure measured for each condition of the corresponding circular configuration. The uncertainty for the pressure in the cavity is less than 1.25 %. The comparison is not performed at the same electric power input as it has been done in the previous chapter, because the system impedance affects the jet operating conditions. By working at the same pressure cycle in the cavity, the same amount of energy is transferred to the fluid. Hence, the fluid dynamics effects of the chevron exit on the heat transfer can be evaluated. In the following, $Re$ and $L_0/D$ related to the chevron case indicate the corresponding circular configuration. Since the chevrons elements present a little penetration depth, the head loss is small and the governing parameters at the nozzle exit are comparable. The details of the experimental set up are summarized in Table 5.1.

An uncertainty analysis on the measured values in Equation 3.16 is conducted as suggested by Moffat (1988). The Nusselt number distribution is recalculated perturbing the variables of Equation 3.16 with the related

Table 5.1: Details of the experimental setup for convective heat transfer measurements.

| | |
|---|---|
| Flow conditions | $Re = 4500$, $L_0/D = 9, 56, 112$, $H/D = 2, 4, 6, 8, 10$ |
| Sensor | constantan foil (50 µm thick, 200 mm long, 450 mm wide) |
| Recording device | IR camera CEDIP JADE III (320 px × 240 px InSb focal plane array) |
| NETD | 25 mK |
| Field of view | $12D \times 9D$ |
| Acquisition frequency | 120 Hz |
| Integration time | 450 µs |
| Recorded images | 2000 |
| Digital resolution | 2.3 px mm$^{-1}$ |

uncertainty (listed in Table 5.2). The main effect on the Nusselt number estimation is related to the relative temperature difference measurement. The total error is estimated as the 2-norm of the individual errors. The analysis leads to a 4.8 % of uncertainty for the local Nusselt number. The estimated error for $Re$, considering Equation 1.1, is less than 3.5 % and for $L_0/D$ (Equation 1.2) is less than 3 %.

### 5.1.3 Data reduction

The experimental data are reduced in dimensionless form in terms of Nusselt number

$$Nu = \frac{hD}{k} \tag{5.1}$$

where $h$ is the convective heat transfer coefficient, $D$ is the exit diameter of the nozzle and $k$ is the thermal conductivity of the air at the film temperature defined as $T_{film} = (T_w + T_{aw})/2$. The results are reported in terms of distribution maps of $Nu$, azimuthally averaged radial profiles $Nu_r$ and

Table 5.2: Error analysis according to Moffat (1988).

| | Typical Value | Uncertainty |
|---|---|---|
| $T_w$ | $317\,\mathrm{K}$ | $0.35\,\mathrm{K}$ |
| $T_{aw}$ | $303\,\mathrm{K}$ | $0.35\,\mathrm{K}$ |
| $T_w - T_{aw}$ | $12\,\mathrm{K}$ | $0.2\,\mathrm{K}$ |
| $T_{amb}$ | $303\,\mathrm{K}$ | $0.1\,\mathrm{K}$ |
| $I_f$ | $55\,\mathrm{A}$ | $1\,\%$ of reading |
| $V_f$ | $1.1\,\mathrm{V}$ | $1\,\%$ of reading |
| $\varepsilon$ | $0.95$ | $0.01$ |
| $D$ | $1 \times 10^{-2}\,\mathrm{m}$ | $1 \times 10^{-4}\,\mathrm{m}$ |
| $s$ | $50 \times 10^{-6}\ \mathrm{m}$ | $1 \times 10^{-6}\ \mathrm{m}$ |
| $\mu$ | $1.8 \times 10^{-5}\ \mathrm{Pa\,s}$ | $1.8 \times 10^{-7}\ \mathrm{Pa\,s}$ |
| $\rho$ | $1.16\,\mathrm{kg\,m^{-3}}$ | $1.16 \times 10^{-2}\mathrm{kg\,m^{-3}}$ |

enhancement ratio $\gamma$ of the Nusselt number, defined as follows:

$$Nu_r(r) = \frac{1}{2\pi}\int_0^{2\pi} Nu(r,\theta)\,d\theta \tag{5.2}$$

$$\gamma = \frac{Nu_{chev}}{Nu_{circ}} - 1 \tag{5.3}$$

In particular, the second parameter, $\gamma$, is useful to compare the heat transfer performance of the two exit geometries at the stagnation point $\gamma_0$.

## 5.2 Results

In this section, firstly, the $Nu$ maps are presented for both synthetic jets at $H/D = 2, 6, 10$ for $L_0/D = 112$ and $L_0/D = 9$, to point out the most relevant differences. Then, the effect of $L_0/D$ at fixed $H/D = 2$ on the heat transfer distribution of the chevron synthetic jet is analysed. A comparison of $Nu_r$ as a function of $r/D$ for both configurations is presented. Finally, $Nu_0$ as a function of $H/D$ and $L_0/D$ is reported for the circular and the chevron synthetic jets and the enhancement at the stagnation point $\gamma_0$ is shown.

### 5.2.1 Heat transfer maps and azimuthally averaged profiles

In Figure 5.2, the $Nu$ distribution maps of the circular synthetic jet for $L_0/D = 112$ are shown on the left column. At $H/D = 2$, a ring-shaped region with a local $Nu$ maximum appears at $r/D \approx 0.5$ and an outer region with a little $Nu$ hump appears at approximately $r/D \approx 1.5$. Both peaks are clearly visible in the following azimuthally averaged profiles in Figure 5.5. These local maxima are well observed and described for continuous jets (Gardon, 1962; Carlomagno and Ianiro, 2014) as well as for synthetic jets (Greco et al., 2014, 2017). Indeed, for high values of $L_0/D$, the flow regime of the synthetic jet is dominated by the trailing jet (McGuinn et al., 2013; Greco et al., 2017), and for this reason, it presents features similar to continuous jets. As well assessed in the literature for continuous (Jambunathan et al., 1992) and synthetic (Greco et al., 2018) circular jets, the Nusselt number in the central area of impingement increases as $H/D$ increases up to 6, where the maximum $Nu_0$ is achieved and then it decreases. The increase of $Nu_0$ could be related to the increasing turbulence levels up to $H/D = 6$ in the centre of the impingement area, as observed in other experimental studies (Greco et al., 2016, 2017). After this value, the increment in turbulence level could do not compensate for the velocity deficit, as observed for continuous jets (Jambunathan et al., 1992).

The heat transfer results obtained with the chevron cap show a different behaviour. The $Nu$ map on the right column of Figure 5.2, for $L_0/D = 112$ at $H/D = 2$, shows a characteristic 6-point-star pattern that resembles the shape of the nozzle exit (inner star-shaped region). The six regions of higher values of $Nu$, near the stagnation area, correspond to the nozzle notches and could be ascribed to the higher arrival speed on the plate. Between these regions, other six regions, corresponding to the apices of the chevron nozzle, are characterised by an extended area of enhanced heat transfer rate in the radial direction (outer star-shaped region). This effect could be caused by the interaction of streamwise structures (see Chapter 4), developed from the notches, with the impingement plate. Also in this case, the chevron synthetic jet exhibits characteristics similar to a continuous jet. Indeed, such a pattern has been observed for the analogous chevron continuous jet by Violato et al. (2012). For this nozzle-to-plate distance, at the centre of the impingement area, the chevron synthetic jet presents a larger heat transfer rate than that

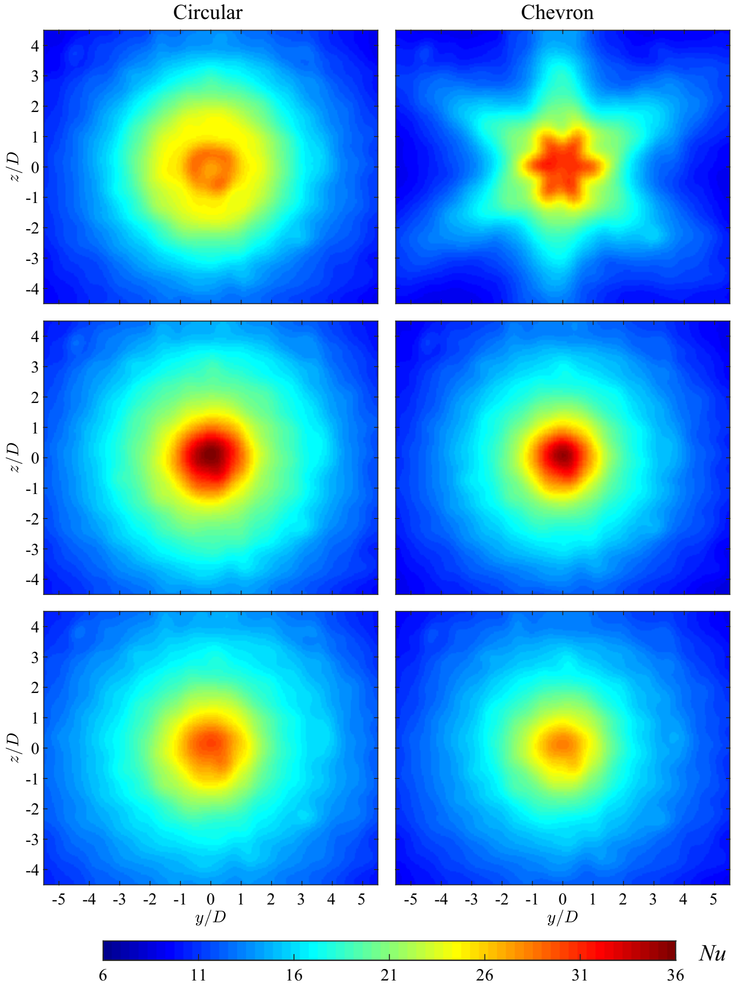

Figure 5.2: $Nu$ maps at $Re = 4500$ and $L_0/D = 112$ for the circular synthetic jet on the left column and the chevron synthetic jet on the right column at $H/D = 2$, 6 and 10.

of the corresponding circular case. This enhancement is probably caused by a higher arrival speed obtained with the chevron exit geometry, which acts as an additional converging nozzle as seen in Chapter 4. Passing from the nozzle-to-plate distance $H/D = 2$ to $H/D = 6$, the observed inner and outer star patterns of $Nu$ approach a circular pattern (as shown for chevron continuous jets by Violato et al., 2012). The pattern suggests an axisymmetric development of the chevron synthetic jet. At $H/D = 6$, the maximum $Nu_0$ is achieved, while at higher $H/D$, the heat transfer rate of the chevron configuration decreases achieving lower levels than the circular configuration. This latter aspect could be probably due to a reduction of the arrival speed and low turbulence levels in the centre of impingement at these nozzle-to-plate distances.

For $L_0/D = 9$, the left column of Figure 5.3 reports the $Nu$ maps for the circular configuration at $H/D = 2, 6$ and 10. At $H/D = 2$, differently from $L_0/D = 112$, the inner and outer ring-shaped regions are difficult to be observed, even if their presence is detected in Figure 5.5. It is interesting to note that in the central region of the impinged area, a quasi-uniform region of heat transfer achieves a $Nu$ enhancement of more than 40 % respect to the same configuration at $L_0/D = 112$. This is probably related to the shorter trailing jet and an enhanced entrainment due to the dominant effect of the vortex ring near the exit (Greco et al., 2017). At $H/D = 6$, the $Nu$ distribution presents a wider central impingement area of high heat transfer, in agreement with the broader jet width at lower $L_0/D$ found by Greco et al. (2017). By increasing $H/D$ up to 10, the heat transfer rate decreases.

On the right column of Figure 5.3, the heat transfer maps for the chevron configuration at $L_0/D = 9$ are shown. At $H/D = 2$ an appreciable increment of the $Nu$ in the impinged area is achieved, compared to the circular exit (about 16 % in the stagnation region), as better shown in the following Figure 5.5. The $Nu$ map presents a quasi-axisymmetric pattern, suggesting that a possible axisymmetric development of the jet starts closer to the exit probably related to the presence of weaker streamwise vortices. By increasing $H/D$, the heat transfer rate of the chevron synthetic jet increases. In the stagnation region at $H/D = 4$, the maximum $Nu$ value is achieved as shown in the following Figure 5.5. Then, the heat transfer rate decreases, but keeping higher values than those of the circular case. In particular, for $H/D \geq 6$, the heat transfer rates of the chevron and circular exits are comparable. In fact, for low dimensionless stroke length, the chevron exit geometry has no longer effects on the propagating jet at about this nozzle-to-

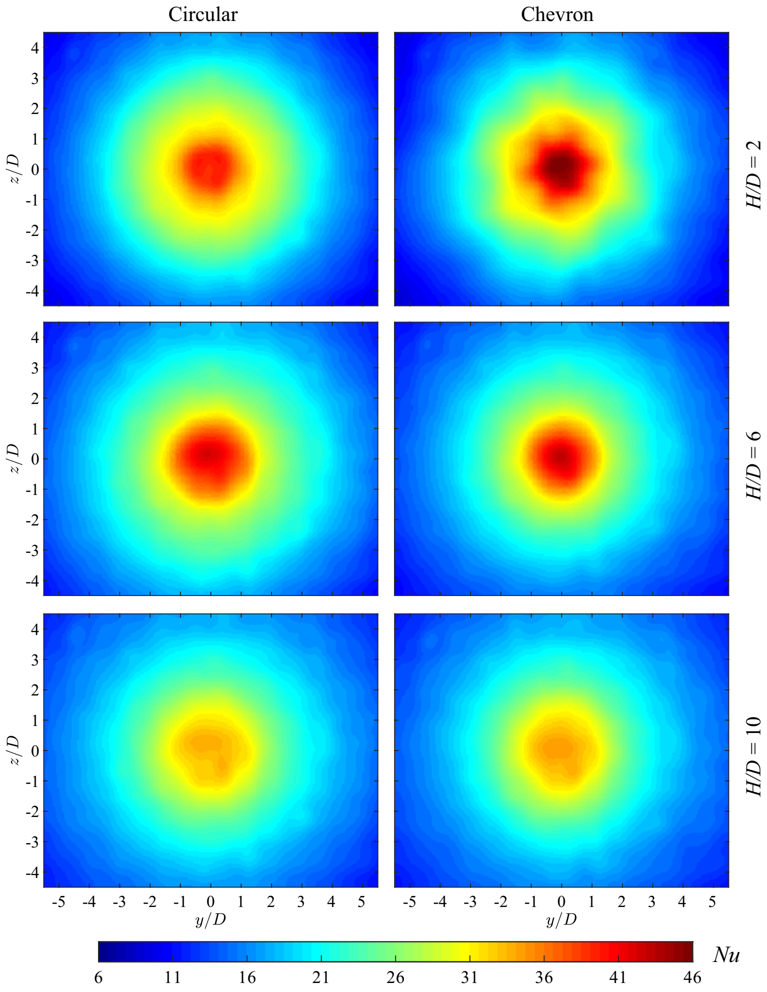

Figure 5.3: $Nu$ maps at $Re = 4500$ and $L_0/D = 9$ for the circular synthetic jet on the left column and the chevron synthetic jet on the right column at $H/D = 2$, 6 and 10.

plate distance (as seen in Chapter 4), so the chevron synthetic jet probably attains similar fluid dynamic features of the circular synthetic jet.

In order to assess how $L_0/D$ affects the heat transfer distribution of the chevron synthetic jet at $H/D = 2$, $Nu$ maps are shown in Figure 5.4. The $Nu$ distribution map passes from a quasi-axisymmetric pattern for $L_0/D = 9$, to a well-defined star-shaped pattern for $L_0/D = 112$ with a lower heat transfer. The quasi-axisymmetric distribution obtained for the shortest stroke length is probably due to a flow field characterised by the dominant effect of the vortex ring impinging on the target plate, compared to a relatively short trailing jet and weak streamwise vortices. As $L_0/D$ increases, six regions of enhanced heat transfer near the stagnation point become more evident, probably because of the longer trailing jet. Furthermore, stronger streamwise vortices are probably generated at the longer stroke length which could be responsible of the outer star-shaped extending region. This aspect will be clarified in Chapter 6. Hence, near the stagnation point the high axial momentum is probably the primary cause of the inner star-shaped pattern, while the streamwise vortices impinging on the target plate could be the main reason of the outer star-shaped pattern. At the centre of the impinged area, for short dimensionless stroke length, high heat transfer coefficients are achieved. This could be related to the enhanced entrainment and turbulent mixing induced by both the vortex ring and the streamwise vortices.

Radial profiles of the azimuthally averaged Nusselt number, $Nu_r$, are compared in Figures 5.5. For $L_0/D = 9$, at $H/D = 2$, the circular configuration presents a local maximum of heat transfer at $r/D \approx 0.5$ and a defined inflection point at about $r/D \approx 2$. The heat transfer features depart from those of continuous jets because of the short trailing jet and a dominant unsteady behaviour (the train of vortices is dominant). At the same nozzle-to-plate distance, the chevron jet shows a better heat transfer at the centre of the impingement region and a weak inflection point at about $r/D \approx 1.8$, respect to the circular case. At $H/D = 4$, in both cases the profiles assume a bell-like shape and the stagnation Nusselt number achieves the maximum value in both cases. Increasing the nozzle-to-plate distance, the heat transfer rate decreases for both configurations.

For $L_0/D = 56$, at $H/D = 2$, the circular synthetic jet shows the inner and the outer local maxima at about $r/D \approx 0.5$ and $r/D \approx 1.8$. Although the $Nu$ values are lower than that obtained at $L_0/D = 9$, these maxima are more pronounced. Regarding the inner annular maximum, it could be due to

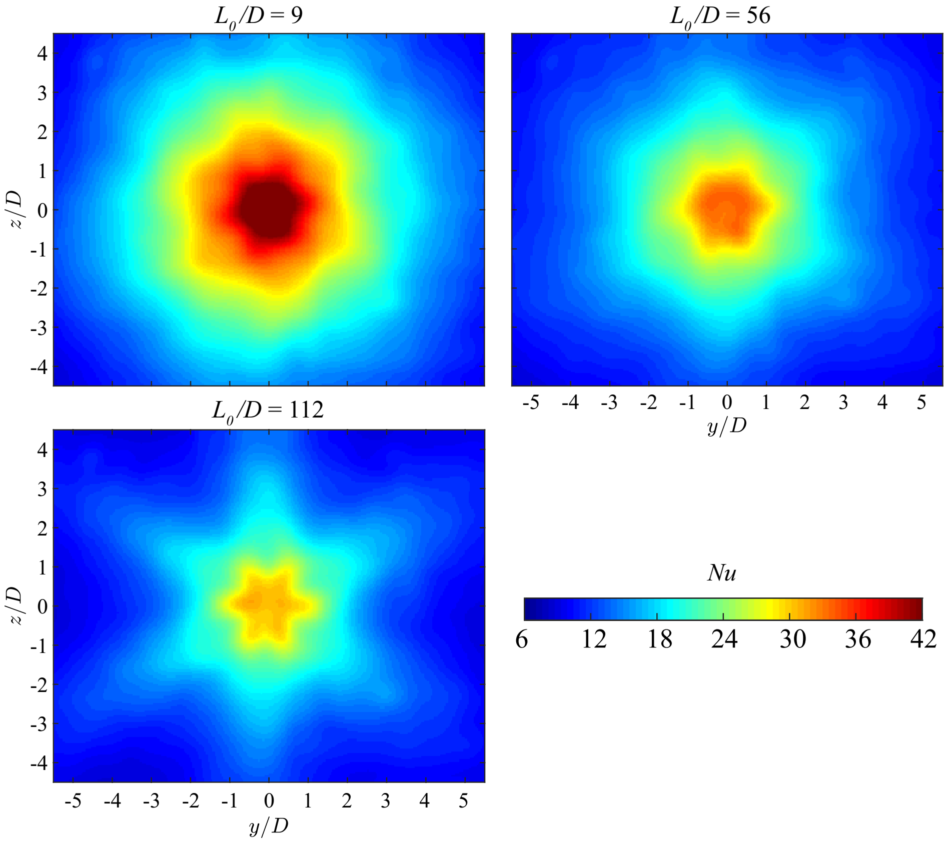

Figure 5.4: $Nu$ maps for chevron synthetic jet at $Re = 4500$, $L_0/D = 9$, 56 and 112 and $H/D = 2$.

the increment of the stroke length. As a consequence, the jet potential core-like region impinging on the plate is stronger. Whilst for the outer annular region, the cause could be ascribed to the primary vortex ring and the K-H instabilities of the trailing jet (Greco et al., 2018). At a radial location from the centre of about $r/D \approx 1.8$, the adverse pressure gradient along the wall and the sweeping vortex rings (both primary vortex rings and K-H instabilities) produce a counter-rotating vortex on the plate. This counter-rotating vortex ring will be shown in the next chapter for $L_0/D = 28$.

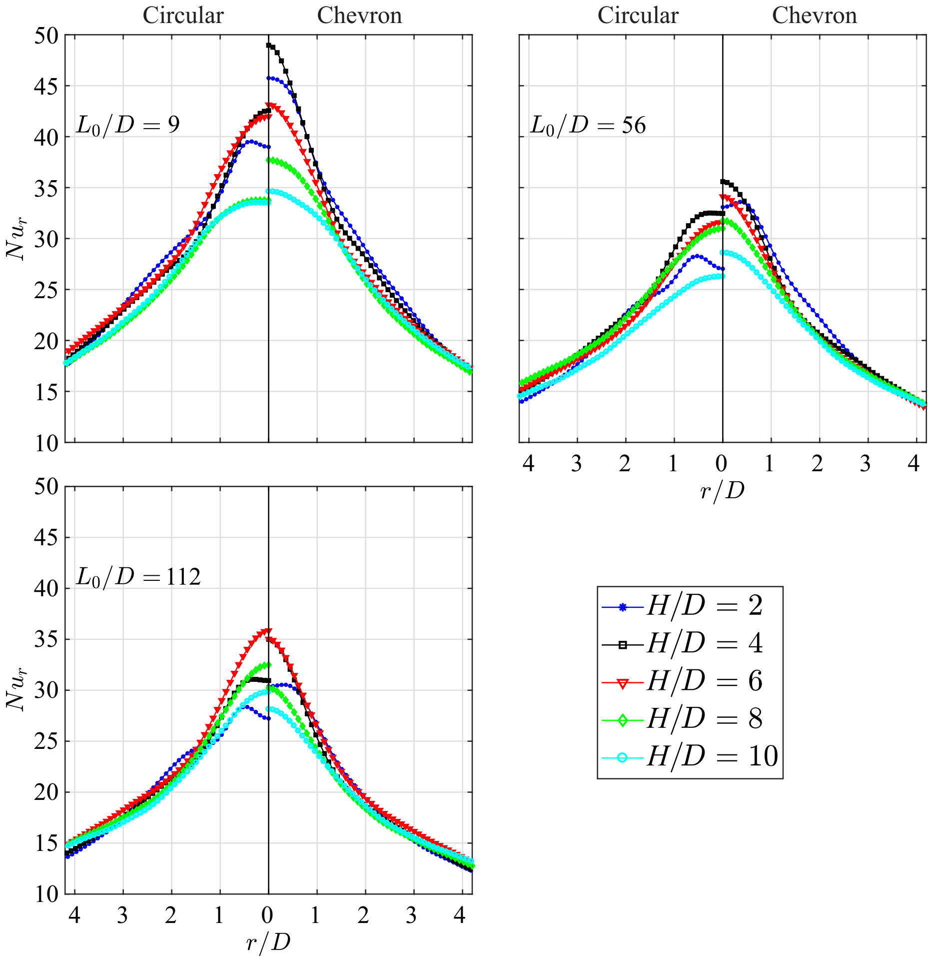

Figure 5.5: Comparison of $Nu_r$ as a function of $r/D$ at different $H/D$, for $L_0/D$ investigated. Circular synthetic jet on the left and chevron synthetic jet on the right.

For $L_0/D = 112$, at $H/D = 2$, the circular synthetic jet shows a local maximum at $r/D \approx 0.5$ (inner annular region) and a second maximum, a hump, at about $r/D \approx 2$ (outer annular region). Such regions are caused by the impinging potential core and the secondary vortex ring generation near the impingement plate, respectively. The chevron configuration presents a plateau for $r/D \leq 0.35$ and a fast decrease as $r/D$ increases. The $Nu_0$ is enhanced of about 10 % by applying the chevron cap with respect to the circular exit. This effect is probably due to a higher arrival speed and turbulent mixing induced by the chevron exit. At $H/D = 4$, in the circular case, the inner annular region is replaced by a plateau for $r/D \leq 0.5$, while the outer region is replaced by the presence of an inflection point at $r/D \approx 2$. Furthermore, at $H/D = 6$, the inflection point is no longer present, the $Nu_r$ profile assumes a bell-like shape and the maximum of $Nu_0$ is achieved. Differently, the chevron synthetic jet features a bell-shaped profile of $Nu_r$ starting from $H/D = 4$ achieving a maximum of $Nu_0$, that is held up to $H/D = 6$. Then, the heat transfer rate monotonically decreases in both cases for $H/D \geq 6$.

It is worth to note that as the stroke length decreases from $L_0/D = 112$ to $L_0/D = 9$, the Nusselt number increases and the maximum $Nu_0$ switches from $H/D = 6$, showing a behaviour similar to continuous jets, to $H/D = 4$. Moreover, the chevron jet produces higher increment of heat transfer for low nozzle-to-plate distances and tends to replace the inner annular peak, which is characteristic for the circular case, with a central region of more uniform enhanced heat transfer. These aspects will be clarified in the following.

### 5.2.2 Heat transfer enhancement at the stagnation point

In this section, $Nu_0$ as a function of $H/D$ and $L_0/D$ is reported in Figure 5.6a and Figure 5.6b for the circular and the chevron synthetic jets, respectively. The enhancement at the stagnation point $\gamma_0$ is shown in Figure 5.6c. The white dots reported in Figure 5.6 are the measured values, while the remaining part of these maps is obtained by data interpolation. These maps allow to infer the heat transfer trends and best operating conditions, in terms of $H/D$ and $L_0/D$, for circular and chevron impinging synthetic jets at the stagnation point.

Figure 5.6a shows that the circular exit exhibits the greatest heat transfer rates at the stagnation point for $L_0/D = 9$. A region of operating conditions in which the circular synthetic jet is characterised by optimal heat transfer rate at the stagnation area is observed approximately for $L_0/D \approx 9$ and

$4 \leq H/D \leq 6$. Passing from $L_0/D = 9$ to $L_0/D = 112$, the reduction of the thermal performance might be attributed to a flow regime uniquely dominated by the trailing jet which suppresses the contribution of the unsteady train of vortex rings to the heat transfer process through its entrainment and turbulent mixing. Hence, $L_0/D = 9$ seems to be an operating condition at which the effects of both the vortex ring and the trailing jet give a proper contribution to the heat transfer rate. It is worth to note that the maximum $Nu_0$ is achieved at $H/D = 6$ for $L_0/D = 112$ and at $H/D \approx 4 - 6$ for $L_0/D = 9$. Probably, this is addressed to a longer or shorter extension of the potential core of the jet, respectively (Greco et al., 2018).

As for the circular exit, Figure 5.6b shows that the chevron synthetic jet exhibits high values of $Nu_0$ for $L_0/D = 9$. The maximum $Nu_0$ is shifted of about $1D$, with respect to the circular case. Optimal stagnation heat transfer conditions are obtained, approximately, for $L_0/D \approx 9$ and $3 \leq H/D \leq 5$. The chevron synthetic jet exhibits better heat transfer rate for small nozzle-to-plate distances. This result could be probably ascribed to two effects: the increased jet velocity and the increased turbulent mixing introduced by the chevron cap. In particular, it is worth to note that the maximum $Nu_0$ is achieved at $H/D \approx 4 - 6$ for $L_0/D = 112$ and at $H/D \approx 2 - 4$ for $L_0/D = 9$. Probably, the potential core-like region is shorter than that of the circular case because of a more penetrating shear layer.

In order to point out the heat transfer enhancement effect, at the stagnation point, of the chevron exit compared to the circular one, Figure 5.6c reports the stagnation enhancement $\gamma_0$ defined in Equation 5.3. According to the uncertainty propagation theory (Taylor, 1997), the uncertainty range of $\gamma_0$ is $\pm 0.1$. Therefore, the iso-level lines of enhancement $\gamma_0$ starting from $\gamma_0 = 0.15$ are taken into account in Figure 5.6c. The chevron cap results more effective for low nozzle-to-plate distances and short dimensionless stroke lengths. As well assessed in literature, for free chevron continuous jets (Doty et al., 2007; Zaman et al., 2011) and experimentally seen in Chapter 4 for a free chevron synthetic jet, the chevron geometry has the effect of modifying the turbulence distribution with respect to a circular exit, by increasing the turbulence level near the nozzle exit and reducing it at higher distances from the exit. Hence, this increase of $Nu_0$ at low nozzle-to-plate distances can be related to high turbulent-induced mixing near the exit, caused by streamwise vortices that develop from the chevron notches. At $L_0/D = 9$, the enhancement of the chevron jet is observable for a relatively wider range of nozzle-to-plate distances. A possible explanation may be that the shorter trailing jet makes the turbulent mixing and jet entrainment of both primary vortex ring and streamwise vortices, more effective for relatively longer distances. Whilst, by increasing $L_0/D$, gradually the vortex ring effect reduces and stronger streamwise vortex structures might both increase the heat transfer rate and shift their effect for low nozzle-to-plate distances (region $\gamma_0 \geq 0.2$ in Figure 5.6c). In such case, the streamwise structures are almost solely responsible for the turbulent mixing and jet entrainment. The maximum heat transfer enhancement is observed for $H/D = 2$ and $L_0/D \approx 28$. This condition will be investigated in the next chapter.

The outcome of the present analysis is that for the inspected $Re$ and $L_0/D$ numbers, the chevron case is more efficient than the circular one under the same cavity pressure at short nozzle-to-plate distances. Nevertheless, this aspect exasperates the non-uniformity (star-shaped pattern of the Nusselt number distribution in Figure 5.4) of the radial distribution of the Nusselt number for high stroke lengths.

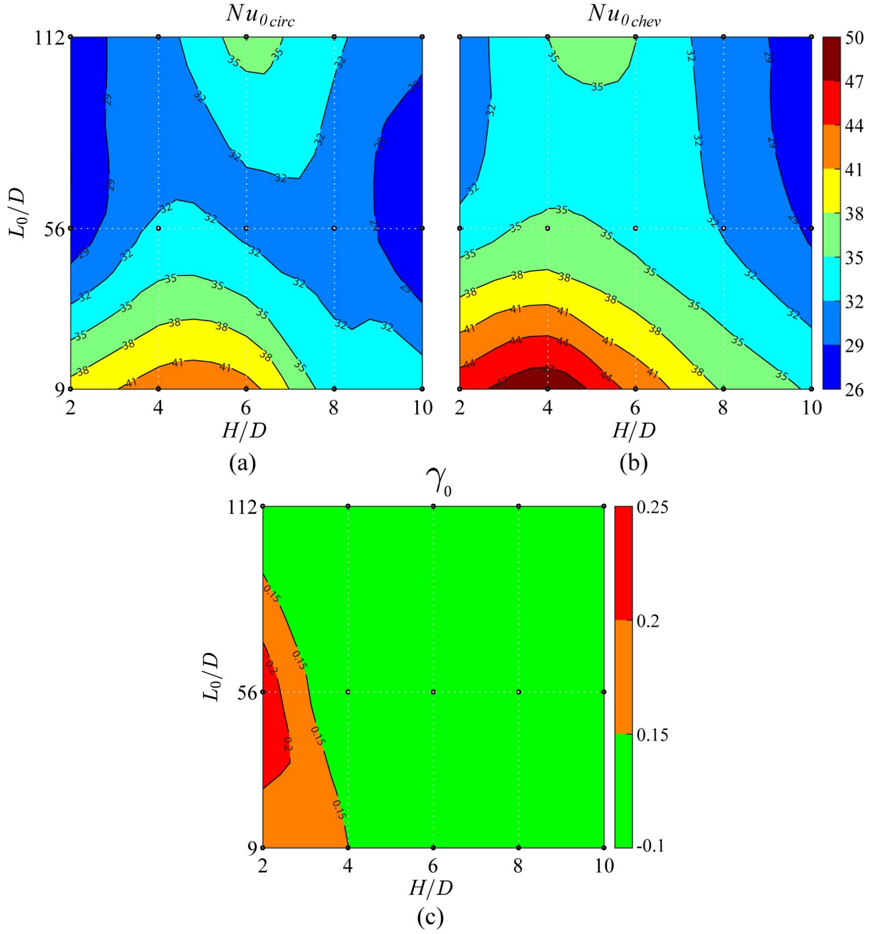

Figure 5.6: $Nu_0$ as a function of $L_0/D$ and $H/D$ for (a) circular and (b) chevron synthetic jets and (c) heat transfer enhancement, $\gamma_0$, as a function of $L_0/D$ and $H/D$.

# Chapter 6

# Flow field of a chevron impinging synthetic jet

The flow field of a chevron synthetic jet in impinging configuration is analysed at the condition of maximum heat transfer enhancement. Based on the heat transfer enhancement results of the previous chapter, the condition at Reynolds number $Re = 4500$, dimensionless stroke length $L_0/D = 28$ and nozzle-to-plate distance $H/D = 2$ is investigated. The effect of the presence of the impinging plate onto the flow field organisation is discussed by comparison with the case of a circular synthetic jet. Two different experiments are carried out. The first experiment is devoted to the characterisation of the flow field evolution on the impingement plate. The second experiment is a complete 3D reconstruction of the entire flow field at the phases chosen by analysing the results obtained through the first experiment. Three phases are reconstructed corresponding to three synthetic jet conditions: approaching vortex, impinging vortex and flow developing on the plate.

## 6.1 Experimental procedure

### 6.1.1 Experimental setup

The synthetic jet device is the same as used in Chapter 5. It is worth recalling that it is realised by coupling a contoured nozzle with a loudspeaker

(HERTZ DS 25.3) through a wooden box as already shown in Figure 5.1b. The contoured nozzle and the chevron cap (used to realise the chevron configuration) have been already described in both Chapters 4 and 5.

A glass square impingement plate is located at a fixed distance of two diameters from the nozzle exit section. The size of the glass plate ($30D \times 30D$) is chosen so that boundary effects on the flow field are negligible. The positioning of the impingement plate is regulated by means of a translational and rotational system, which ensures micrometre accuracy.

The origin of the reference frame is fixed at the centre of the round nozzle exit section. The $x-$axis, perpendicular to the impingement plate, is aligned with the jet centreline and the $y-$ and $z-$axes lie in the plane perpendicular to the $x-$direction, forming a clockwise reference frame. A sketch of the adopted reference frame is reported in Figure 6.1.

Stereo-PIV technique is used to measure the 2D-3C velocity field. Two different Stereo-PIV experiments are performed. The first experiment is devoted to the characterisation of the flow field evolution near the impinged plate: particle images are acquired in the $y-z$ plane 1 mm off the plate. The second experiment is a complete 3D reconstruction of the entire flow field at three phases, chosen by analysing the results obtained through the first experiment. In particular, this reconstruction is performed by sliding both the synthetic jet device and the impingement plate. Indeed, the synthetic jet device together with the impingement plate are placed on a support base fixed on a slide with micrometre accuracy and the flow field is scanned along the $x-$ direction with 21 planes across the vortex core (Figure 4.2b). The distance between two subsequent planes is set to $\Delta x = 0.5\,\mathrm{mm}$ ($0.05D$). For each plane, 300 double frame particle images are acquired.

The flow is seeded with oil droplets with a diameter of approximately 1 µm generated by a Laskin nozzle. Illumination is provided by the Quantel Evergreen laser that is a double pulsed Nd:YAG laser (532 nm, 200 mJ per pulse, <10 ns pulse duration). The time separation between the two laser pulses is set to $\Delta t = 17\,\mu\mathrm{s}$. The laser sheet thickness is about 1 mm. Particle images are recorded by two Andor Zyla sCMOS cameras ($2160\,\mathrm{px} \times 2560\,\mathrm{px}$, 16 bit, $6\,\mu\mathrm{m\,px}^{-1}$) equipped with Scheimpflug adapters and Tokina 100 mm focal length objectives. The optical objective is set at numerical aperture $f_{\#} = 16$ for the camera looking in forward scattering configuration (camera

1 in Figure 6.1) and $f_{\#} = 11$ for the camera looking in backward scattering configuration (camera 2 in Figure 6.1), in order to compensate for the different brightness condition. The angle between the two cameras is about 97°. The resulting digital resolution is $26\,\mathrm{px\,mm^{-1}}$. The measurement domain ranges between $0.9 \leq x/D \leq 1.9$, $-5 < y/D < 5$ and $-4 < z/D < 4$. The acquisition system is synchronized with the synthetic jet in order to perform phase-locked measurements. The synchronization is realised by using a Digilent Inc. Analog Discovery. The input signal to the loudspeaker is used also as a trigger for the acquisition system. The acquisition is performed at the frequency $f_{acq}$ estimated following Greco et al. (2013) as reported in Equation 4.1. The phenomenon is sampled with a phase separation $\Delta\phi = 6°$. In order to obtain reliable turbulent statistics, 18000 double frame particles images (300 snapshots per phase) are recorded.

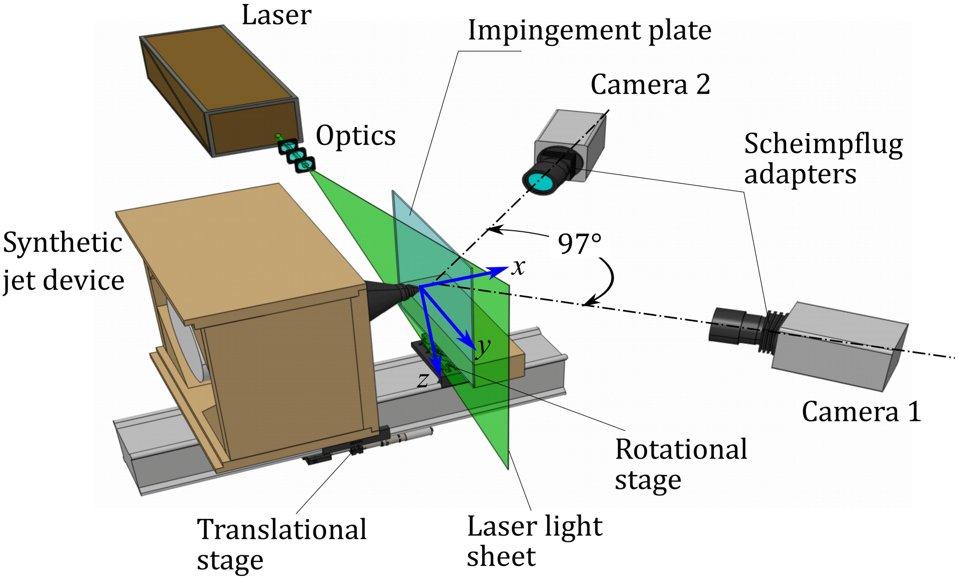

Figure 6.1: Sketch of the experimental setup in impingement configuration.

### 6.1.2 Test conditions and PIV measurement details

The loudspeaker is driven by a sinusoidal input signal with a frequency of 25 Hz by a Diligent Inc. Analog Discovery coupled with an amplifier. At this working frequency, the two synthetic jet configurations present the same impedance. The voltage amplitude is adjusted in order to realise $Re = 4500$ and $L_0/D = 28$ for the circular configuration. The resulting operating conditions are estimated by measuring the axial velocity component along the jet centreline at the nozzle exit with planar PIV experiments. By applying the chevron cap, the voltage amplitude is set to obtain the same cavity pressure measured for the circular case, as already discussed in Section 5.1.2. In the following, $Re$ and $L_0/D$ related to the chevron case indicate the corresponding circular configuration.

An in-house software based on a multi-pass algorithm with windows deformation and Blackman weighting windows (Astarita and Cardone, 2005; Astarita, 2006, 2007, 2008) is used to compute the velocity fields. The final interrogation window size is 32 px × 32 px with an overlap of 75 %, thus resulting in a vector pitch of 0.3 mm (approximately 32 vectors per diameter). A normalised median validation criterion (Westerweel and Scarano, 2005) is applied to remove spuriously detected vectors. The displacement uncertainty, related to the peak localisation, is the main contribution to velocity uncertainty. For the given particle size (approximately 3-4 px), image noise and particle displacement, the random error is found to be approximately 2 % of the maximum velocity in the jet core.

The calibration procedure for the Stereo-PIV experiments is performed by taking images of a target (black dots on white background, 5 mm pitch) moved through the measurement volume in five different locations using a translational micrometre stage. The maximum calibration error is of about 0.5 px. A disparity procedure is then carried out to correct the location of the laser sheet and to reduce reciprocal misalignment between cameras and laser sheet.

A pre-processing, consisting in temporal minimum image subtraction, is applied to the raw images in order to reduce the background noise. The details of the experimental set up are summarized in Table 6.1.

Table 6.1: Details of the experimental setup for impinging flow field.

| | |
|---|---|
| Flow conditions | $Re = 4500$, $L_0/D = 28$, $H/D = 2$ |
| Seeding material | olive oil particles - 1 µm diameter |
| Illumination | Quantel Evergreen Nd:YAG laser (532 nm, 200 mJ per pulse, <10 ns pulse duration) |
| Recording device | 2 Andor Zyla sCMOS cameras (2160 px × 2560 px, 16 bit, 6 µm px$^{-1}$) |
| Recording method | double frame - single exposure |
| Optical arrangement | Tokina 100 mm focal length objectives, $f_{\#} = 16$ forward scattering camera, $f_{\#} = 11$ backward scattering camera, Scheimpflug adapters |
| Field of view | $10D \times 8D$, $1D$ scanned, $0.05D$ spatial step |
| Pulse separation | 17 µs |
| Recorded images | 300 snapshots/phase (evolution on the plate)<br>300 snapshots/plane (3D reconstruction) |
| Digital resolution | 26 px mm$^{-1}$ |
| Interrogation window size | 32 px × 32 px, overlap 75 % |

### 6.1.3 Data reduction

The data are reduced as previously reported in Section 4.1.3. The data measured in the $y - z$ plane are reported in a polar reference frame. Hence, in-plane radial and azimuthal $U_r$, $U_\theta$ velocity components along the radial and azimuthal directions are shown to better explain the phenomenon.

## 6.2 Results

In this section, the mean and statistical flow fields of both the circular and chevron synthetic jets are discussed. Then, the phase-averaged measurements are presented. Finally, the circular and chevron synthetic jet flow field reconstructions are reported at three significant phases. Since the circular case is axisymmetric, the azimuthal velocity component is not reported for it.

### 6.2.1 Time-averaged impinging flow field

Figures 6.2 and 6.3 report the mean axial and radial velocity components and the turbulent kinetic energy maps for the circular and chevron synthetic jet, respectively.

The circular synthetic jet is characterised by a local minimum of axial velocity $U$ in the stagnation region, while it attains a maximum at a radial location of about $r/D \approx 0.5$, as shown in Figure 6.2a. As the flow approaches the plate, the axial velocity component decreases and undergoes a change of direction into parallel to wall direction. As a matter of fact, the impingement plate presence causes an axial velocity decrease, and as a consequence, an adverse pressure gradient is formed. Figure 6.2b shows a minimum of radial velocity component at the stagnation region, then the flow suddenly accelerates along the impinged surface. Therefore, a favourable pressure gradient on the plate is established. A maximum of radial velocity $U_r$ occurs at a radial distance of about $0.6D$ from the centre of impingement. This first inner annular peak of $U_r$ is due to the sudden change of direction of the axial velocity. A second outer annular peak of radial velocity, located at about $r/D \approx 1.8$, is visible. This second peak is ascribed to the formation of a secondary vortex ring on the plate, as it will be show in the following. The $TKE$ map in Figure 6.2c presents two annular peaks at approximately the same location of the annular peaks of radial velocity. This indicates that the regions where the radial velocity achieves a maximum, the flow experiences an increase of the fluctuation level. At the stagnation region, the turbulent kinetic energy is very low, this is ascribed to the potential core-like region extension impinging on the plate (Greco et al., 2016).

These findings allow for a better understanding of data in Chapter 5. The significant axial and radial velocity values and turbulent kinetic energy levels around the central region of impingement are responsible for the presence of the inner local maximum in the Nusselt number distribution. Furthermore, the radial profile of Nusselt number (reported in Figure 5.5) presents a second maximum of heat transfer at a radial distance of about $r/D \approx 2$. Figure

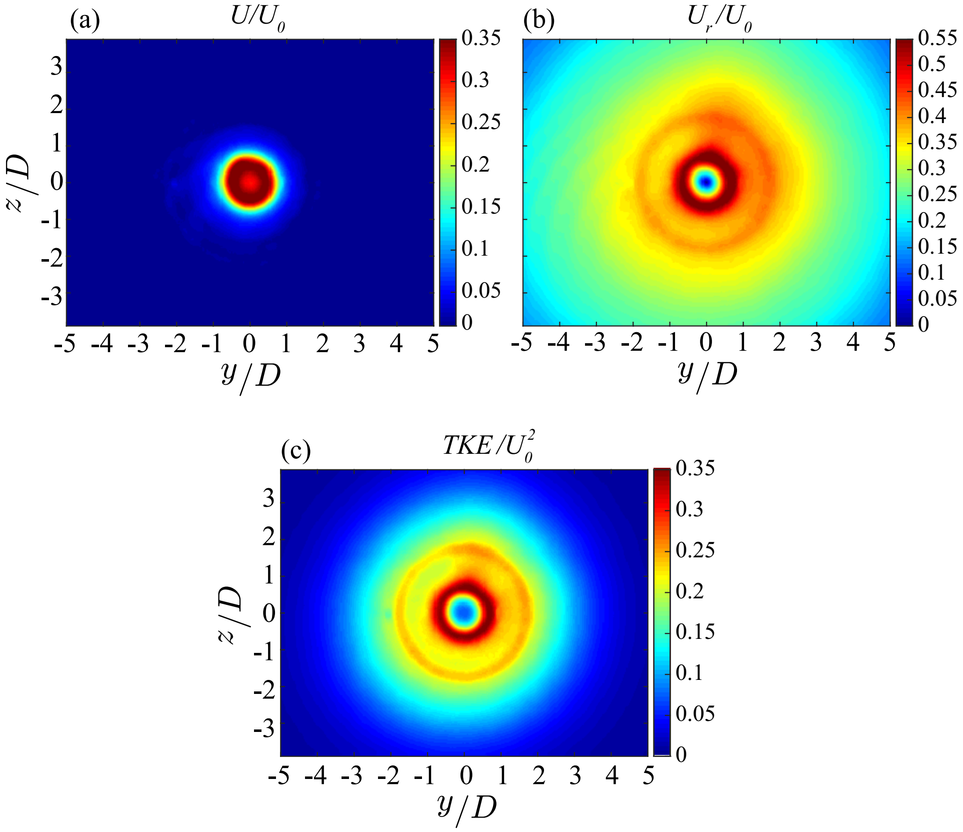

Figure 6.2: Time-averaged (a) axial, (b) radial velocity components and (c) turbulent kinetic energy maps for the circular synthetic jet.

6.2 shows average significant $U_r$ and $< TKE >$ values at such a location. In order to better describe these mean flow features and the related heat transfer, it is useful to refer to the phase-averaged measurements.

Figure 6.3a shows that, similar to the circular case, the chevron synthetic jet presents a minimum of axial velocity close to the central region of impingement. This region is surrounded by a six-point-star shaped region of higher axial velocity component due to the flow issued from the nozzle notches. As the fluid approaches the impinged wall, the momentum is trans-

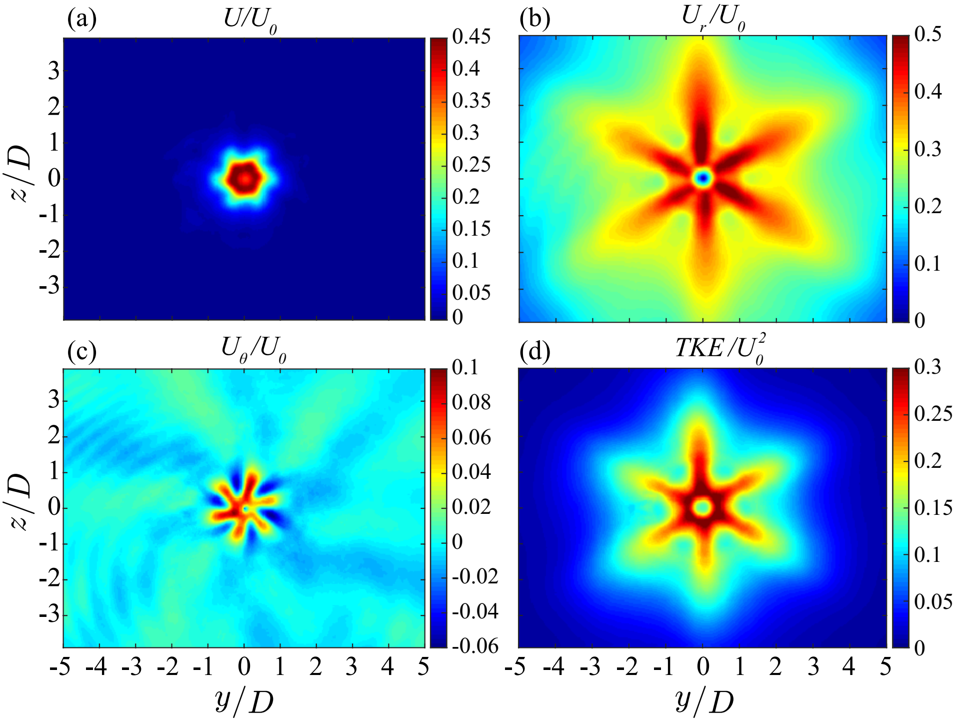

Figure 6.3: Time-averaged (a) axial, (b) radial, (c) azimuthal velocity components and (d) turbulent kinetic energy maps for the chevron synthetic jet.

ferred from the axial to the radial component. In this case, as in the circular one, the adverse pressure gradient influences the flow acceleration in the radial direction. The peculiarity here is represented by the presence of the alternating regions of high and low radial velocity component, as shown in Figure 6.3b. The higher values of radial velocity component are measured along the directions corresponding to the apices of the nozzle. This aspect is due to the fact that the jet experiences an axis-switching like behaviour on the wall, as characteristic for cross-shaped continuous jets (Rau et al., 2014). This behaviour could be explained considering the trailing jet and the counter-rotating streamwise vortices impinging on the wall. The star-shaped morphology of the trailing jet at the impingement and the presence of the streamwise vortices impinging on the plate generate preferential outflow paths from the notch towards the apex directions, resulting in high momentum flow along these directions. The azimuthal velocity component, in Figure 6.3c, illustrates that high momentum fluid is convected from the notch to the apex directions. The map in Figure 6.3d presents the $TKE$ distribution for the chevron synthetic jet. A local minimum of $TKE$ at the stagnation region is present. Around the stagnation region, high values of the $TKE$ are measured, in the region where the momentum is transferred from the axial to the radial component, with a maximum of $TKE$ at $r/D \approx 0.4$. It is interesting to note that the directions of the apices are characterised by large fluctuations values. This could be ascribed to the radial outflow and to its interaction with the passage of the vortex ring.

It is interesting to note that the star-shaped impinging jet (with six points) of high axial velocity values (shown in Figure 6.3a) is the main cause of the presence of the inner star-shaped pattern in the Nusselt number distribution. The developing wall jet, with preferential outflow paths in correspondence of the apex directions, gives a grasp of the presence of the outer star-shaped pattern of the Nusselt number distribution. Like in the circular case, Figure 5.5 shows an inflection of the Nusselt number profile at a radial distance of about $r/D \approx 1.8$, whose presence will be clarified in this chapter.

### 6.2.2 Phase-averaged impinging flow field

The phase evolution of the two configurations is discussed observing both the phase-averaged velocity components and turbulent kinetic energy fields. The starting phase $\phi = 0°$ is considered as the phase corresponding to the maximum increase of axial velocity component measured along the jet axis at the closest location to the impingement plate (in the first experiment).

The phase evolution of the circular synthetic jet on the impingement plate is reported in Figure 6.4 where the phase-locked axial $< u >$ and radial $< u_r >$ velocity components are reported in the first and second column, respectively. The phase-averaged turbulent kinetic energy $< TKE >$ is shown in the third column.

At $\phi = 0°$, the flow field induced ahead of the circular vortex ring is detected in the measurement plane. A uniform region of $< u > /U_0 \approx 0.6$ is present for $r/D < 1$. The radial velocity induced ahead of the vortex ring is zero at the stagnation region, it increases up to a maximum of $1.3U_0$ at $r/D \approx 0.8$, then it decreases monotonically with the radial direction. Subsequently, the jet impinges on the plate and the flow spreads radially outward almost parallel to the impinged plate. The vortex ring travels along the wall and at $\phi = 18°$, a central minimum of $< u >$, caused by the adverse pressure gradient at the impingement, surrounded by an annular region of maximum axial velocity is present. The axial velocity distribution in the central area of impingement, still present for subsequent phases, is responsible for the inner annular ring of heat transfer observed in Chapter 5. The presence of the primary vortex ring and the formation of a small counter-rotating secondary vortex ring is observed, from the map of axial velocity component, at a radial location of approximately $r/D \approx 2.1$. At this phase (i.e. $\phi = 18°$), an annular region of upwash (i.e. away from the wall), surrounded by two annular regions of downwash, is produced by the effect of the primary and secondary vortex rings. The formation of the secondary vortex ring is the same which occurs in impinging continuous jets as also observed in Hadžiabdić and Hanjalić (2008); Rohlfs et al. (2012). The generation of this counter-rotating secondary vortex ring is ascribed to the combined effect of the sweeping primary vortex ring and the adverse pressure gradient, caused by it, along the wall. Such a phenomenon induces a local reverse flow in the quiescent fluid ahead of it, initiating separation and the formation of the counter-rotating secondary vortex ring.

In particular, by looking at the investigated phases not reported here, the secondary vortex ring begins the first formation stage at $\phi = 12°$ located at about $r/D \approx 1.8$. It reaches the maximum intensity at $\phi = 18°$ with a radial position about $r/D \approx 2.1$, then at $\phi = 24°$ approaches $r/D \approx 2.5$ where its intensity is reducing and finally it is no longer detected at $\phi = 30°$.

For $\phi = 18°$, at the primary vortex ring location, the radial velocity map shows a strong radial velocity component at $r/D \approx 1.7$ and an outer annular region of low value at $r/D \approx 2.1$. This latter region is ascribed to the radial velocity induced by the secondary vortex ring. In the central impingement region, the trailing jet, following the primary vortex ring, is impinging on the wall as shown by $< u >$ and $< u_r >$ maps. At $\phi = 36°$, the axial velocity

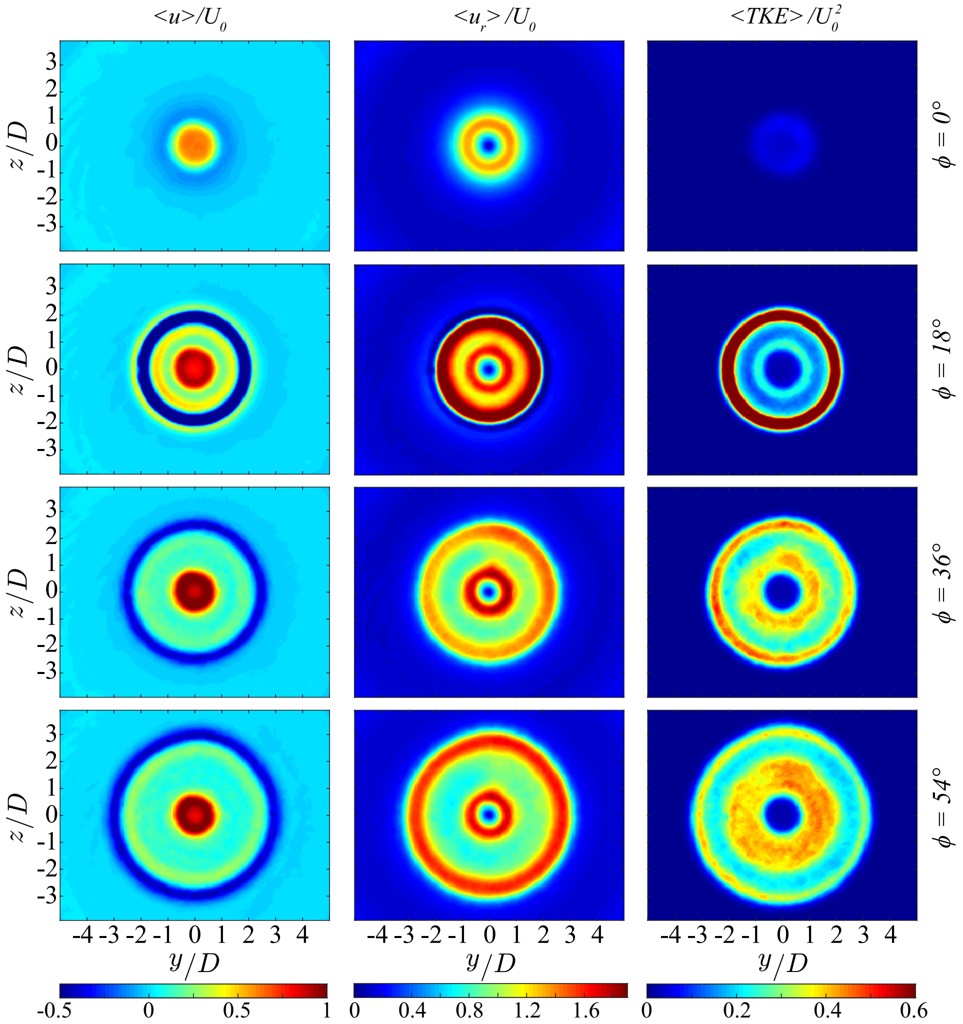

Figure 6.4: Phase-averaged (first column) axial, (second column) radial velocity components and (third column) turbulent kinetic energy for the circular synthetic jet.

near the centre of the impingement achieves a maximum value. This suggests that the axial velocity maximum is located downstream of the vortex ring in the trailing jet. The velocity field induced by the primary vortex ring is weak because of the lift-up of the vortex as shown in the following 3D reconstruction of Figure 6.7c. At the subsequent phase $\phi = 54°$, the radial velocity component induced by the sweeping primary vortex ring increases. Probably, the primary vortex ring is approaching the wall again.

The phase evolution of the $< TKE >$ indicates a high fluctuating behaviour as the counter-rotating secondary vortex ring is formed ($\phi = 18°$). The interaction of the two counter-rotating vortex rings promotes the turbulence. The average location of the secondary vortex ring $x/D \approx 1.8 - 2.5$ clarifies the presence of the outer annular region in the time-averaged measurements in Figure 6.2. When the following trailing jet impinges on the wall (phases 36° and 54°), two zones of significant $< TKE >$ are present: at the vortex ring position and around the stagnation region. The former is ascribed to the turbulent vortex ring passage. The latter must be ascribed to the shear layer of the trailing jet. Moreover, the extent of this region increases passing from 36° to 54° since, it must be taken into account the concurrent effect of the spreading of the jet. In fact, as the high axial velocity fluid in the trailing jet impinges on the plate, the shear layer is stronger and wider and it causes a large region of increased turbulence (as also seen by Greco et al. (2016)).

It is worth nothing that, during the flow evolution, the location of the primary and secondary counter-rotating vortices, ranging between $r/D \approx$ 1.8 and 2.5, sorts out the formation of the outer annular peaks reported in the mean flow of Figure 6.2. These vortical structures are responsible for the local maximum of heat transfer at $r/D \approx 2$ observed in the previous Figure 5.5.

For the chevron synthetic jet, Figure 6.5 reports the phase-locked axial $< u >$, radial $< u_r >$ and azimuthal $< u_\theta >$ velocity components in the first, second and third column, respectively. The phase-averaged turbulent kinetic energy $< TKE >$ is shown in Figure 6.6. Different phases are reported for the chevron impinging synthetic jet, since the impingement plate presence affects the flow evolution.

At $\phi = 0°$, the axial velocity map shows a characteristic six-point-star pattern that resembles the shape of the orifice. The second column of Figure 6.5 illustrates that outwards flow patterns are arising at the azimuthal

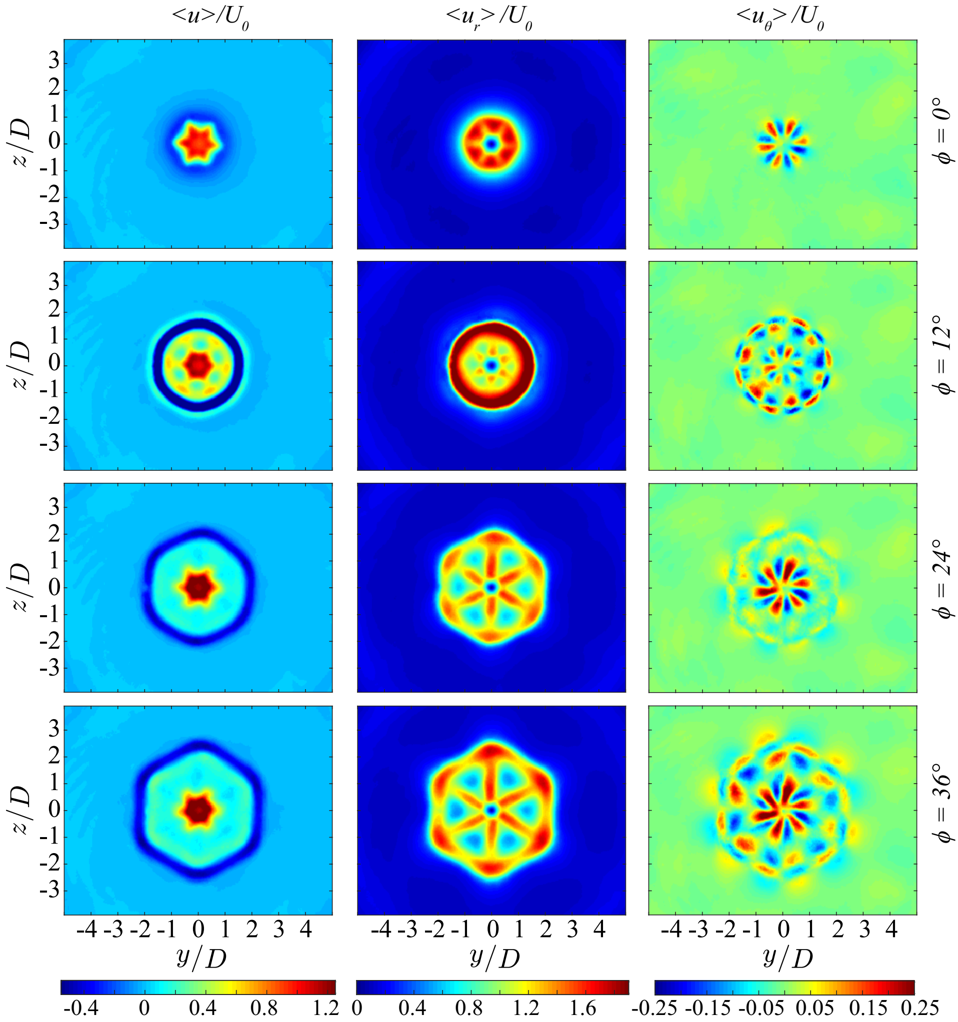

Figure 6.5: Phase-averaged (first column) axial, (second column) radial and (third column) azimuthal velocity components for the chevron synthetic jet.

position of the apices. As already stated before, the peaks of outflow at the apices could be associated with the streamwise vortices and the star-shaped jet which create a flow from the notches towards the apices, as shown in the third column, resulting in preferential outflow paths along the apices. At $\phi = 12°$, the effect of the presence of the plate on the impinging trailing jet creates a minimum of axial velocity at the jet axis, $r/D = 0$, surrounded by higher axial velocity values. The non-circular primary vortex ring has already impinged on the wall and it is located at approximatively $r/D \approx 1.3$ assuming a quasi-circular shape. It will be shown in the next section that the non-circular primary vortex ring changes its three-dimensional structure. As for the circular jet, looking at the axial and radial velocity components, a counter-rotating secondary vortex ring is formed on the wall. The second column of Figure 6.5 shows that at $\phi = 12°$, the flow field is characterised by an annular region of local maximum of radial velocity and an outer thin annular region of low radial velocity associated to the secondary vortex ring.

The investigated phases, not reported here, show the secondary vortex ring is already formed at $\phi = 12°$ located at about $r/D \approx 1.7$. Then at $\phi = 18°$ approaches $r/D \approx 2.0$ and it is no longer detected at $\phi = 24°$.

At the location of the primary and secondary vortex rings, azimuthal velocity components are present, as reported at $\phi = 12°$ on the third column of Figure 6.5. The three-dimensional structure of the non-circular primary vortex ring is the main cause of this effect. Indeed, the axial and radial vorticity components of the non-circular vortex ring induce the azimuthal velocity pattern. At the subsequent phases $\phi = 24°$ and $36°$, as for the circular case, the central region of impingement is characterised by higher axial velocity. This suggests that, also in this case, the maximum of axial velocity is located downstream of the vortex ring in the trailing jet. As a consequence, the azimuthal velocity (third column of Figure 6.5) around the stagnation region exhibits an increase of the flow velocity convected along the preferential outflow paths (second column of Figure 6.5). The non-circular vortex ring assumes a hexagonal shape with the vertices at the apex directions. This structure is caused by the high radial velocity along such directions. In particular, at $\phi = 24°$ the velocity field induced by the non-circular vortex ring is weak because of the lift-up of the vortex as shown in the 3D reconstruction of Figure 6.8c, whilst, it could probably approach again the plate at $\phi = 36°$.

At $\phi = 0°$, a low turbulence intensity level ahead of the non-circular vortex ring is measured. The phase $\phi = 12°$ in Figure 6.6 shows that the

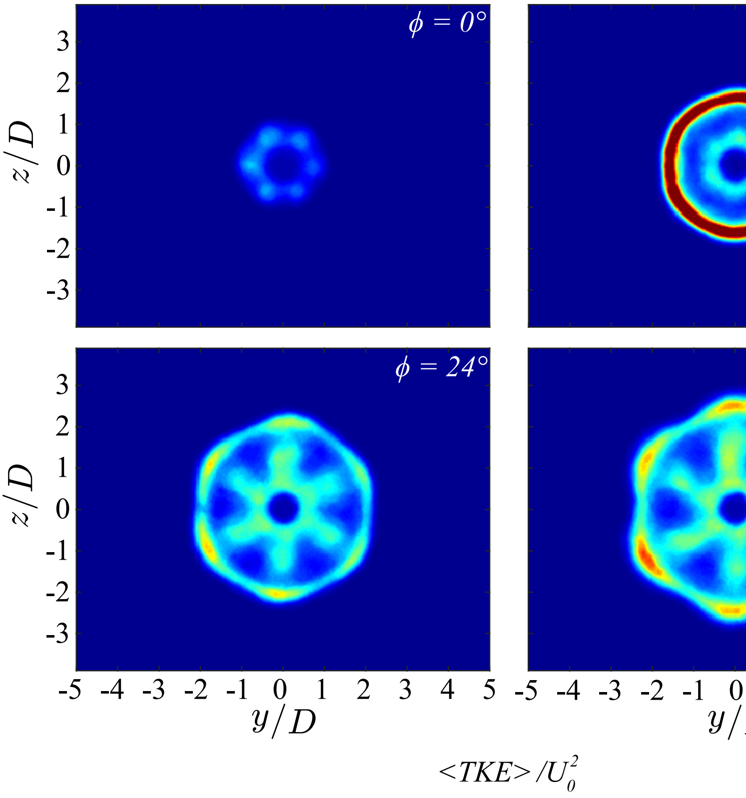

Figure 6.6: Phase-averaged turbulent kinetic energy for the chevron synthetic jet.

chevron synthetic jet exhibits an inner annular region at about $r/D \approx 0.5$ and another annular region at about $r/D \approx 1.6$ of significant $< TKE >$ values. The former region is ascribed to the shear layer of the impinging trailing jet. The latter, as for the circular case, is generated by the interaction between the primary and secondary vortex rings. At phases 24° and 36°, the flow field is also characterised by a star pattern of $< TKE >$. During the phase evolution, the star pattern spreads radially along the direction of the apices. This suggests that the $< TKE >$ in such a region is caused by the impinging trailing jet shear layer and the radial flow on the wall at the direction of the apices. The annular region of $< TKE >$ , stretched passing from 24° to 36°, is caused by the sweeping non-circular vortex ring. The peaks of turbulent kinetic energy at the vertices of the non-circular vortex ring could probably be related to the three-dimensional structure of the non-circular vortex ring itselft which is closer to the plate in such regions.

It should be pointed out that the effect of the non-circular primary and secondary vortices, ranging between $r/D \approx 1.7$ and 2, causes an inflection point in the Nusselt number profile located approximately at $r/D \approx 1.8$ (as previously shown in Figure 5.5).

### 6.2.3 Impinging flow field reconstruction

In order to study the three-dimensional flow organisation of the two investigated configurations of impinging jets, the flow field is reconstructed by means of scanning Stereo-PIV measurements for three phases corresponding to $\phi = 0°$, 18°, 36° for the circular case and 0°, 12° and 24° for the chevron one. The reconstructed phases correspond to three synthetic jet different conditions: approaching, impinging and developing on the plate. The $Q$ criterion (Jeong and Hussain, 1995) is used to visualise the azimuthal vortex structures, while the axial component of the vorticity $\omega_x$ is used to visualise the streamwise vortex structures.

Figure 6.7a shows that the circular synthetic jet is characterised by a circular vortex ring travelling towards the wall. At the phase 0°, the vortex ring core is located at $r/D \approx 1$ and the axial position is $x/D \approx 1.25$. Then, the vortex ring penetrates the wall boundary layer and initiates the formation of the counter-rotating secondary vortex ring near the wall. The secondary vortex ring has been reconstructed at $\phi = 18°$ and shown in Figure 6.7b. The primary vortex ring assumes an axial position of about $x/D = 1.75$ and it results stretched in radial position at $r/D \approx 1.8$, whilst the secondary vortex ring is close to the wall and the core is located at $r/D \approx 2.1$. As a consequence of the secondary vortex formation, the primary vortex ring lifts up from the wall (Fabris et al., 1996; Greco et al., 2017). Subsequently, at phase $\phi = 36°$ the secondary vortex ring is no longer visible and uniquely the primary vortices is observed at $x/D \approx 1.45$ and $r/D = 2.1$.

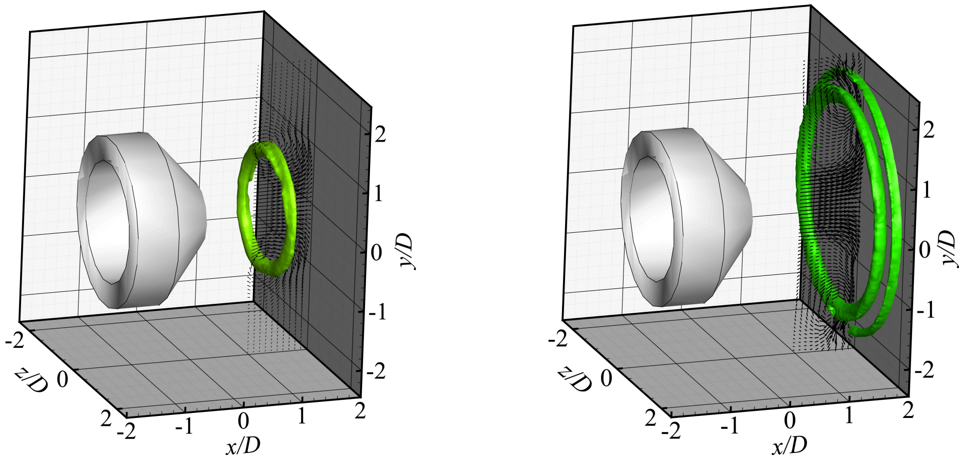

(a) $\phi = 0°$ (b) $\phi = 18°$

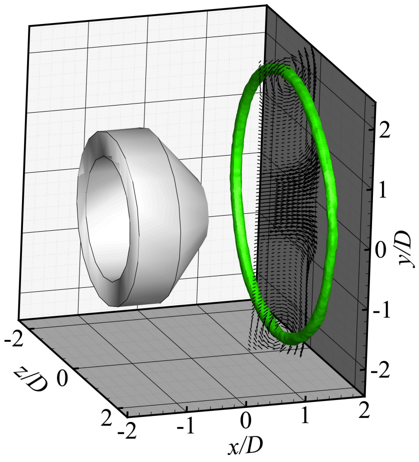

(c) $\phi = 36°$

Figure 6.7: Three-dimensional reconstruction of the flow field at phase (a) 0°, (b) 18° and (c) 36° for the circular synthetic jet. Green iso-surface with $QD^2/U_0^2 = 35$ for 0° and $QD^2/U_0^2 = 60$ for 18° and 36°.

For the chevron synthetic jet, the impinging flow field is characterised by a non-circular vortex ring and six pairs of counter-rotating streamwise vortices developed from the edges of the chevron nozzle, as shown in Figure 6.8a. At the phase 0°, the non-circular vortex ring core features axial and radial different positions at notch and apex directions. The non-circular vortex ring core corresponding to the notches of the nozzle is located at $x/D \approx 1.6$ and $r/D \approx 0.7$, while the portion of the vortex azimuthally corresponding to the apices of the nozzle is located at $x/D \approx 1.4$ and $r/D \approx 0.9$. The counter-rotating streamwise vortices developed from the left and right side of the notch valley show a divergence from the notches to get close to the counter-rotating streamwise vortex developed from the adjacent notch valley. The mutual induction of the streamwise vortices and the pressure gradient behind the chevron elements should be the main causes of this effect. At this phase, the vortical structures are approaching the impingement plate. As the vortex structures impinge on the wall, the non-circular vortex ring generates the formation of a counter-rotating secondary vortex ring near the wall. The corresponding flow field reconstruction is reported in Figure 6.8b. The vortex ring spreads on the wall assuming a hexagonal shape with the vertices along the direction of the apices radially located at approximately $r/D \approx 1.4$, and the axial difference is reduced assuming $x/D \approx 1.83$ and 1.76 at the notch and apex directions, respectively. The secondary vortex ring is stretched and presents the same pattern of the primary vortex ring. The vertices are located at approximately $r/D \approx 1.8$ and it is possible to note that also for the secondary vortex ring an axial different location of the vortex ring core along the directions corresponding to the apices and the notches is present. However, it is not possible to fully reconstruct the secondary vortex being in certain regions closer to the wall with respect to the measurement planes used for the reconstruction. From the flow field reconstruction, radial vortices on the wall are not visible, as also confirmed from the phase-averaged measurements. So, it is reasonable to assume that the streamwise vortices break up at the impingement and their effect is to produce an annular region of increased turbulence around the stagnation zone as shown in Figure 6.6. Afterwards, as for the circular synthetic jet, the primary vortex ring lifts up from the wall and the secondary vortex ring is not present. At phase $\phi = 24°$, the primary vortex ring is located at $x/D \approx 1.6$. The vortex ring presents a quasi-planar configuration characterised by an hexagonal pattern as shown in Figure 6.8c.

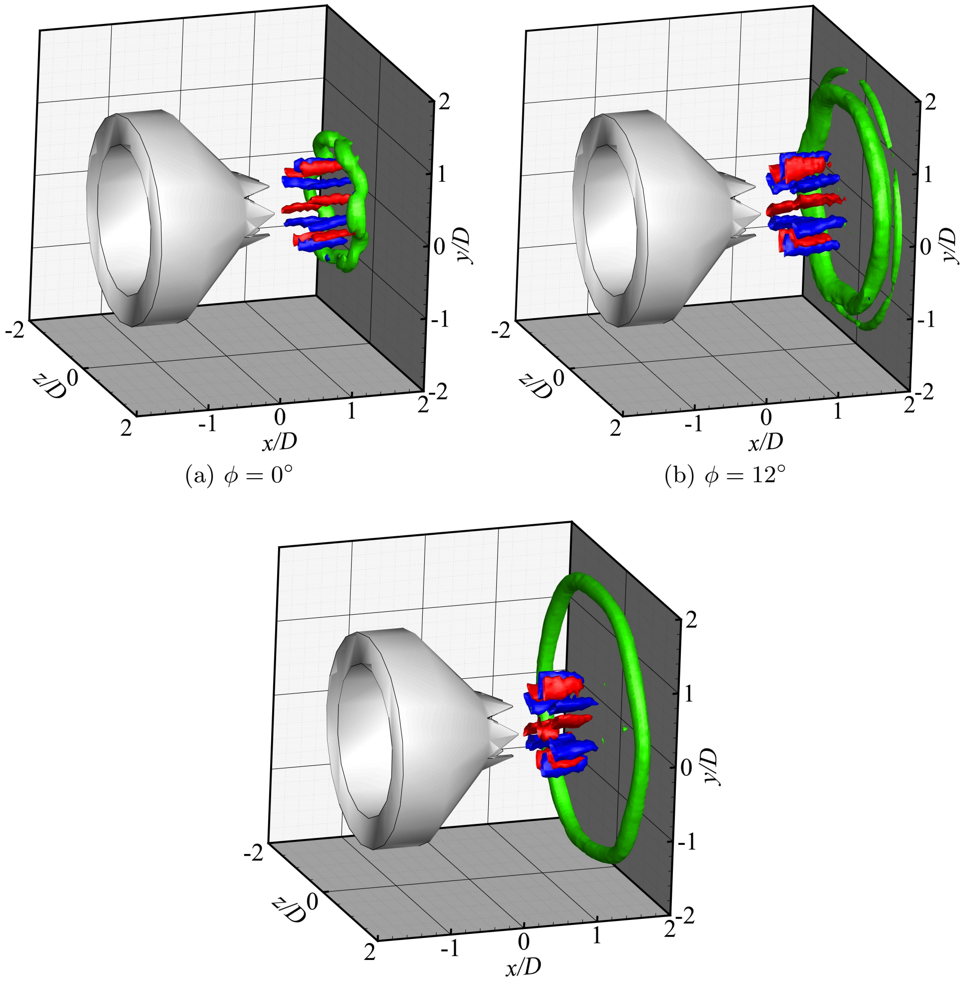

(a) $\phi = 0°$

(b) $\phi = 12°$

(c) $\phi = 24°$

Figure 6.8: Three-dimensional reconstruction of the flow field at phase (a) 0°, (b) 12° and (c) 24° for the chevron synthetic jet. Green iso-surface with $QD^2/U_0^2 = 60$, blue iso-surfaces with $\omega_x D/U_0$ equal to -4.5 for $\phi = 0°$ and -2 for $\phi = 12°$ and 24° and red iso-surfaces with $\omega_x D/U_0$ equal to 4.5 for $\phi = 0°$ and 2 for $\phi = 12°$ and 24°.

# Chapter 7

# Conclusions and outlooks

In this work, the flow field and heat transfer of a chevron synthetic jet are experimentally investigated and compared with those of a circular synthetic jet. Particle image velocimetry (both planar and stereoscopic) for the flow field analysis and IR Thermography for the evaluation of the convective heat transfer rate of impinging synthetic jets are applied.

The free synthetic jets (Chapter 4) are obtained by operating both configurations at the same input electric power, resulting in Reynolds and Strouhal numbers equal to 5600 and 0.115 for the circular synthetic jet and 6000 and 0.106 for the chevron one. Reynolds number and Strouhal number are close enough for comparison. In presence of the chevron exit, the circular vortex ring issued through the circular nozzle exit, is replaced by a non-circular vortex ring with additional streamwise vortices. The mutual interaction between these structures prevents the axis-switching of the non-circular vortex ring during its convection. The presence of the streamwise vortices causes a flow motion towards the jet axis in the apex plane and an opposite motion in the notch plane. The global effect is mixing and entrainment enhancement. These streamwise vortices dissipate while convecting downstream and the vortex ring assumes a circular shape. Comparing the two configurations, the chevron exit generates a larger time-averaged streamwise velocity along the centreline but with lower turbulent kinetic energy intensity. Differences are also present between the notch and the apex streamwise-radial planes of the chevron exit. In the notch plane, both the time-averaged axial velocity component profile in the spanwise direction and the shear layer width are wider than in the apex plane. Furthermore, considering the turbulent kinetic energy distribution, the chevron case shows larger levels near the exit and lower levels at more downstream locations.

Then, heat transfer performance is experimentally studied in Chapter 5 with the heated thin foil heat flux sensor along with temperature measurements from IR thermography for different nozzle-to-plate distances. The circular synthetic jet, taken as a reference case, is operated at Reynolds number equal to 4500 and three values of the dimensionless stroke length (i.e. the inverse of Strouhal number) equal to 9, 56, 112. The chevron synthetic jet is synthesised by keeping the same pressure oscillation in the device cavity. For $L_0/D$ approaching higher investigated values, both impinging synthetic jets show a heat transfer behaviour similar to that of continuous ones. Indeed, high stroke length implies long extension of the trailing jet and a flow field characterised by a long fluid column. The chevron synthetic jet shows a star-shaped heat transfer pattern similar to that observed for an impinging continuous jets. As the dimensionless stroke length is reduced, the heat transfer rate increases. The unsteady behaviour of the train of vortices mainly affects the heat transfer. In particular, the vortices are responsible for a higher entrainment and a wider jet width. Furthermore, as the dimensionless stroke length reduces from 112 to 9, the maximum stagnation Nusselt number passes from being located at a dimensionless nozzle-to-plate distance of 6 to about 4-6 for the circular synthetic jet and from about 4-6 to 2-4 for the chevron synthetic jet. Two considerations can be inferred from this observation. The first idea is that, probably, this feature could be addressed to a longer or shorter extension of the potential core of the jet based on the stroke length, respectively. Secondly, in the chevron synthetic jet, the potential core-like region is shorter than that of the circular exit because of a more penetrating shear layer. This could explain the global shift of about $1D$ of the maximum stagnation Nusselt number position in term of nozzle-to-plate distance. The chevron synthetic jet has shown better heat transfer characteristics for short nozzle-to-plate distances and short dimensionless stroke lengths. As well assessed in literature, for free chevron continuous jets Doty et al. (2007); Zaman et al. (2011) and experimentally seen in Chapter 4 for a free chevron synthetic jet, the chevron geometry has the effect of modifying the turbulence distribution with respect to a circular exit, by increasing the turbulence level near the nozzle exit. Hence, this increase at low stroke lengths and nozzle-to-plate distances can be related to enhanced turbulent-induced mixing and entrainment near the exit, caused by the non-circular vortex ring and streamwise vortices that develop from the chevron notches.

At the end, the flow field in impinging configuration is analysed at the nozzle-to-plate distance of 2 diameters (Chapter 6). Based on the heat transfer results, the condition at Reynolds number $Re = 4500$ and dimensionless stroke length $L_0/D = 28$ is chosen. Two different experiments are carried out. The first experiment is devoted to the characterisation of the flow field evolution on the impingement plate. The second experiment is a complete 3D reconstruction of the entire flow field at the phases chosen by analysing the results obtained through the first experiment. Three phases are reconstructed corresponding to three synthetic jet conditions: approaching vortex, impinging vortex and flow developing on the plate. These measurements allows to better understand the heat transfer characteristics. The heat transfer enhancement of the chevron synthetic jet is addressed to two main agents (as shown by the results reported in Chapter 6): first, the cross-shaped exit leads to the acceleration of the fluid, thus to a larger impinging velocity; second, the presence of streamwise structures, as presented also in the free synthetic jet case, are responsible for a significant enhancement of the jet entrainment and mixing in correspondence of the impinged plate at low nozzle-to-plate distance. Furthermore, the convective heat transfer rate presents regions of minimum values of Nusselt number in correspondence of the directions of the notches. The impinging flow field results show that they are ascribed to the presence of counter-rotating vortices that produce a local flow with preferential radial paths.

This study represents the first experimental investigation of a synthetic jet device equipped with a chevron exit. The results obtained have led to a better knowledge of the flow behaviour and heat transfer characteristics of a chevron synthetic jet, but many questions are still open.

A parametric study on the geometry of the chevron exit (number of chevron elements, length and penetration depth) and governing parameters (Reynolds number and Strouhal number) would be of interest to identify a possible impact on the shear layer and flow topology of the propagating synthetic jet and on the extension of the region of intense turbulent kinetic energy near the exit.

The heat transfer distribution shows a strong dependence on the Strouhal number. A more extensive study at different Strouhal numbers and chevron exit parameters might lead to the development of an empirical correlation on the stagnation point heat transfer rate as a function of the geometric parameters.

Finally, the acoustic noise emission is a relevant problem associated with the employment of small scale synthetic jet actuators. Chevron exits applied to synthetic jet devices might be a strategy for noise reduction.

# References

G. N. Abramovich, T. A. Girshovich, S. I. Krasheninnikov, A. N. Sekundov, and I. P. Smirnova. The theory of turbulent jets. *Moscow Izdatel Nauka*, 1984.

R. J. Adrian and C.-S. Yao. Pulsed laser technique application to liquid and gaseous flows and the scattering power of seed materials. *Applied Optics*, 24(1):44–52, 1985.

M. Al-Atabi. Experimental investigation of the use of synthetic jets for mixing in vessels. *Journal of Fluids Engineering*, 133(9):094503, 2011.

M. Amitay, D. R. Smith, V. Kibens, D. E. Parekh, and A. Glezer. Aerodynamic flow control over an unconventional airfoil using synthetic jet actuators. *AIAA Journal*, 39(3):361–370, 2001.

M. Arik and T. Icoz. Predicting heat transfer from unsteady synthetic jets. *Journal of Heat Transfer*, 134(8):081901, 2012.

T. Astarita. Analysis of interpolation schemes for image deformation methods in piv: effect of noise on the accuracy and spatial resolution. *Experiments in Fluids*, 40(6):977–987, 2006.

T. Astarita. Analysis of weighting windows for image deformation methods in piv. *Experiments in Fluids*, 43(6):859–872, 2007.

T. Astarita. Analysis of velocity interpolation schemes for image deformation methods in piv. *Experiments in Fluids*, 45(2):257–266, 2008.

T. Astarita and G. Cardone. Analysis of interpolation schemes for image deformation methods in piv. *Experiments in Fluids*, 38(2):233–243, 2005.

T. Astarita and G. M. Carlomagno. *Infrared thermography for thermo-fluid-dynamics*. Springer Science & Business Media, 2012.

F. Bazdidi-Tehrani, M. Karami, and M. Jahromi. Unsteady flow and heat transfer analysis of an impinging synthetic jet. *Heat and Mass Transfer*, 47(11):1363–1373, 2011.

U. S. Bhapkar, A. Srivastava, and A. Agrawal. Acoustic and heat transfer characteristics of an impinging elliptical synthetic jet generated by acoustic actuator. *International Journal of Heat and Mass Transfer*, 79:12–23, 2014.

Boeing. Boeing 737 max. `http://www.boeing.com/commercial/737max/#/gallery`. Accessed: 13-10-2017.

L. J. S. Bradbury and A. H. Khadem. The distortion of a jet by tabs. *Journal of Fluid Mechanics*, 70(4):801–813, 1975.

J. Bridges and C. Brown. Parametric testing of chevrons on single flow hot jets. In *10th AIAA/CEAS Aeroacoustics Conference*, page 2824, 2004. doi: 10.2514/6.2004-2824.

J. Bridges and M. P. Wernet. Turbulence measurements of separate flow nozzles with mixing enhancement features. 2002.

G. M. Carlomagno and G. Cardone. Infrared thermography for convective heat transfer measurements. *Experiments in Fluids*, 49(6):1187–1218, 2010.

G. M. Carlomagno and A. Ianiro. Thermo-fluid-dynamics of submerged jets impinging at short nozzle-to-plate distance: a review. *Experimental Thermal and Fluid Science*, 58:15–35, 2014.

J. E. Cater and J. Soria. The evolution of round zero-net-mass-flux jets. *Journal of Fluid Mechanics*, 472:167–200, 2002.

M. Chaudhari, B. Puranik, and A. Agrawal. Heat transfer characteristics of synthetic jet impingement cooling. *International Journal of Heat and Mass Transfer*, 53(5):1057–1069, 2010a.

M. Chaudhari, B. Puranik, and A. Agrawal. Effect of orifice shape in synthetic jet based impingement cooling. *Experimental Thermal and Fluid Science*, 34(2):246–256, 2010b.

M. Chaudhari, B. Puranik, and A. Agrawal. Multiple orifice synthetic jet for improvement in impingement heat transfer. *International Journal of Heat and Mass Transfer*, 54(9):2056–2065, 2011.

D. J. Coe, M. G. Allen, M. A. Trautman, and A. Glezer. Micromachined jets for manipulation of macro flows. In *Solid-State Sensor and Actuator Workshop*, pages 13–16, 1994.

D. J. Coe, M. G. Allen, B. L. Smith, and A. Glezer. Addressable micromachined jet arrays. In *Solid-State Sensors and Actuators, 1995 and Eurosensors IX.. Transducers' 95. The 8th International Conference on*, volume 2, pages 329–332. IEEE, 1995.

C. M. Crispo, C. S. Greco, F. Avallone, and G. Cardone. On the flow organization of a chevron synthetic jet. *Experimental Thermal and Fluid Science*, 82:136–146, 2017.

M. J. Doty, B. S. Henderson, and K. W. Kinzie. Turbulence measurements of separate-flow nozzles with pylon interaction using particle image velocimetry. *AIAA Journal*, 45(6):1281, 2007.

C. Eckart. Vortices and streams caused by sound waves. *Physical Review*, 73:68–76, Jan 1948. doi: 10.1103/PhysRev.73.68. URL `https://link.aps.org/doi/10.1103/PhysRev.73.68`.

D. Fabris, D. Liepmann, and D. Marcus. Quantitative experimental and numerical investigation of a vortex ring impinging on a wall. *Physics of Fluids*, 8(10):2640–2649, 1996.

M. Gad-el Hak. *Flow control: passive, active, and reactive flow management.* Cambridge University Press, 2006.

R. Gardon. Heat transfer between a flat plate and jets of air impinging on it. *International Development on Heat Transfer (ASME)*, pages 454–460, 1962.

M. Gharib, E. Rambod, and K. Shariff. A universal time scale for vortex ring formation. *Journal of Fluid Mechanics*, 360:121–140, 1998.

R. Giordano and T. Astarita. Spatial resolution of the stereo piv technique. *Experiments in Fluids*, 46(4):643, 2009.

A. Glezer and M. Amitay. Synthetic jets. *Annual Review of Fluid Mechanics*, 34(1):503–529, 2002.

C. S. Greco, A. Ianiro, T. Astarita, and G. Cardone. On the near field of single and twin circular synthetic air jets. *International Journal of Heat and Fluid Flow*, 44:41–52, 2013.

C. S. Greco, A. Ianiro, and G. Cardone. Time and phase average heat transfer in single and twin circular synthetic impinging air jets. *International Journal of Heat and Mass Transfer*, 73:776–788, 2014.

C. S. Greco, G. Castrillo, C. M. Crispo, T. Astarita, and G. Cardone. Investigation of impinging single and twin circular synthetic jets flow field. *Experimental Thermal and Fluid Science*, 74:354–367, 2016.

C. S. Greco, G. Cardone, and J. Soria. On the behaviour of impinging zero-net-mass-flux jets. *Journal of Fluid Mechanics*, 810:25–59, 2017.

C. S. Greco, G. Paolillo, A. Ianiro, G. Cardone, and L. de Luca. Effects of the stroke length and nozzle-to-plate distance on synthetic jet impingement heat transfer. *International Journal of Heat and Mass Transfer*, 117:1019–1031, 2018.

F. F. Grinstein, E. J. Gutmark, T. P. Parr, D. M. Hanson-Parr, and U. Obeysekare. Streamwise and spanwise vortex interaction in an axisymmetric jet. a computational and experimental study. *Physics of Fluids*, 8(6): 1515–1524, 1996.

E. Gutmark, Y. Yassour, and M. Wolfshtein. Acoustic enhancement of heat transfer in plane channels. *Heat transfer 1982*, pages 441–445, 1982.

E. J. Gutmark and F. F. Grinstein. Flow control with noncircular jets. *Annual Review of Fluid Mechanics*, 31(1):239–272, 1999.

M. Hadžiabdić and K. Hanjalić. Vortical structures and heat transfer in a round impinging jet. *Journal of Fluid Mechanics*, 596:221–260, 2008.

R. Holman, Y. Utturkar, R. Mittal, B. L. Smith, and L. Cattafesta. Formation criterion for synthetic jets. *AIAA Journal*, 43(10):2110–2116, 2005.

A. K. M. F. Hussain and W. C. Reynolds. The mechanics of an organized wave in turbulent shear flow. *Journal of Fluid Mechanics*, 41(2):241–258, 1970.

U. Ingård and S. Labate. Acoustic circulation effects and the nonlinear impedance of orifices. *The Journal of the Acoustical Society of America*, 22(2):211–218, 1950. doi: http://dx.doi.org/10.1121/1.1906591.

K. Jambunathan, E. Lai, M. A. Moss, and B. L. Button. A review of heat transfer data for single circular jet impingement. *International Journal of Heat and Fluid Flow*, 13(2):106–115, 1992.

J. Jeong and F. Hussain. On the identification of a vortex. *Journal of Fluid Mechanics*, 285:69–94, 1995.

C. J. M. Lasance and R. M. Aarts. Synthetic jet cooling part i: overview of heat transfer and acoustics. In *Semiconductor Thermal Measurement and Management Symposium, 2008. Semi-Therm 2008. Twenty-fourth Annual IEEE*, pages 20–25. IEEE, 2008.

I. V. Lebedeva. Experimental study of acoustic streaming in the vicinity of orifices. *Soviet Physics Acoustics*, 26:331–333, 1980.

P. Levesque, P. Brémond, J.-L. Lasserre, A. Paupert, and D. L. Balageas. Performance of fpa ir cameras and their improvement by time, space and frequency data processing: Part i-intrinsic characterization of the thermographic system. *Quantitative InfraRed Thermography Journal*, 2(1): 97–112, 2005.

J. Lighthill. Acoustic streaming. *Journal of Sound and Vibration*, 61(3): 391–418, 1978.

M. J. Lighthill. On sound generated aerodynamically. i. general theory. In *Proceedings of the Royal Society of London A: Mathematical, Physical and Engineering Sciences*, volume 211, pages 564–587. The Royal Society, 1952.

Z.-B. Luo, Z.-X. Xia, and B. Liu. New generation of synthetic jet actuators. *AIAA Journal*, 44(10):2418–2420, 2006.

Z.-B. Luo, D. Xiong, W. Lin, and Z.-X. Xia. Experimental technique based on delay phase angle and piv measurements of a dual synthetic jets actuator. In *Piezoelectricity, Acoustic Waves and Device Applications (SPAWDA), 2011 Symposium on*, pages 269–273. IEEE, 2011.

R. Mahalingam and A. Glezer. Design and thermal characteristics of a synthetic jet ejector heat sink. *Journal of Electronic Packaging*, 127(2): 172–177, 2005.

S. Mallinson, G. Hong, and J. Reizes. Some characteristics of synthetic jets. In *30th Fluid Dynamics Conference*, page 3651, 1999.

L. D. Mangate and M. B. Chaudhari. Heat transfer and acoustic study of impinging synthetic jet using diamond and oval shape orifice. *International Journal of Thermal Sciences*, 89:100–109, 2015.

H. Martin. Heat and mass transfer between impinging gas jets and solid surfaces. *Advances in Heat Transfer*, 13:1–60, 1977.

T. Maxworthy. Some experimental studies of vortex rings. *Journal of Fluid Mechanics*, 81(3):465–495, 1977.

W. H. McAdams. Heat transmission. Technical report, 1954.

A. McGuinn, R. Farrelly, T. Persoons, and D. B. Murray. Flow regime characterisation of an impinging axisymmetric synthetic jet. *Experimental Thermal and Fluid Science*, 47:241–251, 2013.

E. P. Mednikov and B. G. Novitskii. Experimental study of intense acoustic streaming. *Akusticheskii Zhurnal*, 21:245–249, 1975.

A. Melling. Tracer particles and seeding for particle image velocimetry. *Measurement Science and Technology*, 8(12):1406, 1997.

R. J. Moffat. Describing the uncertainties in experimental results. *Experimental Thermal and Fluid Science*, 1(1):3–17, 1988.

K. Mohseni and R. Mittal. *Synthetic Jets: Fundamentals and Applications*. CRC Press, 2014.

M. Mueller, L. Bernal, R. Moran, P. Washabaugh, B. Parviz, T.-K. Chou, C. Zhang, and K. Najafi. Thrust performance of micromachined synthetic jets. In *Fluids 2000 Conference and Exhibit*, page 2404, 2000.

R. T. Nagel, J. W. Denham, and A. G. Papathanasiou. Supersonic jet screech tone cancellation. *AIAA Journal*, 21:1541–1545, 1983.

NASA. Boeing 777. `https://www.nasa.gov/topics/aeronautics/features/bridges_chevron_events.html`. Accessed: 13-10-2017.

K. Otani, J. Moore, W. Gressick, and M. Amitay. Active yaw control of a ducted fan-based mav using synthetic jets. *International Journal of Flow Control*, 1(1):29–42, 2009.

S. S. Pannu and N. H. Johannesen. The structure of jets from notched nozzles. *Journal of Fluid Mechanics*, 74(3):515–528, 1976.

G. Paolillo, C. S. Greco, and G. Cardone. Novel quadruple synthetic jet device: Flowfield and acoustic behavior. *AIAA Journal*, 2017.

A. Pavlova and M. Amitay. Electronic cooling using synthetic jet impingement. *Journal of Heat Transfer*, 128(9):897–907, 2006.

T. Persoons, T. S. O'Donovan, and D. B. Murray. Heat transfer in adjacent interacting impinging synthetic jets. In *ASME 2009 Heat Transfer Summer Conference collocated with the InterPACK09 and 3rd Energy Sustainability Conferences*, pages 955–962. American Society of Mechanical Engineers, 2009.

T. Persoons, A. McGuinn, and D. B. Murray. A general correlation for the stagnation point nusselt number of an axisymmetric impinging synthetic jet. *International Journal of Heat and Mass Transfer*, 54(17):3900–3908, 2011.

S. Polat, B. Huang, A. S. Mujumdar, and W. J. M. Douglas. Numerical flow and heat transfer under impinging jets: a review. *Annual Review of Heat Transfer*, 2(2), 1989.

A. Powell. Theory of vortex sound. *The journal of the acoustical society of America*, 36(1):177–195, 1964.

A. K. Prasad. Stereoscopic particle image velocimetry. *Experiments in Fluids*, 29(2):103–116, 2000.

M. Raffel, C. E. Willert, J. Kompenhans, et al. *Particle image velocimetry: a practical guide.* Springer Science & Business Media, 2007.

M. J. Rau, E. M. Dede, and S. V. Garimella. Local single-and two-phase heat transfer from an impinging cross-shaped jet. *International Journal of Heat and Mass Transfer*, 79:432–436, 2014.

Lord Rayleigh. *The theory of sound.* Macmillan and co., 1896.

M. F. Reeder and M. Samimy. The evolution of a jet with vortex-generating tabs: real-time visualization and quantitative measurements. *Journal of Fluid Mechanics*, 311:73–118, 1996.

W. Rohlfs, H. D. Haustein, O. Garbrecht, and R. Kneer. Insights into the local heat transfer of a submerged impinging jet: Influence of local flow acceleration and vortex-wall interaction. *International Journal of Heat and Mass Transfer*, 55(25):7728–7736, 2012.

C. L. Rumsey, T. B. Gatski, W. L. Sellers III, V. N. Vasta, and S. A. Viken. Summary of the 2004 computational fluid dynamics validation workshop on synthetic jets. *AIAA Journal*, 44(2):194–207, 2006.

M. Samimy, K. B. M. Q. Zaman, and M. F. Reeder. Effect of tabs on the flow and noise field of an axisymmetric jet. *AIAA Journal*, 31(4):609–619, 1993.

C. F. Schram. Aeroacoustics of subsonic jets: Prediction of the sound produced by vortex pairing based on particle image velocimetry. 2003. doi: http://dx.doi.org/10.6100/IR561402. URL `http://repository.tue.nl/aae38a03-e973-49a9-bf8f-7763650e855c`.

J. M. Shuster and D. R. Smith. Experimental study of the formation and scaling of a round synthetic jet. *Physics of Fluids*, 19(4):045109, 2007.

L. A. Silva and A. Ortega. Convective heat transfer in an impinging synthetic jet: A numerical investigation of a canonical geometry. *Journal of Heat Transfer*, 135(8):082201, 2013.

B. L. Smith and A. Glezer. The formation and evolution of synthetic jets. *Physics of Fluids*, 10(9):2281–2297, 1998.

B. L. Smith and A. Glezer. Jet vectoring using synthetic jets. *Journal of Fluid Mechanics*, 458:1–34, 2002.

B. L. Smith and G. W. Swift. A comparison between synthetic jets and continuous jets. *Experiments in Fluids*, 34(4):467–472, 2003.

J. Taylor. *Introduction to error analysis, the study of uncertainties in physical measurements.* 1997.

P. Valiorgue, T. Persoons, A. McGuinn, and D. B. Murray. Heat transfer mechanisms in an impinging synthetic jet for a small jet-to-surface spacing. *Experimental Thermal and Fluid Science*, 33(4):597–603, 2009.

D. Violato and F. Scarano. Three-dimensional evolution of flow structures in transitional circular and chevron jets. *Physics of Fluids*, 23(12):124104, 2011.

D. Violato, A. Ianiro, G. Cardone, and F. Scarano. Three-dimensional vortex dynamics and convective heat transfer in circular and chevron impinging jets. *International Journal of Heat and Fluid Flow*, 37:22–36, 2012.

R. Viskanta. Heat transfer to impinging isothermal gas and flame jets. *Experimental Thermal and Fluid Science*, 6(2):111–134, 1993.

I. A. Waitz, Y. J. Qiu, T. A. Manning, A. K. S. Fung, J. K. Elliot, J. M. Kerwin, J. K. Krasnodebski, M. N. O'Sullivan, D. E. Tew, E. M. Greitzer, et al. Enhanced mixing with streamwise vorticity. *Progress in Aerospace Sciences*, 33(5-6):323–351, 1997.

H. Wang and S. Menon. Fuel-air mixing enhancement by synthetic microjets. *AIAA Journal*, 39(12):2308–2319, 2001.

J. R. Welty, C. E. Wicks, G. Rorrer, and R. E. Wilson. *Fundamentals of momentum, heat, and mass transfer.* John Wiley & Sons, 2009.

J. Westerweel and F. Scarano. Universal outlier detection for piv data. *Experiments in Fluids*, 39(6):1096–1100, 2005.

R. Westley and G. M. Lilley. An investigation of the noise field from a small jet and methods for its reduction. Technical report, College of Aeronautics Cranfield, 1952.

B Wieneke. Stereo-piv using self-calibration on particle images. *Experiments in fluids*, 39(2):267–280, 2005.

C. Willert. Stereoscopic digital particle image velocimetry for application in wind tunnel flows. *Measurement Science and Technology*, 8(12):1465, 1997.

K. B. M. Q. Zaman. Axis switching and spreading of an asymmetric jet: the role of coherent structure dynamics. *Journal of Fluid Mechanics*, 316: 1–27, 1996.

K. B. M. Q. Zaman, M. F. Reeder, and M. Samimy. Control of an axisymmetric jet using vortex generators. *Physics of Fluids*, 6(2):778–793, 1994.

K. B. M. Q. Zaman, J. E. Bridges, and D. L. Huff. Evolution from 'tabs' to 'chevron technology' - a review. *International Journal of Aeroacoustics*, 10(5-6):685–709, 2011.

# List of publications

## Journal papers

- C. M. Crispo, C. S. Greco, F. Avallone and G. Cardone. On the flow organization of a chevron synthetic jet. *Experimental Thermal and Fluid Science*, 82:136–146, 2017.

- C. S. Greco, G. Castrillo, C. M. Crispo, T. Astarita and G. Cardone. Investigation of impinging single and twin circular synthetic jets flow field. *Experimental Thermal and Fluid Science*, 74:354-367, 2016.

- C. M. Crispo, C. S. Greco and G. Cardone. Heat transfer characteristics of chevron and circular synthetic jets. To be submitted.

- C. M. Crispo, C. S. Greco and G. Cardone. Investigation of chevron and circular impinging synthetic jets flow field. To be submitted.

- C. M. Crispo, F. Avallone, F. F. J. Schrijer and G. Cardone. Effect of an isolated roughness element on hypersonic boundary layer transition investigated by tomographic PIV. To be submitted.

## Conference papers

- C. M. Crispo, C. S. Greco, F. Avallone and G. Cardone. Stereo PIV measurements on circular and chevron synthetic jets. In *11th International Symposium on Particle Image Velocimetry - PIV15, Santa Barbara, CA, USA*, September 14-16, 2015.

- G. Castrillo, C. S. Greco, C. M. Crispo, T. Astarita and G. Cardone. Impinging Single and Twin Circular Synthetic Jets Flow Field. In *11th International Symposium on Particle Image Velocimetry - PIV15, Santa Barbara, CA, USA*, September 14-16, 2015.

# Acknowledgements

I want to take this opportunity to express my gratitude for the numerous exceptional people who have helped me, guided me, or simply spent time with me throughout my PhD.

I feel enormously grateful to my supervisor Prof. *Gennaro Cardone.* Prof., you guided me during these years with valuable competence. Thanks for everything you have taught me. I am grateful to Prof. *Carlo Salvatore Greco*, my second supervisor. You gave me all the support to undertake this adventure, you have been the source of constant encouragement and help with enormous patience and dedication. I want also to thank Prof. *Tommaso Astarita.* You offered me the possibility of undertaking this path and you were always available for my countless questions and doubts. I also thank "*i Professori stranieri*" *Andrea Ianiro, Stefano Discetti* and *Gioacchino Cafiero* and "*lo statale*" *Peppe Ceglia.* You may not know, but you helped me directly or indirectly. I also wish to thank Prof. *Giovanni Maria Carlomagno*, I will never forget the advice and the nice conversations with him. I would also like to thank my PhD-student colleagues for the good company during the long days at the office and at the laboratory. In particular, thank you *Giusy Castrillo* (my darling deskmate), *Mattia Contino, Simone Boccardi* and *Gerardo Paolillo.* I wish to thank *Giuseppe Sicardi* for his help with equipments and bureaucratic hurdles.

I kindly acknowledge Delft University of Technology for providing the contoured nozzle and the chevron exit. I am thankful to Profs. *Fulvio Scarano, Ferry Schrijer* and *Francesco Avallone* (Fra', I put you in the Netherlands section, because it is well known that you are "*l'Olandese*" now), who hosted me for 6 months in Delft, for the support, the very long meetings and discussions we had. In the Netherlands, I was lucky to meet some special people. I have enjoyed staying together, partying, eating and laughing with Prof. *Daniele Ragni, Serena de Simone, Jan Schneiders, Greta Quaranta, Sara Barros, Beppe Caridi* and *Jacopo Serpieri.*

I am thankful to my family, that always provided me the necessary support. You have always respected my decisions.

Last but not least, my beloved *Jlenia*, you deserve my warmest thanks. You supported me all this time, always being on my side even when I did not deserve it. I am lucky to have you in my life.

*Cuono Massimo Crispo*